Doctoral Dissertation

All-Optical OOK to 16QAM Modulation Format Conversion Based on Fiber Nonlinearity

GUOXIU HUANG

August 2013

Division of Electrical, Electronic and Information Engineering
Graduate School of Engineering

OSAKA UNIVERSITY

This thesis is dedicated to my parents, Qingmin Huang and Xiuxian Yang, for their endless love, supports and encouragements.

Guoxiu

Preface

Due to the rapidly growing data and internet traffic, worldwide next-generation optical networks will require significant improvements in transmission capacity. Multi-level modulation format, preferably in combination with coherent detection is a key technique for simultaneously increasing the spectral efficiency (SE) and maintaining long transmission distance. Substituting multi-level modulation formats for conventional on-off keying (OOK) modulation, the bit rate of one wavelength channel of commercial wavelength division multiplexing (WDM) transmission networks can be upgraded from 10 Gb/s to 40 Gb/s or 100 Gb/s. The conventional on-off keying (OOK) modulation format will never be completely replaced by multi-level modulation formats in optic-fiber networks, because of its absolute advantages of cost-effective TX/RX structure, and high robustness against nonlinear impairments. In next-generation networks, disparate modulation formats should be incorporated together to achieve cost efficiency. The function of OOK to multi-level modulation format conversion will be an important interface technology to realize the optical network's demand of flexibility by choosing an optimal modulation format. All-optical signal processing techniques have received much attention due to their ultra-fast response and extended transparency. This is accomplished by eliminating optical-electrical-optical conversions in the optical fiber communication networks. Semiconductor optical amplifier (SOA) and highly nonlinear fiber (HNLF) have been widely employed for all-optical modulation format conversion. This thesis focuses on fiber nonlinearity and nonlinear effects. An attempt is made to propose and demonstrate an all-optical OOK to 16 quadrature amplitude modulation (QAM) format converter based on fiber nonlinearity.

In order to provide a good understanding on the principle of the proposed all-optical OOK to 16QAM format converter, the necessary knowledge of the nonlinear Schrödinger (NLS) equation, and nonlinear effects such as cross phase modulation (XPM) and four-waving mixing (FWM), are described in Chapter 2. Nonlinear optical loop mirror (NLOM), which is the main operation part of the converter, is attractive for its application in all-optical signal processing based fiber-optic communications. The researches related to NOLM will also be briefly summarized.

The efficiency of nonlinear effects depends on the fiber nonlinear coefficient γ. Accurate measurement of γ is one of the key criteria for designing transmission systems and HNLF-based

devices. In Chapter 3, a novel method to measure the nonlinear coefficient γ employing the phase-mismatching four-wave-mixing (PM-FWM) is proposed. The PM-FWM method can simultaneously measure the chromatic dispersion with high precision, and therefore its influence on the measurement of γ can be removed. The measurements of γ for highly nonlinear dispersion-shifted fibers (HNLDSFs) and a standard single mode fiber (SSMF) are made by the PM-FWM method. By comparing the PM-FWM measured results with ones measured by conventional methods, the practicability of the PM-FWM method was established.

The main research work of this thesis, a novel all-optical OOK to 16QAM modulation format conversion employing NOLM based on XPM and optical parametric amplification (OPA) in optical fibers is proposed and numerically demonstrated in Chapter 4. Simulation results confirm the feasibility of this converter.

In order to experimentally demonstrate the all-optical OOK to 16QAM format conversion, a simplified configuration of the converter with a 1:2 coupler employed in the NOLM is proposed in Chapter 5. The first experimental demonstration of an all-optical modulation format conversion from non-return-to-zero (NRZ)-OOK to return-to-zero (RZ)-16QAM is presented at 10 GS/s. The simulation and experimental results confirm the feasibility of this proposed converter.

Chapter 6 concludes the whole thesis. The whole study has been funded by Japanese Government of the Ministry of Education, Culture, Sports, Science and Technology (MEXT).

Guoxiu Huang
Osaka, Japan
August, 2013

Acknowledgements

The present research has been carried out during my tenure of doctoral course at the Department of Electrical, Electronic and Information Engineering, Graduate School of Engineering, Osaka University, under the guidance of Prof. Ken-ichi Kitayama.

First of all, I would like to gratefully and sincerely thank my supervisor, Prof. Ken-ichi Kitayama, for his guidance, understanding, and patience during my graduate studies at Osaka University. Without his support and encouragement, I would never have finished this work. I could not have imagined having a better advisor for my Ph.D. Acknowledgements also go to Prof. Kyo Inoue of Department of Electrical, Electronic and Information Engineering, Osaka University, for his careful review and invaluable discussions on this thesis.

I am deeply grateful to Associate Prof. Akihiro Maruta of Department of Electrical, Electronic, and Information Engineering, Osaka University, for giving me sufficient basic backgrounds, and many advises for my research, spending his time carefully going through my publication drafts, correcting my presentations, and helping me tremendously at every step forward.

I am indebted to Assistant Prof. Yuji Miyoshi of Department of Electrical and Information Systems, Osaka Prefecture University, for giving me valuable discussions, continuous encouragement, and careful review during the period of this research. He has a great part in shaping my research work and helped me to learn the various skill of academic research.

I would like to give my appreciation to Messrs. Yoshinori Yamamoto, Masaaki Hirano, and Takashi Sasaki of Sumitomo Electric Industries, Ltd for their guidance during my three months internship in the company and also thank them for their valuable advice and help on the research. It was a really significant experience for me, not only for the scientific research work but also for shaping my career path.

I am also greatly indebted to Prof. Tetsuya Takine, Prof. Seiichi Sampei, Prof. Noboru Babaguchi, Prof. Takashi Washio for their guidance regarding my whole tenure in Osaka University.

I express my thanks to Assistant Prof. Yuki Yoshida of Department of Electrical, Electronic, and Information Engineering, Osaka University, for his professional advice. Acknowledgement also goes to many members in Photonic Networks Laboratory (Kitayama Lab), especially to Mr. Pandelis Diamandopoulos and Mr. Gihan Weerasekara, who have given me very valuable suggestions about

this thesis.

I wish to acknowledge the Ministry of Education, Culture, Sports, Science and Technology (MEXT) for their grants and financial support.

I extend many thanks to my friends who made the realization of this thesis more pleasant with their company. Their cooperation was helpful to face the challenges and stress, and eventually it gave me confidence and stamina to accomplish the doctoral program. I would like to thank my parents, Qingmin Huang and Xiuxian Yang, their understanding, supports and endless love let me full of power to complete the graduate study in Japan.

Contents

Chapter 1

Introduction

1.1 Optical networks

Optical networks are characterized by high-capacity, which consist of optical fiber links and optoelectronic or all-optical nodes. As shown in Fig. 1.1, optical networks are classified as a three-level hierarchy consisting of long-haul core networks, regional/metropolitan networks, and access networks [1]. The transmission links in the long-haul core networks transport large amount of data over a long distance (>1000km), classed as wide area networks (WANs). The interlinks between the access and the core networks are regional and metropolitan networks. Such metro area networks (MAN) provide a less amount data transport within a smaller geographical region. The infrastructure of an access network is generally not shared by a large number of end users, such networks are predominantly engineered to provide a low-cost solution [2]. Typical transmission distances of different types of optical networks are listed in Table 1.1 [3].

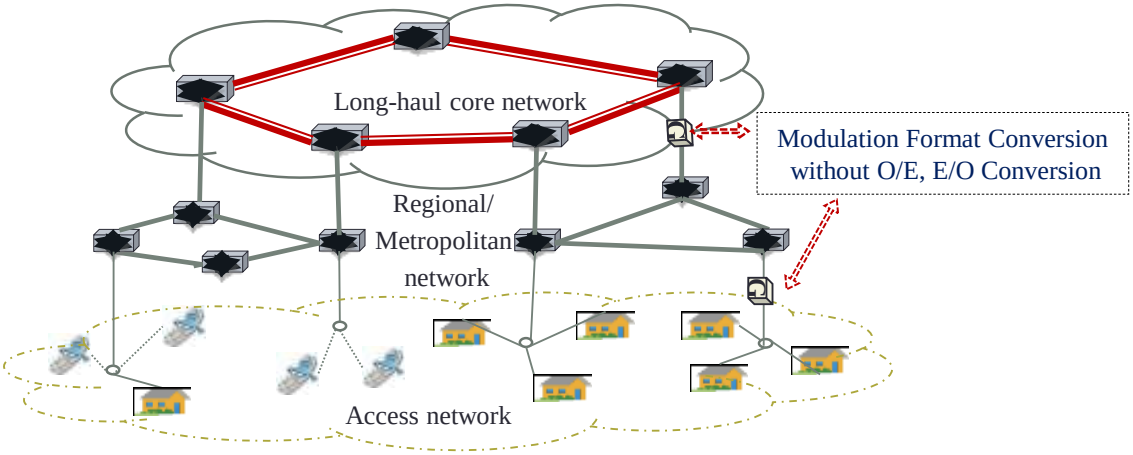

Fig. 1.1 Optical network hierarchy.

In fiber-optic communications, wavelength-division multiplexing (WDM) is a technology that multiplexes a number of optical signals in a single optical fiber by using different wavelengths. The WDM transmission link can transport large amount of data traffic, therefore the use of WDM allows for a manifold increase in the capacity of optical transmission systems. Or, maybe even more importantly, it allows for a tremendous decrease in the cost of the transmitted bandwidth, i.e., the cost per transmitted bit, since optical transmission link amplifiers can be shared by all of the WDM channels through one fiber.

The growth of the Internet traffic in all market segments, such as residential and enterprise wired and wireless services, is showing double digit annual growth. Facing this annual growth rates of 35% to 85% around the world, low cost, ultra-high transmission capacity growth are an active demand for the entire telecommunication infrastructure [4]. Network planners have three options to increase the optical transmission capacity: move to higher transmission rates, add more wavelengths, and install new fibers [5]. Nowadays, erbium doped fiber amplifiers (EDFAs) are generally employed in WDM transmission systems, where the scalable bandwidth of the WDM system is limited by the gain spectrum of an EDFA. For the dense wavelength-division multiplexing (DWDM) system with the standard 50GHz grid per channel, achieving higher channel data bit rates in DWDM systems become urgent [6, 7].

Table 1.1. Classification of optical network transmission systems [2].

System	Distance (km)
Access	<20
Metro	<300
Regional	300-1,000
Long-haul	1,000-3,000
Ultra long-haul	>3,000

For decades, on-off keying (OOK) modulation format has been employed in fiber-optic networks. The I-Q constellation map of OOK is shown in Fig. 1.2. It is a binary amplitude shift keying (BASK) which can be directly received by a square-law detector. In large capacity DWDM networks, OOK-modulated transmission links are typically operated at channel data rates of up to 10 Gb/s. However, the main disadvantage of OOK modulation format is its low tolerance against inter-symbol interference (ISI). ISI is a form of distortion where neighboring symbols interfere with each other that induce a sensitivity penalty to the quality of the received data. Main causes of ISI are linear impairments such as chromatic dispersion (CD) and polarization mode dispersion (PMD). The channel data rates of OOK-modulated DWDM system could not be further increased to 40 Gb/s, because a high baud-rate reduces the tolerance against ISI. Even when duobinary modulation is used

to increase the tolerance to ISI [8, 9], the maximum tolerance to CD and PMD are 300 ps/nm and 3.5 ps, respectively, for 40 Gb/s [10]. The feasible spectral efficiency (SE) is limited to 0.5 b/s/Hz without and 1 b/s/Hz with duobinary modulation [11]. With the need for higher DWDM data bit rates per single channel and a higher spectral efficiency, the fiber-optic community has seen a rapid shift away from OOK and direct-detection receivers.

The recent development of high-speed complementary metal-oxide-semiconductor (CMOS) integrated circuits has made the use of digital signal processing (DSP) in optical transmission extremely attractive. The improved performance of CMOS analog to digital converter (ADC), digital to analog converter (DAC) and DSP techniques have made it feasible to design single-chip CMOS coherent receivers and transceivers with low power consumption [12]. The optical coherent receiver down-converts the whole optical signal linearly to an electrical signal by means of heterodyne or homodyne detection. Meeting the ever-increasing bandwidth demand, single-carrier multi-level modulation (modulated on both amplitude and phase) based on optical coherent technologies become to be the key means to achieve a high SE [13, 14]. For multi-level modulation using M levels, where each symbol carries $\log_2 M$ bits. The linear transmission impairments of CD and PMD can be compensated by DSP at the coherent receiver. Replacement of the OOK formats with the multi-level modulation formats such as phase shift keying (PSK) and 16 or 64 quadrature amplitude modulation (16, 64QAM) formats is the main solution to scale the WDM channel capacity from 10G to 40G/100G and later to 400G [15, 16].

1.2 All-optical modulation format conversion

The development of multi-level modulation, preferably in combination with digital coherent detection technologies, is important for enabling efficient lightwave transmission of high-bit rate services, such as 40G optical transport network (OTN) and 100G Ethernet [17]. However, the conventional OOK modulation format will never be completely replaced by the multi-level modulation formats in optic-fiber networks, due to its absolute advantages such as a cost-effective and simple TX/RX structure and robustness against nonlinear impairments. The 100G transmission system will not completely replace 40G/10G any time soon, but these two technologies may be suitably incorporated together under consideration of cost efficiency [18]. A comparison of the system performance employing various types of modulation formats has been made [19-23] in order to face the demands of high transmission capacity, better system reliability, and optimum operation conditions [24]. Depending on the size and requirement of the future optical networks, the modulation formats may be selectively used [25]. In such situations, modulation format conversion will be required between networks separately employing distinct modulation formats.

To accommodate coming broadband networks, very high-speed signal processing technologies

must be developed not only for transmission lines, but also for transmission nodes. In network nodes, received optical signals are firstly converted into electrical signals and then forwarded again to suitable ports after being converted from the electrical signal to optical signal again. However, this optical-to-electrical (O/E) and electrical-to-optical (E/O) conversions need much power consumption and the bandwidth of the electrical components is limited by tens of GHz at present. All-optical nodes do not need any O/E and E/O conversions by use of low-cost transparent light paths. Thus, optical networks with all-optical network nodes potentially allow high-speed optical communications to become cost effective [26]. The advantages of processing the signal in the all-optical domain include its latency-free operation and tremendous available bandwidth, translated into ultra-high processing speeds that are not possible otherwise [27]. Aiming at realization of high-speed transparent gateway nodes and flexible network design, the function of all-optical modulation format conversion should be an important interface technology [28]. Until now, all-optical methods for modulation format conversions between non-return-to-zero (NRZ) and return-to-zero (RZ) pulse shape [29-32], between OOK and multi-level modulation formats have been widely proposed.

One of multi-level modulation formats is PSK which modulates lightwave phase. Compared with OOK format, PSK format owns a better performance and more robustness against transmission impairments [33]. The quadrature phase shift keying (QPSK) format can enhance the spectral efficiency by a factor of approximately two, compared with the binary phase shift keying (BPSK) data formats [34, 35]. The coherent-detected polarization-multiplexed (CP)-QPSK is likely to become the next standard for long-haul optical transmission systems with 100 Gb/s owning to its advantages as the compatibility with a 50GHz channel grid and compensation of linear transmission impairments enabling dispersion unmanaged transmission [36, 37]. The successful transmission of 45.8 Gb/s CP-BPSK over 9,420 km of legacy submarine fiber was reported in [38]. The increase in the transmission distance also implies cost reduction by eliminating regeneration points through transmission links. The I-Q constellation maps of BPSK and QPSK formats are shown in Fig. 1.2.

The nonlinear effect of cross phase modulation (XPM) has been extensively used for OOK to PSK format conversion owning to its function of power-dependent phase modulation [39-41]. The technologies of all-optical OOK to BPSK/QPSK at 40 Gb/s have been proposed in [42]. The all-optical NRZ-OOK to 8 amplitude phase shift keying (APSK) format conversion was proposed in [43]. In this method, the XPM and optical parametric amplification (OPA) in optical fibers were employed to achieve power-dependent phase and amplitude modulation onto probe light. XPM in a Mach-Zehnder interferometer (MZI) configuration with parallel semiconductor optical amplifiers (SOAs) was also employed to realize OOK to BPSK converters at 10.7 GS/s [44]. As a part of the research work of this thesis, RZ-OOK to RZ-BPSK modulation format conversion employing XPM will be demonstrated at 10.7 Gb/s.

The 16QAM modulation format is another attractive multi-level modulation format which carries four bits per symbol and possess outstanding performance of transmission capacity. Its constellation map is shown in Fig. 1.2. Until now, the highest SE of 6.4 b/s/Hz has been achieved by employing 16QAM format, then, 69.1 Tb/s transmission over 240-km low-loss pure silica core fibers have been demonstrated in a WDM system employing wideband amplifiers [45-48]. Also, 16QAM-format-based optical time division multiplexing (OTDM) systems are widely employed to realize single-wavelength-channel Multi-Tb/s high-data capacity transmission [49, 50]. All of the above researches confirm the potentiality of 16QAM for the next generation transmission systems of higher than 100G. However, its large constellation size significantly reduces its tolerance against noise and nonlinear impairments, and thus limits the feasible transmission reach. One conclusion is that 16QAM format may be more suitable for metro deployments. Researchers will unremittingly explore the practicability of 16, 32 or 64QAM format achieving 400G transmission capacity in WANs with a cost-effective manner. On the other hand, the conventional OOK formats may keep their main role in MANs and access network or rarely incorporate with the multi-level modulation formats in the WANs. The function of OOK to 16QAM format conversion will be an important interface technology for gateway nodes between optimum designed WAN and MAN (or MAN and access network) separately employing different modulation formats. With the above background, this thesis proposes all-optical OOK to 16QAM modulation format conversion employing nonlinear optical loop mirror (NOLM) for the first time.

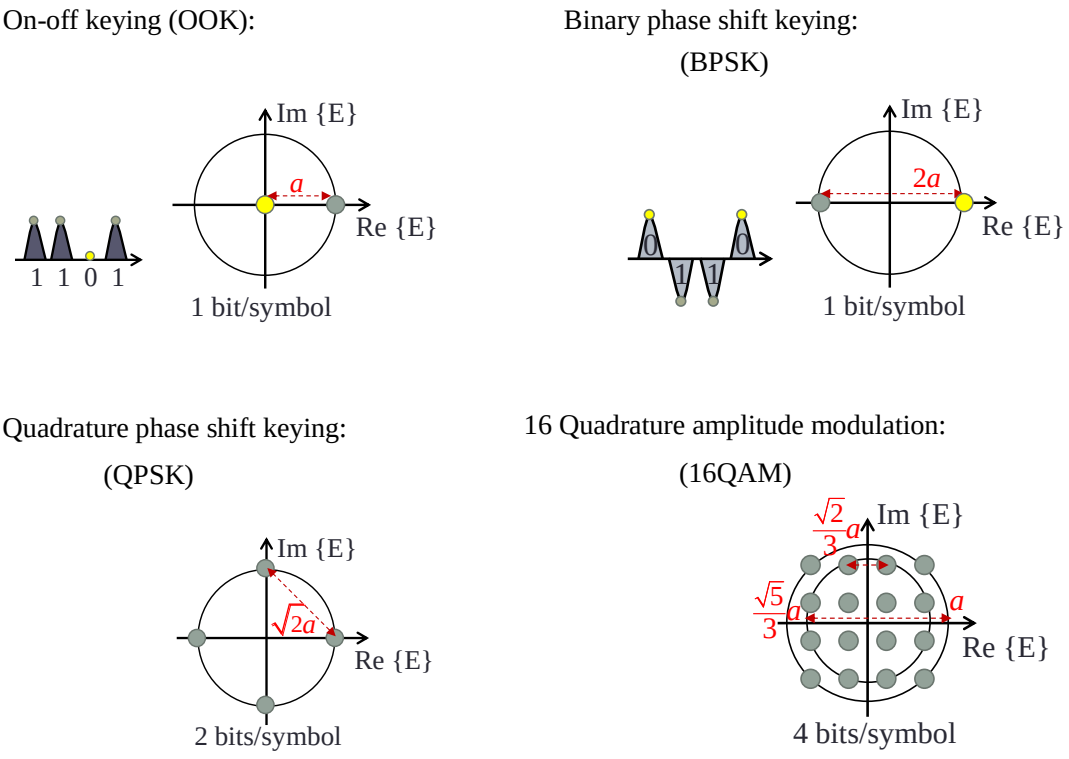

Fig. 1.2 I-Q constellation maps of OOK, BPSK, QPSK and 16QAM formats.

1.3 Objective

The objective of this thesis is to develop technologies contributing to enlarge the network capacity by enhancing the throughput in gateway nodes and the network flexibility on choosing an optimized modulation format. With the development of digital coherent technologies, multi-level modulation formats such as PSK and 16QAM have become a key mean to achieve large capacity networks. The OOK format may keep its main role in MAN, and access network or rarely incorporate with multi-level modulation format in the WAN because of its cost efficiency. All-optical methods of OOK to multi-level modulation format conversion can be an important interface technology to realize a transparent gateway node between MAN and WAN (or MAN and access network) separately employing distinct modulation formats. The optical nonlinearities in SOAs and optical fibers are usually employed to realize all-optical modulation format conversion [39-44]. However, the pattern effect in SOAs has to be compensated which can seriously impair the performance of high-speed signal processing systems [51]. The operation speed will be limited by its slow recovery speed. This thesis focuses on the fiber nonlinearity, which has a very fast response time, and its applicability for high-speed signal processing system. Aiming at realizing a transparent gateway node for higher than 100 Gb/s signal benefit from the ultrafast response time of fiber nonlinear effects which could be faster than sub-picoseconds.

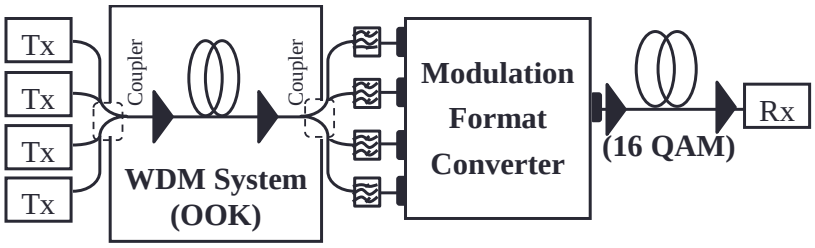

Fig. 1.3 Operation system of four-channel OOK WDM system to 16QAM format converter

The framework of this thesis is as follows:

Firstly, a novel method measuring optical fiber nonlinear coefficient γ with high precision will be proposed. The efficiency of the nonlinear effects depends on the fiber's nonlinear coefficient γ, thus accurate measurement of γ is one of the important issues for designing transmission systems and highly nonlinear fiber (HNLF)-based devices.

Then, an all-optical OOK to 16QAM modulation format converter based on fiber nonlinear effects

will be proposed. The configuration of a system using the proposed converter is shown in Fig. 1.3. WDM signals modulated by OOK format are demultiplexed at a gateway node, where modulation format converters convert the four OOK channels to a 16QAM signal in the optical domain. Numerical simulations and experiments for the proposed converter will be demonstrated to verify its feasibility and evaluate the performance.

1.4 Thesis structure

Chapter 2 overviews the necessary knowledge for good understanding of the OOK to 16QAM format conversion. The nonlinear Schrödinger (NLS) equation helps us to theoretically understand how nonlinear effects are generated in optical fiber. The fiber's nonlinear effects of XPM and four-wave mixing (FWM) are employed in the OOK to 16QAM modulation format conversion. A NOLM, which is the most important part of the converter, is attractive for its application in all-optical signal processing in fiber-optic communications. The related research and the transfer function of NOLM will also be briefly explained.

In Chapter 3, a novel method to measure fiber nonlinear coefficient γ by phase-mismatching (PM)-FWM will be proposed. The PM-FWM method can simultaneously measure the CD with a high precision, and therefore its influence on the measurement of γ can be removed. The measurements for highly nonlinear dispersion-shifted fibers (HNLDSFs) and a standard single mode fiber (SSMF) will be made by the PM-FWM method. Comparing the measured results with ones measured by a conventional method, the practicability of the PM-FWM method was dedicated.

In Chapter 4, RZ-OOK to RZ-BPSK modulation format conversion employing XPM will be experimentally demonstrated at first. The dispersion tolerance of the converted BPSK signal and the time tolerance of the converter will be evaluated. Then, a novel all-optical OOK to 16QAM modulation format conversion employing a NOLM and OPA in optical fibers will be proposed and numerically demonstrated. The influence of the pulse shape of the OOK signals will be discussed because the pulse shape is an important factor when employing the XPM effect. The peak power of control lights is a key parameter in these nonlinear effects, so that the power tolerance will also be analytically evaluated.

Chapter 5 describes a simplified configuration of the converter with a 1:2 coupler employed in the NOLM. The first experimental demonstration of all-optical modulation format conversion from NRZ-OOK to RZ-16QAM will be presented at 10 GS/s. Since the OOK signals should be amplified to high power before launched onto a HNLF for amplitude-to-phase conversion, amplified spontanesous emission (ASE) noise from the amplifiers degrades the quality of the converted light

phase. The effect of the ASE noise will be theoretically discussed for further improving the converter performance.

Finally, concluding remarks obtained in this thesis are summarized.

Chapter 2

Optical fiber nonlinearity

Nonlinear Kerr effects in optical fibers originate from the nonlinear refractive index; a phenomenon that refers to the intensity dependence of the refractive index of silica resulting from molecular $\chi^{(3)}$ [52]. The refractive index of a dielectric material can be expressed as

$$\tilde{n}\left(\omega,\left|E\right|^2\right)=n_0\left(\omega\right)+n_2\left|E\right|^2, \tag{2.1}$$

which consists of the linear part n_0 and the nonlinear part $n_2|E|^2$. n_2 represents the nonlinear index related to $\chi^{(3)}$ as $n_2=(3/8n)\mathrm{Re}[\chi^{(3)}]$. $|E|^2$ represents the intensity of incident light. The intensity dependence of refractive index of dielectric materials leads to a number of nonlinear effects. The XPM and FWM will be overviewed in this chapter, assuming co-propagating and co-polarized lightwaves.

The main part of our all-optical OOK to 16QAM format converter, which will be described in detail in Chapter 4, is a NOLM. The transfer function of a NOLM will also be briefly introduced in the last part of this chapter.

2.1 Nonlinear Schrödinger (NLS) equation

The NLS equation describes wave propagation properties in fiber optics [53]. The classical NLS equation for lossless optical fiber is expressed as

$$j\frac{\partial E}{\partial z}-\frac{\beta_2}{2}\frac{\partial^2 E}{\partial t^2}-j\frac{\beta_3}{6}\frac{\partial^3 E}{\partial t^3}+\gamma\left|E\right|^2E=0, \tag{2.2}$$

where *z* and *t* represent the transmission length and time, respectively. The function *E*(*z, t*) represents the complex envelope of the electric field. The second and third terms in the left-hand side in Eq. (2.2) represent the second- and third-order dispersions, respectively, which are introduced by expanding the frequency-dependent propagation constant $\beta(\omega)$ in a Taylor series around the carrier frequency ω_0 as

$$\beta(\omega)=\beta_0+\beta_1(\omega-\omega_0)+\frac{1}{2}\beta_2(\omega-\omega_0)^2+\frac{1}{6}\beta_3(\omega-\omega_0)^3+\cdots, \tag{2.3}$$

where $\beta_0=\beta(\omega_0)$ and the other coefficients are defined as

$$\beta_n=\left(\frac{d^n\beta}{d\omega^n}\right)_{\omega=\omega_0}. \tag{2.4}$$

Usually, terms higher than the third-order in Eq. (2.3) are negligible for $\beta_2\neq 0$ and $|\omega-\omega_0| \ll \omega$. Unless $\beta_2 \sim 0$ for a specific values of ω_0, the third-order dispersion should also be taken into account as in Eq. (2.2). The parameter γ in Eq. (2.2) is the nonlinear coefficient defined as

$$\gamma(\omega_0)=\frac{n_2(\omega_0)\omega_0}{cA_{\mathrm{eff}}}, \tag{2.5}$$

where A_{eff} represents the effective core area and *c* expresses the speed of light in vacuum. The NLS equation models many nonlinearity effects in a fiber, including self-phase modulation (SPM), XPM, FWM, etc.

2.2 Nonlinear effects

2.2.1 Cross-phase modulation (XPM)

XPM is generated from the power-dependence of the core's refractive index of fiber which refers to the nonlinear phase shift of an optical field induced by co-propagating channels at different wavelengths. If two lightwaves with different wavelengths simultaneously propagate inside a fiber, the complex envelope of the electric field E(*z, t*) can be expressed as

$$E(z,t)=\sum_{i=1}^{2}E_i(z)\exp\left[-j(\omega_i-\omega_0)t\right], \tag{2.6}$$

where ω_i (i = 1, 2) is the angular frequency of the transmitted lightwave, and ω_0 is the reference angular frequency in Eq. (2.3). If we suppose that the dispersion parameter β_2 and β_3 in Eq. (2.2) are zero, the fiber nonlinearity is only taken into account. By substituting Eq. (2.6) into simplified Eq. (2.2), the NLS equation can be written as the following set of two coupled NLS equations for separate angular frequency.

$$\begin{aligned} j\frac{dE_1}{dz}+\gamma\left(|E_1|^2+2|E_2|^2\right)E_1=0\ , \\ j\frac{dE_2}{dz}+\gamma\left(|E_2|^2+2|E_1|^2\right)E_2=0\ . \end{aligned} \tag{2.7}$$

Suppose $E_{i,0}$ is the electric field at z=0, then the transmitted $E_i(z=L) = E_{i,0}\exp(j\Phi_i)$ can be obtained from Eq.(2.7) as

$$\begin{aligned} E_1(z=L)&=\sqrt{P_1}\exp\left[j\gamma\left(P_1+2P_2\right)L\right], \\ E_2(z=L)&=\sqrt{P_2}\exp\left[j\gamma\left(P_2+2P_1\right)L\right], \end{aligned} \tag{2.8}$$

where L and P_i ($=|E_{i,0}|^2$) are the fiber length and lightwave input powers, respectively. From Eq. (2.8), the nonlinear phase modulation: SPM in the first and XPM in the second terms which differ by factor 2, depend on its own and the co-propagating lightwave power. Here, we define $\Phi_{\mathrm{SPM}i}$ and $\Phi_{\mathrm{XPM}i}$ as the phase changes induced by SPM and XPM, respectively, which can be expressed as

$$\begin{aligned} \Phi_{\mathrm{SPM\_}i}&=\gamma P_i L\ , \\ \Phi_{\mathrm{XPM\_}i}&=2\gamma P_{3-i}L\ . \end{aligned} \tag{2.9}$$

SPM and XPM impose power-dependent phase modulation onto the transmitted light. This XPM effect possesses a wide range of applications for all-optical signal processing such as OOK to BPSK/QPSK format conversion, ADC, and wavelength conversion etc., where a high power signals and the probe pulse co-propagate through HNLFs. The operation principle of OOK to BPSK/QPSK format conversion is schematically explained in Fig. 2.1. An OOK signal is amplified to a specific power P that induces π and 0 phase shift in a probe pulse train as logical data 1 and 0, respectively. Then, a BPSK signal is generated at the HNLF output with a wavelength identical to the probe pulse train. When an OOK signal that induces $\pi/2$ and 0 phase shift is additionally incident to the HNLF, a QPSK signal is generated. This all-optical RZ-OOK to RZ-BPSK format conversion will be

described in detail in Chapter 4.

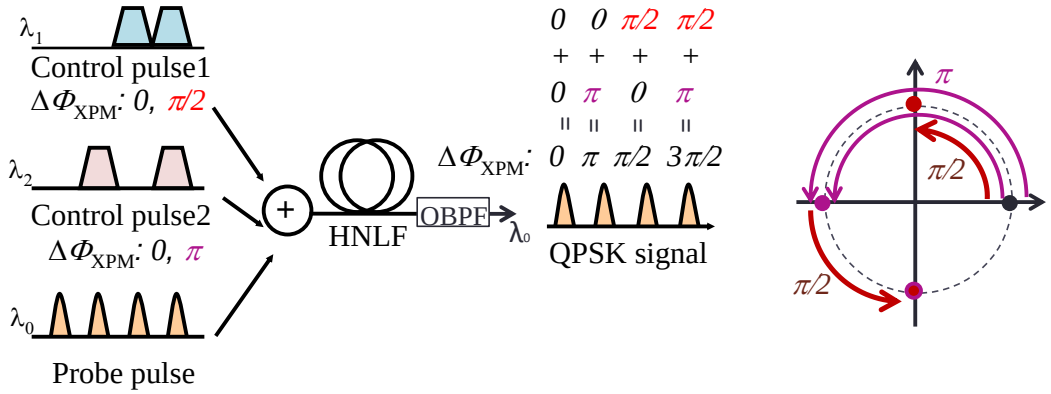

Fig. 2.1 OOK to BPSK/QPSK format conversion based on cross-phase modulation (XPM) in HNLF.

2.2.2 Four-wave mixing (FWM)

In many nonlinear phenomena, an optical fiber plays a passive role except for mediating interaction among several optical waves through a nonlinear response of bound electrons. Such processes are referred to as the parametric processes, which required of the phase-matching for the phenomena to be generated. Nonlinear phenomena such as harmonic generation, FWM, and OPA fall into this category. Different from the XPM effect, a new frequency light is generated in the parametric process.

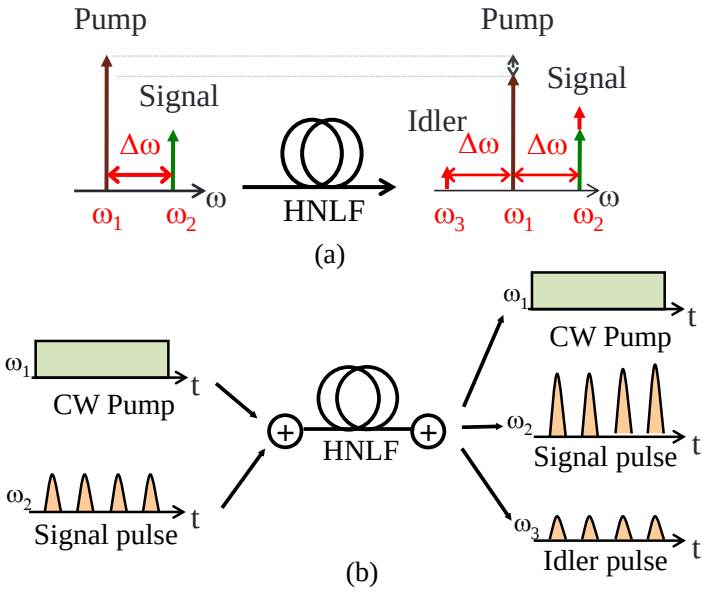

Fig. 2.2 Degenerate four-wave mixing (FWM) in the (a) spectral domain and (b) time domain.

The degenerate FWM is also called as three-wave mixing because only three distinct frequencies are involved in the process as shown in Fig. 2.2. When high-power pump light co-propagates with signal light, idler light is generated. In Fig. 2.2(a), the signal and idler waves are anti- and stokes waves. The angular frequencies of the pump, signal and idler wave are defined as ω_1, ω_2 and ω_3 as shown in Fig. 2.2. The angular frequency difference between these three waves satisfies $\Delta\omega = \omega_1 - \omega_3 = \omega_2 - \omega_1$. The complex envelope of the electric field E(*z, t*) that consists of the three waves can be expressed as

$$E(z,t) = \sum_{i=1}^{3} E_i(z) \exp\left[-j(\omega_i - \omega_1)t\right], \tag{2.10}$$

where the pump angular frequency ω_1 is set to be the reference frequency ω_0 in Eq. (2.3). Equations for $E_i(z)$ can be derived by substituting Eq. (2.10) into Eq. (2.2). With an assumption that pump power (P_{pump}) is extremely larger than signal (P_{signal}) and idler power (P_{idler}), i.e., $P_{\text{pump}} >> P_{\text{signal}}$, P_{idler}, and thus un-depleted, the three coupled equations can be derived as

$$j\frac{dE_1}{dz} + \gamma |E_1|^2 E_1 = 0, \tag{2.11}$$

$$j\frac{dE_2}{dz} + \left[\frac{\beta_2}{2}(\Delta\omega)^2 + \frac{\beta_3}{6}(\Delta\omega)^3\right]E_2 + \gamma\left[2|E_1|^2 E_2 + (E_1)^2 (E_3)^*\right] = 0, \tag{2.12}$$

$$j\frac{dE_3}{dz} + \left[\frac{\beta_2}{2}(\Delta\omega)^2 - \frac{\beta_3}{6}(\Delta\omega)^3\right]E_3 + \gamma\left[2|E_1|^2 E_3 + (E_1)^2 (E_2)^*\right] = 0. \tag{2.13}$$

SPM dominates in the pump light because of high pump power. The components of $(E_1)^2(E_3)^*$ and $(E_1)^2(E_2)^*$ in Eqs. (2.12) and (2.13) imply the degenerated FWM process. By solving Eq. (2.11), the transmitted electric field of the pump light can be expressed as

$$E_1(z) = \sqrt{P_1}\exp(j\theta_1 z) = \sqrt{P_1}\exp(j\gamma P_1 z). \tag{2.14}$$

By substituting Eq. (2.14) into Eqs. (2.12) and (2.13), two coupled equation for the signal and idler fields can be obtained as

$$\begin{aligned} j\frac{dE_2}{dz} + \left[\frac{\beta_2}{2}(\Delta\omega)^2 + \frac{\beta_3}{6}(\Delta\omega)^3 + 2\gamma P_1\right]E_2 + \gamma P_1 (E_3)^* \exp(j2\theta_1) = 0, \\ j\frac{dE_3}{dz} + \left[\frac{\beta_2}{2}(\Delta\omega)^2 - \frac{\beta_3}{6}(\Delta\omega)^3 + 2\gamma P_1\right]E_3 + \gamma P_1 (E_2)^* \exp(j2\theta_1) = 0. \end{aligned} \tag{2.15}$$

To solve these equations, we introduce

$$E_2 = E'_2 \exp\left(j\theta_2 z\right) = E'_2 \exp\left\{ j\left[\frac{\beta_2}{2}\left(\Delta\omega\right)^2 + \frac{\beta_3}{6}\left(\Delta\omega\right)^3 + 2\gamma P_1 \right] z \right\},$$
$$E_3 = E'_3 \exp\left(j\theta_3 z\right) = E'_3 \exp\left\{ j\left[\frac{\beta_2}{2}\left(\Delta\omega\right)^2 - \frac{\beta_3}{6}\left(\Delta\omega\right)^3 + 2\gamma P_1 \right] z \right\}. \tag{2.16}$$

Then, substituting Eq. (2.16) to Eq. (2.15), we obtain

$$\frac{dE'_2}{dz} = j\gamma P_1 \left(E'_3\right)^* \exp\left(-j\Delta\beta z\right),$$
$$\frac{dE'_3}{dz} = j\gamma P_1 \left(E'_2\right)^* \exp\left(-j\Delta\beta z\right), \tag{2.17}$$

where $\Delta\beta$ represents the phase-mismatching parameter given by

$$\Delta\beta = \theta_2 + \theta_3 - 2\theta_1 = \beta_2\left(\Delta\omega\right)^2 + 2\gamma P_1 . \tag{2.18}$$

In the above, the odd order terms in Eq. (2.3) are eliminated. When $|\beta_2|$ is very small, the forth-order term in Eq. (2.3) should be also taken into account. With initial conditions of $E'_2\left(z=0\right) = E'_{2,0}$ and $E'_3\left(z=0\right) = 0$, the solution of Eq. (2.17) can be obtained as

$$E'_2\left(z=L\right) = \frac{E'_{2,0}}{2g}\left\{2g\cosh\left(gL\right) + j\Delta\beta\sinh\left(gL\right)\right\}\exp\left[-j\frac{\Delta\beta L}{2}\right],$$
$$E'_3\left(z=L\right) = j\frac{\gamma P_1}{g}\left(E'_{2,0}\right)^*\sinh\left(gL\right)\exp\left[-j\frac{\Delta\beta L}{2}\right], \tag{2.19}$$

where g is the pump power dependent parametric gain defined as

$$g = \sqrt{\left(\gamma P_1\right)^2 - \left(\frac{\Delta\beta}{2}\right)^2} . \tag{2.20}$$

The powers of the transmitted signal P_2 and the generated idler P_3 depend on the phase-mismatching

$\Delta\beta$ as

$$P_2(z=L)=P_{2,0}\left\{1+\frac{(\gamma P_1)^2\sinh^2(gL)}{g^2}\right\},$$
$$P_3(z=L)=\frac{P_{2,0}(\gamma P_1)^2\sinh^2(gL)}{g^2}, \tag{2.21}$$

where $P_2(z=0)=P_{2,0}$. The FWM process in the time domain is shown in the right of Fig. 2.2(b). At the output of the HNLF, signal light will be amplified. This amplification process is called OPA [54-57]. The gain bandwidth of the OPA can be increased to 5 THZ and beyond by careful optimization of the parameters related to the phase-mismatching. Usually, γ >10/W/km and the pump wavelength close to the zero-dispersion wavelength for low β_2 of the fiber are required for achieving large gain bandwidth. The generated idler light was widely employed for all-optical wavelength conversion, where the conversion efficiency also depends on the phase-mismatching $\Delta\beta$.

2.3 Nonlinear optical loop mirror (NOLM)

All-optical signal processing is expected to play major role in future optical communication systems. A NOLM is a valuable tool in the optical signal processing. It is a fiber-optic device in which a coupler splits the input into two lightwaves that travel in the opposite directions in a fiber-optic loop. The clockwise and counter-clockwise lightwaves in the loop acquire different phases due to the nonlinearities in the optical medium. The transfer function of a NOLM employing 1:1 coupler is [58]

$$\frac{E_{\text{out}}}{E_{\text{in}}}=\sin\left(\frac{\Delta\Phi}{2}\right)\exp\left(-j\frac{\Delta\Phi}{2}\right), \tag{2.22}$$

where $\Delta\Phi$ is the relative phase difference between the clockwise and counter-clockwise input lights. The NOLM is also called fiber Sagnac interferometer. The output power is zero for $\Delta\Phi=0$ and equals to the input power for $\Delta\Phi=\pi$ due to destructive and constructive interferences, respectively. When the phase difference is 0, the light comes back from the input port of the coupler like a mirror. Different from a fiber based MZI, the phase drift between the clockwise and counter-clockwise input lights is cancelled out thanks to a loop configuration.

The SPM based NOLM is shown in Fig. 2.3. An optical attenuator is inserted between the 1:1

coupler and the HNLF in order to make the power level of the clockwise and counter-clockwise pulses imbalance in the HNLF, so that the power difference is converted to phase difference $\Delta\Phi$.

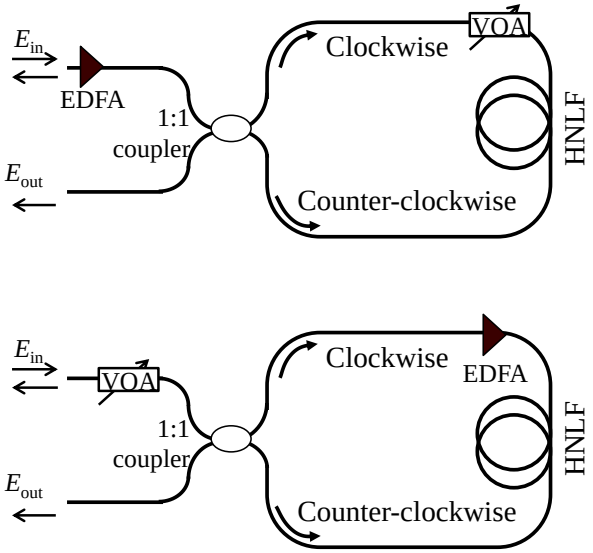

EDFA: Erbium doped fiber amplifier
VOA: Variable optical attenuater
HNLF: Highly nonlinear fiber

Fig. 2.3 SPM based NOLM.

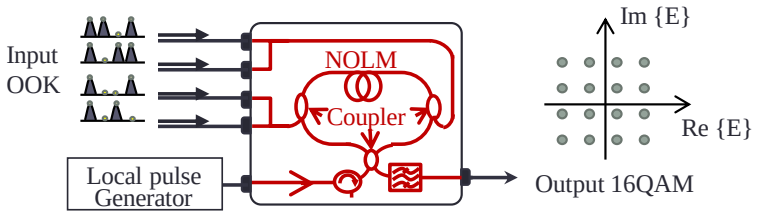

Fig. 2.4 The configuration of the OOK to 16QAM format converter employing a NOLM.

Applications of NOLM for all-optical signal processing in fiber-optic communications includes:

- Analog to digital converter (ADC) [58],
- Wavelength converter [59-61],
- Modulation format converter,
  RZ-to-NRZ or NRZ-to-RZ format converter [62],
- 2R regeneration (Re-amplification, Reshaping) [63, 64], etc.

The NOLM-based all-optical OOK to 16QAM format conversion will be proposed as the main research work in this thesis. Fig. 2.4 shows its configuration. Four OOK signals are coupled into a

NOLM in the clockwise and counter-clockwise directions to modulate the phase of a local pulse via XPM. An optical bandpass filter (OBPF) was used to filter out the OOKs, and output the 16QAM signal. The principle will be described in detail in Chapter 4.

2.4 Conclusion

In this chapter, the NLS equation and the nonlinear effects of XPM and FWM, which are employed in our all-optical OOK to 16QAM format converter, have been introduced. A NOLM is a valuable tool in all-optical signal processing. Different from an all-fiber based MZI, the phase drift between the clockwise and counter-clockwise lights can be cancelled out thanks to a loop configuration. The transfer function of the NOLM employing 1:1 OC and its applications have been also briefly described.

Chapter 3

PM-FWM method for measuring optical fiber's nonlinear coefficient

Accurate measurement of the nonlinear coefficient γ is an important issue for applications of nonlinear phenomena. In this chapter, the conventional methods measuring optical fiber's nonlinear coefficient γ will be overviewed. The continuous wave (CW)-SPM method has been widely employed for the measurement which features simplicity. Unfortunately, however, the influence from CD should be taken into account in this method, which is not easy in fact. For researchers in this field, developing a measuring method of the fiber's nonlinear coefficient γ is an unfinished task. A new method based on PM-FWM with a simple operation setup will be described. The CD of the fiber can be simultaneously measured with a high precision by PM-FWM method proposed in [65], and therefore its influence on the γ measurement can be removed.

3.1 Introduction

The implementation of EDFAs and CD compensation allows long distance data transmission. Along with the WDM technique, this leads to an large amount of power inside the fiber over long distances, and optical nonlinearities start to play a significant role. In large-capacity ultra-long haul transmission systems utilizing digital coherent detection, a major concern is their high sensitivity to nonlinear impairments caused by Kerr effects in optical fibers including SPM, XPM, and FWM. On the other hand, HNLFs have been widely applied to all-optical signal processing due to their ability to efficiently generate nonlinear effects [66]. The efficiency of the nonlinear effects depends on the fiber nonlinear coefficient γ, which is defined as $2\pi n_2/(\lambda \cdot A_{\text{eff}})$, where n_2, λ, and A_{eff} are the nonlinear

refractive index, the wavelength, and the effective core area, respectively. Therefore, accurate measurement of γ is one of the important issues for designing fiber transmission systems and HNLF-based devices.

A number of methods measuring the nonlinear coefficient γ have been reported so far.

- Spectral broadening of short pulses due to the phase chirp induced by SPM [67] or XPM [68] were employed to measure the nonlinear coefficient γ. In this method, the critical assumption on the pulse shape and complex de-convolution calculation are required.

- Interferometric methods [69, 70] were proposed, which is based on interferometric measurement of the SPM or XPM induced phase shift acquired by a laser pulse along a fiber under test. A detection made by an all-fiber self-aligned interferometer incorporating a Faraday mirror was proposed in [71]. The self-aligned setup allows an easy and quick initial adjustment of the interferometer and leads to a good robustness against environmental perturbation since the two interferometer arms are always automatically matched. In this method, the high precision nonlinear coefficient γ measurement was achieved by detecting the phase change. However, the measurement setup is too complicated.

- The CW-SPM method [72] has a simple measurement setup. In this method, two CW lights with a small wavelength difference are employed to generate a beat signal. During the beat signal transmission through a test fiber, SPM generates modulation sidebands in the optical spectrum. The nonlinear coefficient can be evaluated by calculating the intensity ratio of the first-order sideband to the fundamental frequency component. Unfortunately, however, the measurement accuracy may suffer from fiber CD. To neglect the influence of CD, the length of a test fiber should be limited to be less than 500m for standard single mode fiber (SSMF).

- The FWM idler power was used to evaluate the nonlinear coefficient γ of 12.5km-long dispersion shifted fiber (DSF) [73]. However, it might be difficult to measure small γ of large CD fibers such as SSMF or short fibers because of the low FWM efficiency.

A novel method to measure γ by PM-FWM using a simple setup was proposed. In this method, frequency shifts satisfying the phase-mismatching described by Eq. (2.18) for FWM are used to measure γ. The PM-FWM method can simultaneously measure the chromatic dispersion with high precision [65], and therefore is free from the influence of CD. Using the proposed method, we demonstrate γ measurements for HNLDSFs. In addition, γ and CD of a 1km-long SSMF having low nonlinearity and large CD are also measured with the same setup.

3.2 Operation principle of PM-FWM method

When a pump and a probe lights with angular frequencies of ω_{pump} and ω_{probe}, respectively, propagate together through a fiber, an idler light is generated at a frequency of $2\omega_{pump} - \omega_{probe}$ through the FWM process. For linearly co-polarized lights propagating in a fiber, the output power of the idler light, P_{idler}, is given by Eq. (2.21). For $\Delta\beta >> \gamma P_{pump}$ in Eq. (2.20), Eq. (2.21) can be simplified as

$$P_{idler} = \left(\gamma P_{pump} L\right)^2 P_{probe} \mathrm{sinc}^2\left(\frac{\Delta\beta L}{2}\right), \tag{3.1}$$

where L, P_{pump}, and P_{probe} are the fiber length, the launched pump and probe powers, respectively. $\Delta\beta$ is the phase-mismatching parameter given by Eq. (2.18), where β_2 represents the second-order dispersion at pump frequency ω_{pump}, and $\Delta\omega = \omega_{probe} - \omega_{pump}$ is an angular frequency difference between the pump and the probe.

Here, we propose two schemes for measuring γ based on the PM-FWM, depending on β_2 of a tested fiber. For a low β_2 fiber, whose zero-dispersion wavelength is within or close to the measuring wavelengths, ω_{pump} is scanned while keeping $\Delta\omega$ constant. On the other hand, for a high β_2 fiber, ω_{pump} and therefore β_2 are kept constant while ω_{probe} is scanned to change $\Delta\omega$.

I. Low β_2 fiber

For constant $\Delta\omega$ in Eqs. (2.18) and (3.1), P_{idler} is a periodic function of ω_{pump} as shown in Fig. 3.1(a) because β_2 monotonically increase or decrease with ω_{pump}. From Eq. (3.1), P_{idler} is maximum at $\Delta\beta L/2=0$, and has minimal values at which $\Delta\beta$ satisfies

$$\frac{\Delta\beta L}{2} = \mathrm{N}\pi \ \left(\mathrm{N}:\mathrm{integer}\right). \tag{3.2}$$

For the limit of P_{pump} to be zero, β_2 at a pump frequency of $\omega_Z^{(N)}$ providing the minimal P_{idler}, $\beta_{2z}^{(N)}$ can be expressed as [8]

$$\beta_{2Z}^{(N)} = \frac{2\mathrm{N}\pi}{\left(\Delta\omega\right)^2 L}. \tag{3.3}$$

where the forth-order dispersion β_4 was not taken into account since β_2 in Eq. (3.2) should be large enough. In case of $P_{pump} > 0$, the pump frequency giving minimum P_{idler} shifts to $\omega_P^{(N)}$ as shown by

the solid curve in Fig. 3.1(a). Here, β_2 at $\omega_P^{(N)}$, $\beta_{2P}^{(N)}$ can be approximated by using the third-order dispersion at $\omega_Z^{(N)}$, $\beta_{3Z}^{(N)}$ as

$$\beta_{2P}^{(N)} = \beta_{3Z}^{(N)} \left(\omega_P^{(N)} - \omega_Z^{(N)} \right) + \beta_{2Z}^{(N)}. \tag{3.4}$$

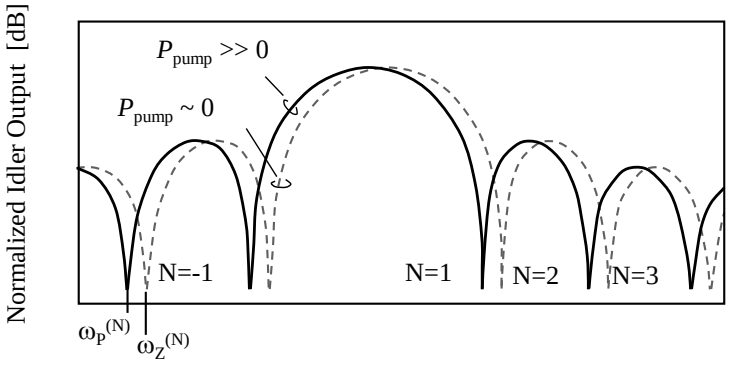

(a)

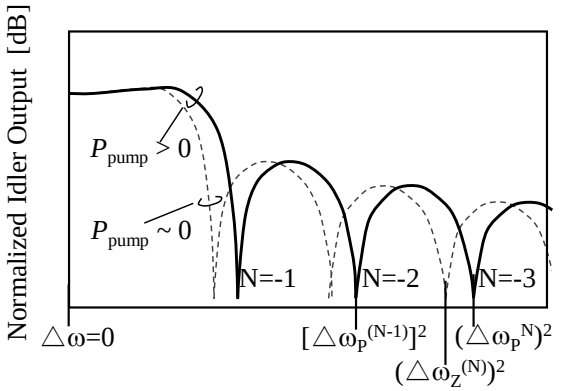

(b)

Fig. 3.1 Idler output power as a function of (a) pump angular frequency with a constant angular frequency difference, and (b) squared angular frequency difference with a constant pump angular frequency.

Substituting Eqs. (2.18) and (3.4) into Eq. (3.2), $\omega_P^{(N)}$ can be expressed as

$$\omega_P^{(N)} = -\frac{2\gamma}{\beta_{3Z}^{(N)} (\Delta\omega)^2} P_{pump} + \omega_Z^{(N)}, \tag{3.5}$$

As a corollary, $\omega_P^{(N)}$ becomes a linear function of P_{pump}, and the nonlinear coefficient γ can be calcu-

lated as

$$\gamma = -\frac{\beta_{3Z}^{(N)}}{2}(\Delta\omega)^2 \frac{\partial \omega_P^{(N)}}{\partial P_{pump}}. \tag{3.6}$$

Therefore, γ at $\omega_P^{(N)}$ can be determined from the slope of the $\omega_P^{(N)}$ versus P_{pump} graph. Here, $\beta_{3Z}^{(N)}$ in Eq. (3.6) can be also obtained using Eq. (3.2). Although the condition of P_{pump}= 0 in Eq. (3.2) would be impossible for actual measurement, $\omega_Z^{(N)}$ can be estimated by calculating the y-intercept on the $\omega_p^{(N)}$ versus P_{pump} graph in Eq. (3.5). β_2 spectrum can be also determined with $\beta_{2z}^{(N)}$ for several N from Eq. (3.3), and $\beta_{3Z}^{(N)}$ can be then calculated by a biquadrate approximation of the β_2 spectrum. The definitions of β are summarized in Table 3.1.

Table 3.1. Definitions of β

$\Delta\beta$	β_2, β_3	$\beta_{2Z}^{(N)}$, $\beta_{2P}^{(N)}$	$\beta_{3Z}^{(N)}$
Phase mismatching parameter	2nd-, 3rd-order dispersion at ω_{pump}	β_2 at $\omega_Z^{(N)}$, $\omega_P^{(N)}$	β_3 at $\omega_Z^{(N)}$

II. High β_2 fibers

When we measure high β_2 fibers such as SSMF at wavelengths around 1550 nm, it is difficult to exactly know N in Eq. (3.3) because the measured frequencies are far away from the frequency at which $\Delta\beta L/2$=0 and N becomes a large value, and therefore, $\beta_{3Z}^{(N)}$ in Eq. (3.6) cannot be obtained. Here, keeping ω_{pump} constant, only $\Delta\omega$ and P_{pump} become variables in Eq. (2.18). In this case, P_{idler} is also a periodic function of the squared frequency difference $(\Delta\omega)^2$ as shown in Fig. 3.1(b). From Eqs. (2.18) and (3.2), the conditions for P_{idler} to be minimum are given by

$$\beta_2\left[\Delta\omega_P^{(N)}\right]^2 + 2\gamma P_{pump} = \frac{2N\pi}{L}, \tag{3.7}$$

$$\beta_2\left[\Delta\omega_P^{(N-1)}\right]^2 + 2\gamma P_{pump} = \frac{2(N-1)\pi}{L}, \tag{3.8}$$

where $\Delta\omega_P^{(N)}$ is the N-th frequency difference providing the minimal P_{idler} for P_{pump}. From two adjacent frequency differences of $\Delta\omega_P^{(N)}$ and $\Delta\omega_P^{(N-1)}$ in Eqs. (3.7) and (3.8), β_2 at ω_p can be determined independently of N as

$$\beta_2 = -\frac{2\pi}{\left\{\left[\Delta\omega_P^{(N-1)}\right]^2 - \left[\Delta\omega_P^{(N)}\right]^2\right\}L}. \tag{3.9}$$

Similar to Eq. (3.3), a frequency difference $\Delta\omega_z^{(N)}$ which provides the minimal P_{idler} for the limit of P_{pump} to be zero is given by

$$\left[\Delta\omega_Z^{(N)}\right]^2 = \frac{2N\pi}{\beta_2 L}. \tag{3.10}$$

From Eqs. (3.7) and (3.10), the following equation is obtained:

$$\left[\Delta\omega_P^{(N)}\right]^2 = -\frac{2\gamma}{\beta_2}P_{pump} + \left[\Delta\omega_Z^{(N)}\right]^2 \quad . \tag{3.11}$$

This equation shows that $[\Delta\omega_P^{(N)}]^2$ also becomes a linear function of P_{pump}, and γ can be evaluated by the slope of the $[\Delta\omega_P^{(N)}]^2$ versus P_{pump} graph, as

$$\gamma = -\frac{\beta_2}{2}\frac{\partial\left[\Delta\omega_P^{(N)}\right]^2}{\partial P_{pump}}, \tag{3.12}$$

3.3 Experimental demonstration

3.3.1 Experimental setup

We conducted experiments to demonstrate the proposed PM-FWM method. The measurement setup is schematically shown in Fig. 3.2. CW tunable lasers were used for pump and probe lights at wavelengths of around 1550 nm. The pump light was amplified by an EDFA to a sufficient power level for the measurement. From Eqs. (3.6) and (3.12), the nonlinear coefficient is evaluated from the slope of linear function of $\omega_P^{(N)}$-P_{pump} and $(\Delta\omega_P^{(N)})^2$-P_{pump} for low and high β_2 fibers, respectively.

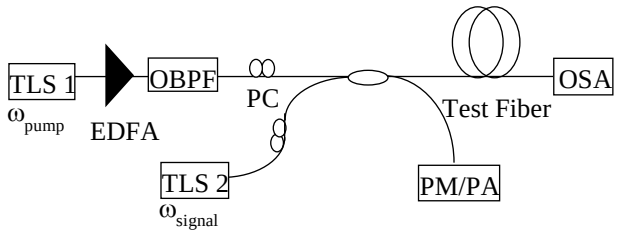

TLS: Tunable Laser Source
EDFA: Erbium Doped Fiber Amplifier
OBPF: Optical Band Pass Filter
PC: Polarization Controller
PM-3dB-OC : Polarization Maintaining 3dB Optical Coupler
OSA: Optical Spectrum Analyzer
PM: Power Meter
PA: Polarization Analyzer

Fig. 3.2 Measurement setup of PM-FWM method

The error Er_γ in measuring the nonlinear coefficient γ by this method comes from the ambiguity in identifying the pump frequency $\Delta\omega_p^{(N)}$ and the pump power ΔP_{pump} that provide the minimal idler power and the chromatic dispersion, which is expressed as

$$Er_{\gamma} \propto \frac{\partial\left(\omega_{\mathrm{P}}^{(\mathrm{N})} + Er_{\omega}\right)}{\partial\left(P_{\mathrm{pump}} + Er_{\mathrm{P}}\right)} - \frac{\partial\left(\omega_{\mathrm{P}}^{(\mathrm{N})}\right)}{\partial\left(P_{\mathrm{pump}}\right)} \quad , \tag{3.13}$$

where Er_{ω} and Er_{P} are the measurement errors of the pump frequency and power, respectively. The above equation indicates that the condition of $\Delta\omega_{\mathrm{p}}^{(\mathrm{N})} >> Er_{\omega}$, $\Delta P_{\mathrm{pump}} >> Er_{\mathrm{P}}$ should be satisfied in order to achieve high precision nonlinear coefficient γ measurement as shown in Fig. 3.3. To satisfy the condition, a high power EDFA was employed in the measurement.

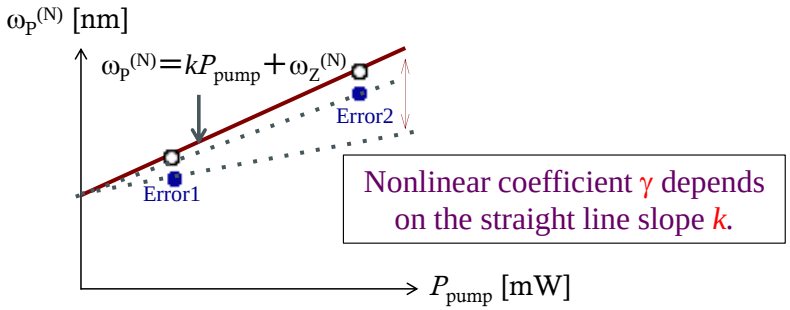

Fig. 3.3 Evaluation of a measurement error in $\omega_{\mathrm{p}}^{(\mathrm{N})}$ versus P_{pump} graph.

The polarization states of pump and probe lights were adjusted to be identical by polarization controllers (PC). In our measurement setup, we confirmed the co-polarized states of the pump and probe lights by a power meter (PM) to maximize the optical power after a polarization-maintained (PM)-3dB-optical coupler (OC) that had a function of eliminating one linear polarization. The pump and probe lights were then launched together into a tested fiber via the PM-3dB-OC. In this measurement setup, the generated idler output power was measured with an optical spectrum analyzer (OSA). In order to accurately evaluate the nonlinear coefficient γ, the absolute power of respective lightwaves are required. We used an OSA to measure the power, which was carefully calibrated with an optical power meter. The input and output polarization states of the probe and pump lights were monitored with a polarization analyzer (PA) at the fiber output, and we confirmed that the states of polarization were very stable even after propagation through 1km-long HNLDSF and SSMF.

In our measurement, ASE noise generated from the high power EDFA accompanied with the idler light at the fiber output. Fig. 3.4(a) shows the experimental results of the measured idler power after a 145m-long HNLDSF when $\Delta\omega = 15.3\times10^{12}$ rad/s. We found that the ultra-low power idler light submerged to the ASE noise at some wavelengths. In our measurement, the generated ASE noise was removed with a 4nm-bandwidth OBPF following the EDFA for accurately identifying the pump and signal frequencies that minimize idler power. Fig. 3.4(b) is an illustraties of the output

spectrum of a test fiber with and without 4nm-width OBPF employed.

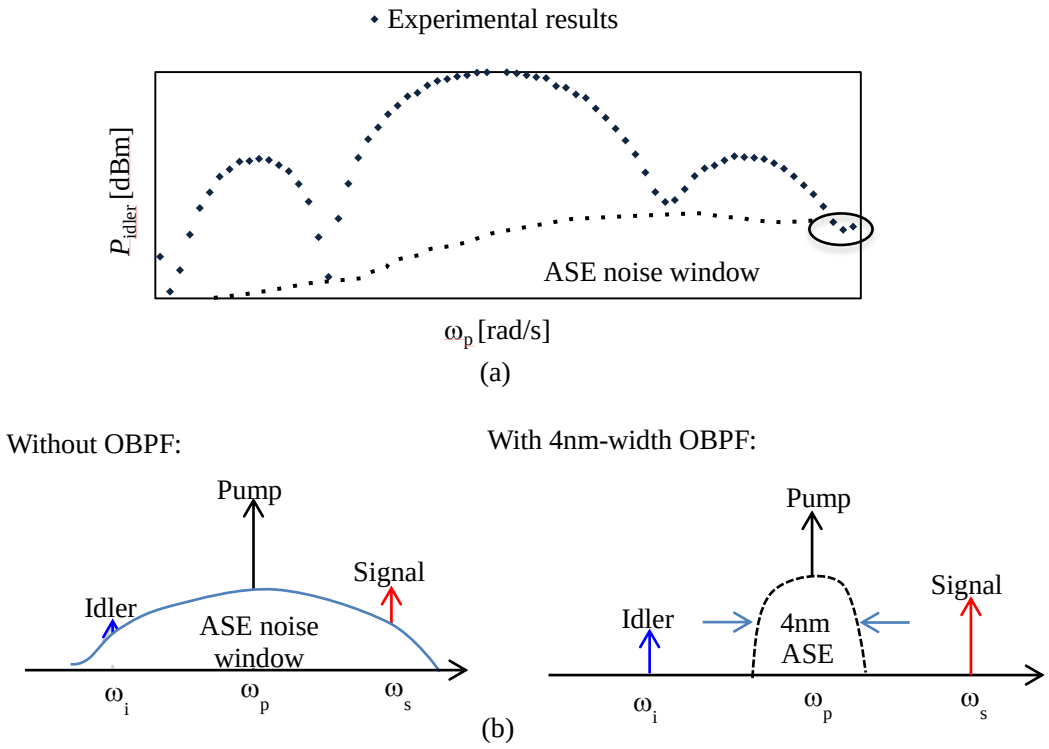

Fig. 3.4 Fiber output spectrum.

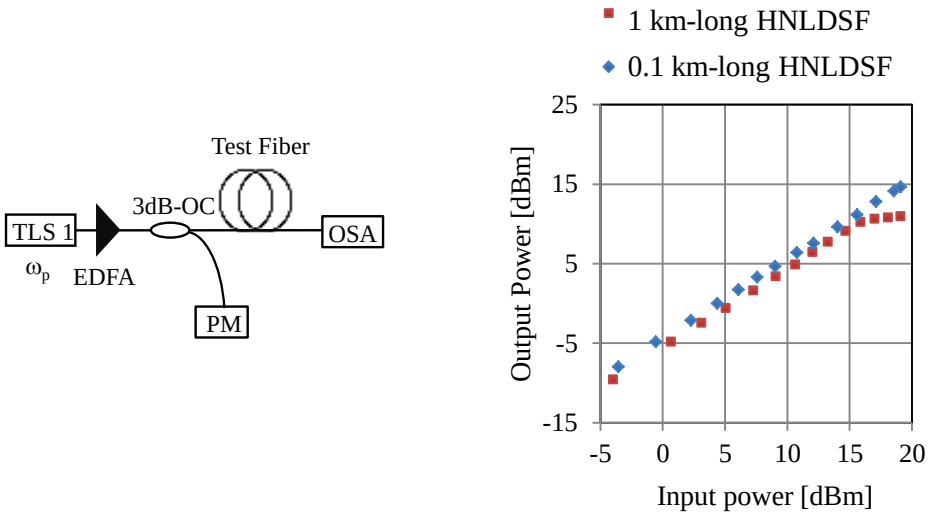

Fig. 3.5 Stimulated Brillouin Scattering (SBS) measurement

The stimulated Brillouin scattering (SBS) easily occurs in single-mode fiber for high input power. In our measurement setup, the pump power P_{pump} was measured by the OSA at the tested fiber output, taking splice and fiber losses into account. The pump power should be lower than the

threshold power of SBS effects occurring, since SBS would distort the linearity in $\omega_P^{(N)}$-P_{pump} and $(\Delta\omega_P^{(N)})^2$-P_{pump} required for measuring the nonlinear coefficient γ. The threshold pump power was evaluated as shown in Fig. 3.5, where the input-output characteristic was measured for the 1-km and 0.1-km long HNLDSFs with the setup also shown in the figure.

3.3.2 Experimental results

First, we examined a 1km-long HNLDSF with a low β_2. The frequencies of the pump and probe lights were scanned together with a constant difference of $\Delta\omega = 7.8\times10^{12}$ rad/s. Examples of the generated idler power P_{idler} against the pump frequency are shown in Fig. 3.1(a). The periodical minima is observed, and we confirmed that $\omega_P^{(N)}$ was shifted as the pump power increased from 1.6 to 26 mW, which is theoretically predicted in Fig. 3.6(a). The measured $\omega_P^{(N)}$ as a function of P_{pump} is shown in Figs. 3.6(b) and 3.6(c), satisfying the condition of Eq. (3.2) with N = 1 for Fig. 3.6(b) and N =2 for Fig. 3.6(c). Those values correspond to wavelengths of around 1535 nm and 1539 nm, respectively. In accordance with Eq. (3.5), $\omega_P^{(N)}$ is linearly decreasing with the increment of P_{pump}.

As mentioned in Eq. (3.6), β_3 should be known in advance in order to obtain the nonlinear coefficient γ. $\beta_{2Z}^{(N)}$ can be calculated from Eq. (3.3), and $\omega_Z^{(N)}$ can be determined from the y-intercept of $\omega_P^{(N)}$-P_{pump} graphs in Figs. 3.6(b) and 3.6(c), as described with Eq. (3.5). We drew a β_2 spectrum by determining the $\beta_{2Z}^{(N)}$ at several $\omega_Z^{(N)}$ related to respective N in Eq. (3.3), and β_3 was calculated as +0.034 ps^3/km by the biquadratic approximation of the β_2 spectra. Then, we obtained the slopes of $\omega_P^{(N)}$-P_{pump} graph in Figs. 3.6(b) and 3.6(c) by means of least squares approximation. Finally, γ at wavelenths of 1535 nm and 1539 nm were calculated as 17.2 and 17.3/W/km, respectively. These values correspond to a nonlinear index n_2 of 3.6×10^{-20} m^2/W for A_{eff} of 8.5 μm^2.

In order to know the effect of the length, we also examined a 0.14-km-long HNLDSF acquired from the same spool. The measured $\omega_P^{(N)}$ for N=-1 at wavelengths of around 1558 nm is shown in Fig. 3.6(d), where $\Delta\omega$ was fixed at 15.3×10^{12} rad/s. From Fig. 3.6(d), γ was evaluated to be 19 /W/km, which is closely corresponded to the value of the 1km-long HNLDSF.

Next, in order to verify if the PM-FWM method can be applied to a low nonlinearity (less than one-tenth of that in HNLDSF) and high β_2 (about -22 ps^2/km or chromatic dispersion of about +17 ps/nm/km) fiber, γ of a 1km-long SSMF was measured using Eqs. (3.9) and (3.12). The probe frequency was scanned while pump frequency was kept at 1.2×10^{15} rad/s (wavelength of 1550 nm). Fig. 3.7(a) shows measured P_{idler} as a function of $(\Delta\omega)^2$, where a periodic change of the generated idler power P_{idler} against the squared frequency difference $(\Delta\omega)^2$ is observed. β_2 at ω_{pump} was determined from Eq. (3.9) as -21.4 ps^2/km. Measured $\Delta\omega_P^{(N)}$ against P_{pump} is shown in Fig. 3.7 (b) for N = -1. We successfully determined the nonlinear coefficient γ and n_2 as 1.3 /W/km and 2.7×10^{-20}

m^2/W, respectively. In addition, the chromatic dispersion was also measured as 16.5 ps/nm/km at a wavelength of 1550 nm.

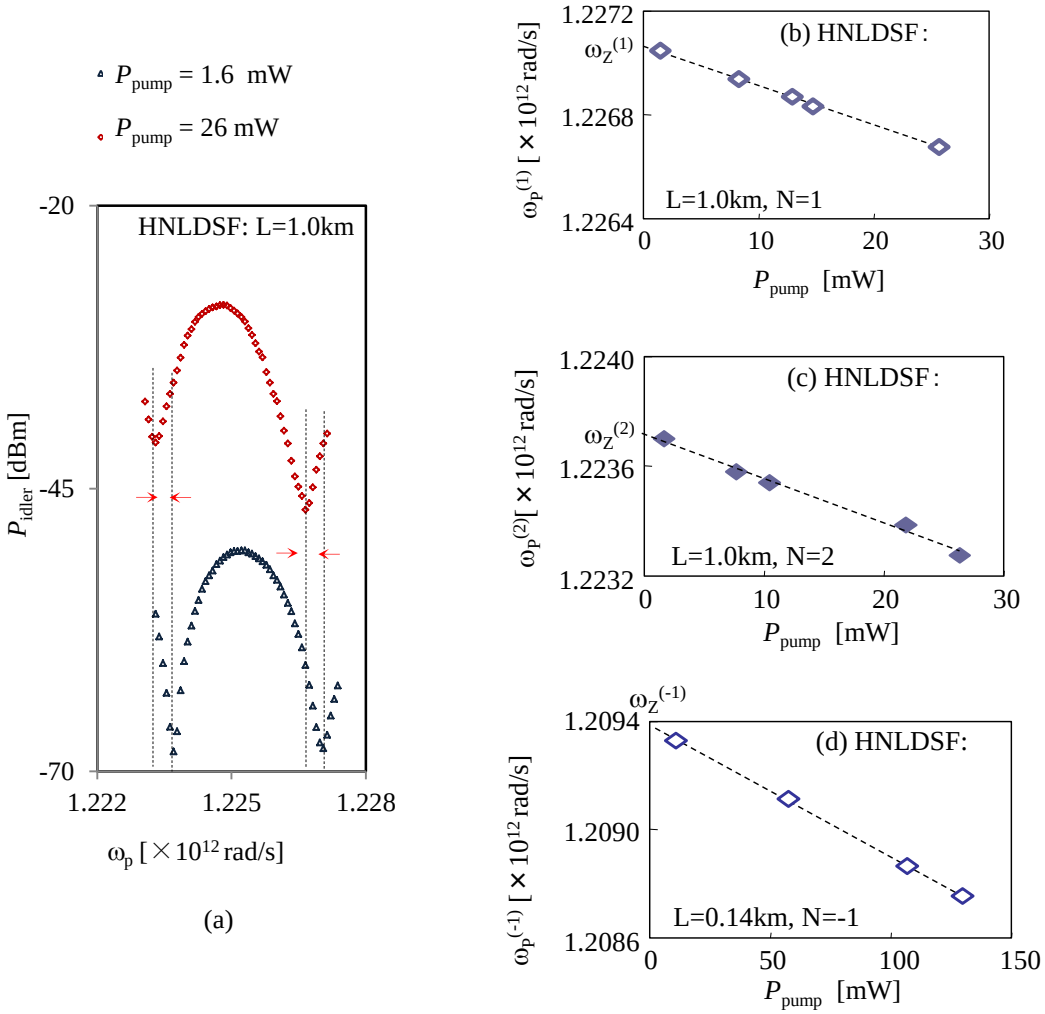

Fig. 3.6 Experimental results for HNLDSFs. (a): Examples of generated idler power P_{idler} against pump frequency with $\Delta\omega = 7.8\times10^{12}$ rad/s for 1km-long HNLDSF. (b)-(d): Pump frequency providing the minimal idler power against pump power with (b) N=1 and (c) N=2 for 1.0 km-long HNLDSF, and (d) N=-1 for 0.14km-long HNLDSF with $\Delta\omega$=15.3×1012 rad/s.

Finally, we compared the nonlinear coefficient γ and n_2 measured with the PM-FWM method to the ones with CW-SPM method [72], in which a factor of 8/9 was taken into account in the evaluation for the random input polarization states. It is noted that γ of SSMF was measured with a 0.40-km-long short fiber not to suffer from the CD effect in the CW-SPM method. The measurement results are summarized in Table 3.2. We found that the PM-FWM method gives results well consistent with those by the CW-SPM method. The CD and dipersion slope measured with

PM-FWM method are also shown in Table 3.2, and agree well with the results obtained by the modulation phase shift (MPS) method [74]. The two methods agree well with each other.

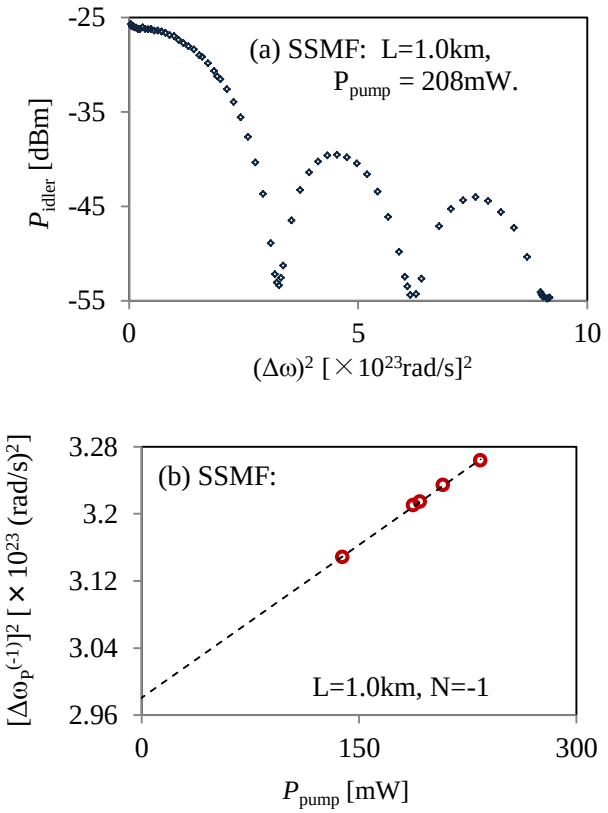

Fig. 3.7 Experimental results for 1km-long SSMF. (a) The generated idler power P_{idler} against squared frequency difference. (b) Squared frequency difference $[\Delta\omega_P^{(N)}]^2$ providing the minimal idler power against pump power P_{pump} with N= -1.

Table 3.2 Measured results of n_2

Measured Fibers		HNLDSF		SMF
Wavelength [nm]		1535	1558	1550
Length [km]		1.0	0.14	1.0
A_{eff} [μm^2]		8.5	8.5	84.5
Dispersion [ps/nm/km]	PM-FWM	-0.17	0.155	16.8
	MPS	-0.153	0.146	16.7
Dispersion Slope [ps/nm^2/km]	PM-FWM	0.019	0.02	0.058
	MPS	0.021	0.02	0.058
n_2 [$\times 10^{-20} m^2/W$]	PM-FWM	3.6	4.0	2.71
	CW-SPM	3.8	4.2	2.66 (0.40km)

3.4 Conclusion

A novel fiber nonlinear coefficient γ measuring method employing PM-FWM has been proposed. With a simple setup, determination of the nonlinear coefficient γ for 0.1- to 1-km long HNLDSF and 1km-long low-nonlinearity SSMF has been achieved in a straightforward way. The measured results agreed well with the ones obtained by the CW-SPM method. The CD and dispersion slope can be simultaneously measured with high precision, and therefore their influence to the nonlinear coefficient γ measurement can be removed.

Chapter 4

All-optical OOK to 16QAM format conversion

In this chapter, in order to well understand the XPM employed in amplitude-to-phase modulation format conversion mentioned in Chapter 2, an RZ-OOK to RZ-BPSK format conversion scheme will be described in Section 4.2. Then, all-optical OOK to 16QAM format conversion will be proposed and numerically demonstrated at 10 Gb/s from Section 4.3. A 16QAM signal is generated as a result of super-position of two QPSK signals with different amplitudes. In the converter, the nonlinear effects of XPM and OPA are employed for OOK to QPSK format conversion and achieving 2:1 amplitude ratio between two QPSK signals, respectively. The performance of the OOK to 16QAM format converter will be numerically evaluated.

4.1 Introduction

All-optical signal processing techniques have received much attention owing to their ultra-fast response time and capability of extending network transparency by eliminating optical-electrical-optical conversions in transmission nodes. Nowadays, multi-level modulation formats are extensively studied, and various types of multi-level modulation formats have been introduced in long-haul transmission systems for WANs in order to upgrade the commercial 10/40G transmission capacity to 100G and later 400G. However, conventional RZ-OOK and NRZ-OOK formats may keep their main role in MANs and access network or rarely incorporate with the multi-level modulation format in the WANs. In the future, different networks may employ different modulation formats suited to the network's coverage. The function of all-optical RZ/NRZ-OOK to multi-level

modulation format conversion will be an important interface technology in such optical networks.

BPSK signaling has been attracting increasing attention for its 3-dB optical signal-to-noise ratio (OSNR) advantage over conventional amplitude shift keying (ASK) signaling, as well as its high tolerance to transmission impairments such as CD and PMD in long-haul back-bone. Recently, all-optical modulation format conversion from NRZ-OOK to RZ-BPSK based on the nonlinearity of either fiber or SOA has been proposed [41, 42]. In particular, we had known that RZ-OOK enjoys an -1, -2 dB advantage over NRZ-OOK in ASE noise limited systems due to an inherent tolerance of the RZ-OOK pulse shape to ISI [22]. In this thesis, we investigated RZ-OOK to RZ-BPSK modulation format conversion based on fiber nonlinearity. By employing a low-dispersion HNLF and choosing the optimal wavelengths for the probe and the control pulses, the effects of walk-off and parametric gain can be suppressed. We experimentally demonstrate an error-free operation of the format conversion at a bit rate of 10.7 Gb/s. In addition, we investigated the CD and timing tolerance of the converter.

Among multi-level modulation formats, 16QAM, which carries four bits per symbol, is attractive owning to its outstanding performance in terms of the transmission capacity. In this chapter, the scheme of a novel all-optical OOK to 16QAM modulation format conversion employing NOLM based on XPM and OPA in optical fibers will be described and numerically demonstrated. A 16QAM signal is generated as a superposition of two QPSK signals with different amplitudes. OOK to QPSK modulation format conversion is achieved by XPM in a HNLF. The amplitude ratio 2:1 of two QPSK signals can be accomplished by an OPA in another HNLF, in which the phase-matching condition cannot be satisfied between lights propagating in the opposite directions. In our scheme, a Sagnac interferometer is employed instead of a conventional all-fiber MZI where the phase drift between two branches is hard to control.

4.2 All-optical OOK to BPSK format conversion by employing XPM

Fig. 4.1 illustrates the operation principle. A RZ pulse sequence and a RZ-OOK signal are synchronously launched into a HNLF as probe and control pulses, respectively. The phase of each probe pulse is optically modulated due to XPM induced by the overlapped control pulse, where the phase change of the probe pulse is proportional to the peak power of the control pulses. By properly adjusting the peak power of the control pulse, the phase change of the probe pulse can be either “π” or “0” corresponding to the “1” or “0” level of the input RZ-OOK signal. Then, only the probe pulses are passed through an OBPF. In order to generate a uniform-amplitude BPSK signal, the effect of OPA in the HNLF should be suppressed. The walk-off arising from the difference in the

group velocity between the control and probe pulses with different wavelengths should also be considered because it will reduce the efficiency of XPM.

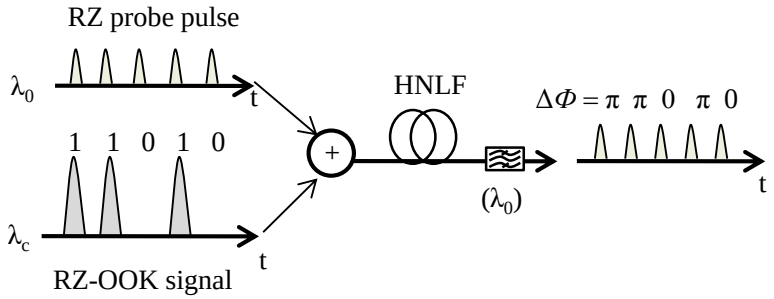

Fig. 4.1. Schematic diagram of the proposed modulation format conversion.

4.2.1 Experimental demonstration

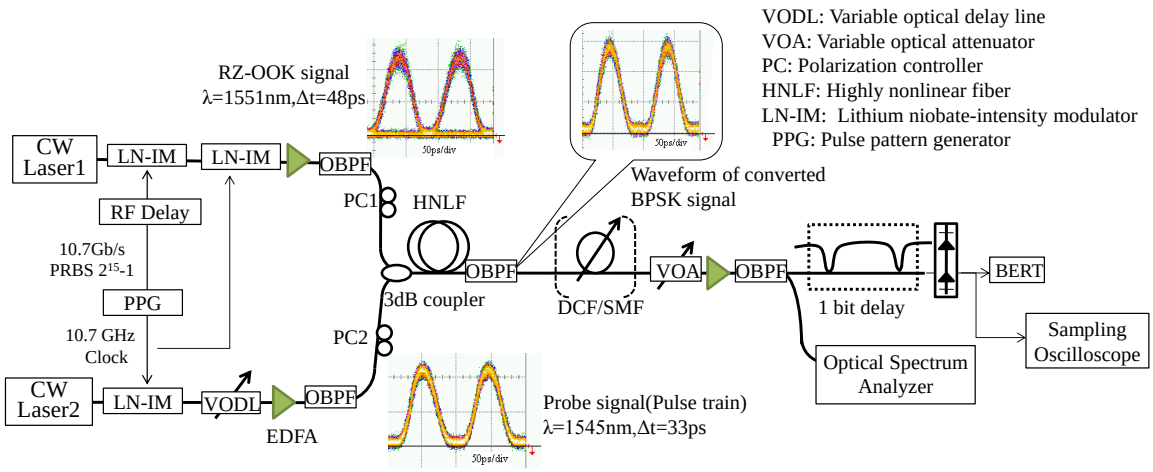

Fig. 4.2 Experimental setup.

The experimental setup is shown in Fig. 4.2. Two cascaded Z-Cut lithium niobate-intensity modulators (LN-IM) were used to modulate CW light into a differentially encoded RZ-OOK signal with 10.7Gb/s PRBS with a length of 2^{15}-1 from a pulse pattern generator (PPG), since we used one-bit delay balance detection to demodulate a converted BPSK signal. The probe pulse sequence was generated by modulating another CW light with one Z-Cut LN-IM by using a 10.7-GHz clock from the PPG. An RF delay was used to overlap the data and clock signals in HNLF. Considering the walk-off and OPA, the wavelengths of CW laser 1 and CW laser 2 were set at 1551nm and 1545nm, respectively. A variable optical delay line (VODL) is used to adjust the time delay between

the control and probe pulses. Here, we set the bias point of LN-IM for the probe pulse to induce a down-chirp, because the probe pulse was up-chirped in HNLF by the RZ-OOK signal. Two PCs were used to optimize the input polarization states of the control and probe pulses, respectively. The average powers of the control and probe signals launched onto the HNLF were 22 dBm and 1.6 dBm, respectively. The zero-dispersion wavelength, the dispersion slope, the fiber loss, the nonlinear coefficient, and the length of the HNLF were 1566.965 nm, 0.02089 ps/ nm^2/km, 0.426 dB/km, 12 /W/km, and 406 m, respectively.

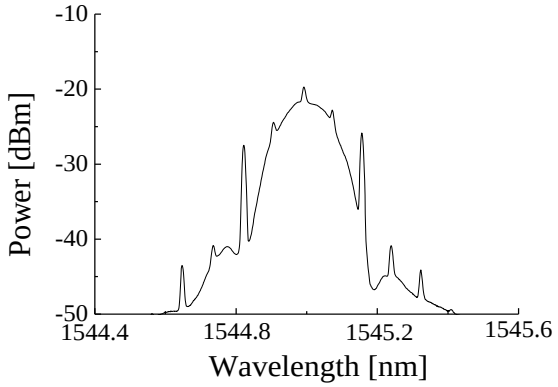

Fig. 4.3 Spectrum of converted signal before 1-bit delay interferometer.

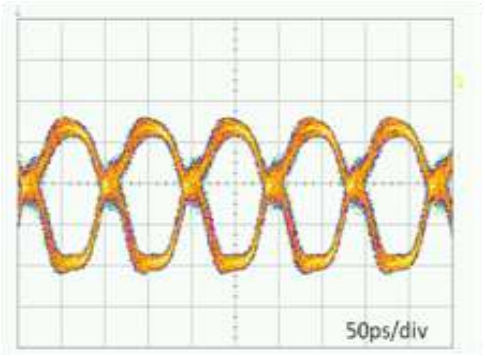

Fig. 4.4 Eye diagram of the converted signal after 1-bit delay and balance receiver.

We can observed a clear pulse train of the converted signal as shown in the inset of Fig. 4.2. Fig. 4.3 shows the spectrum of the 10.7 Gb/s converted BPSK signal before a one-bit delay interferometer. The carrier suppressed spectrum implies the generation of a PSK signal. However, the π phase modulation could not be perfectly achieved due to the unsuppressed SBS phenomenon [75]. Fig. 4.4 shows the eye diagram of the converted BPSK signal after a one-bit delay interferometer and a balance receiver. We can see a clear eye opening, which indicates that the phase

of the converted BPSK signal is properly modulated by "π" and "0", according to the RZ-OOK signal of "1" and "0", by XPM in the HNLF. We measured the bit error rate (BER) of the converted BPSK signal by changing the power of BPSK signal before the receiver using an optical variable attenuator (VOA) as shown in Fig. 4.5(a). An error free operation was achieved in this measurement.

4.2.2 Time and dispersion tolerance

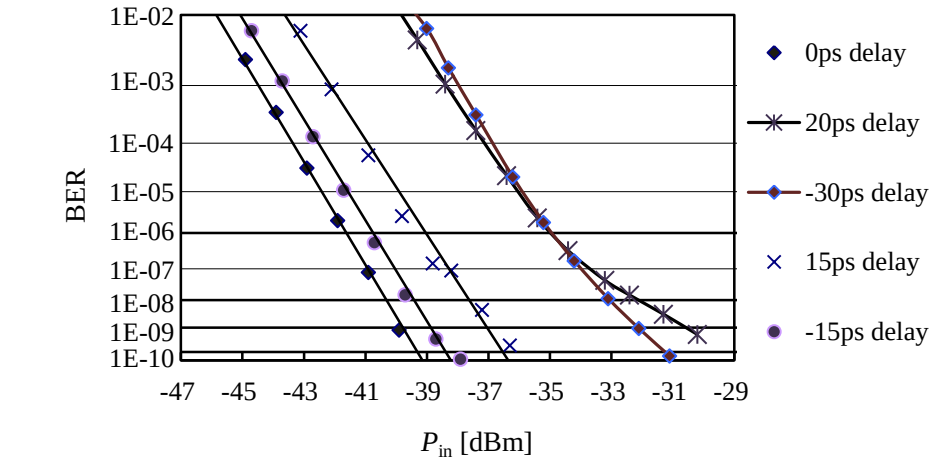

(a)

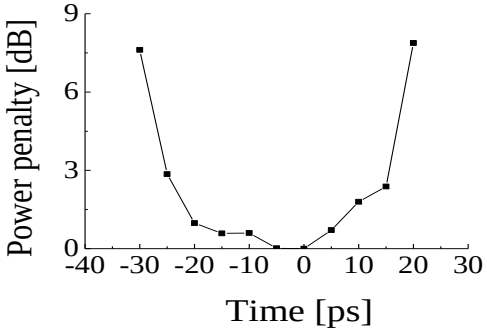

(b)

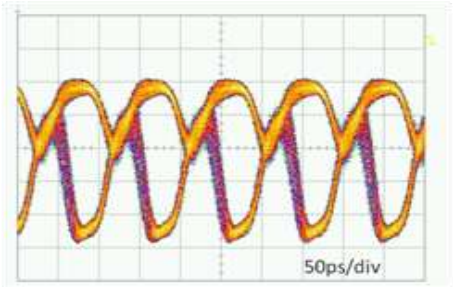

(c)

Fig. 4.5. Results of time-tolerance measurement. (a) BER for several time delays. (b) Power penalty at BER=10^{-9} as a function of time delay between control and probe pulses. (c) Eye diagram after one-bit delay and balance receiver for 20ps time delay between control and probe pulses..

The performance of this RZ-OOK to RZ-BPSK modulation format converter is affected by the time detuning between the control and probe pulses. We investigated the timing tolerance by measuring the eye diagrams and the power penalty at BER=10^{-9} with changing the time delay between the control and probe pulses controlled by VODL, as shown in Fig. 4.5. Fig. 4.5(a) shows

the BER in several different time delays, and Fig. 4.5(b) shows the measured power penalty as a function of the time delay between the control and probe pulses. Time detuned control and probe pulses results in an asymmetric spectrum in the converted BPSK since the time delay results in asymmetric phase modulation by XPM. In Fig. 4.5(a), an error floor was observed for a relatively large time delay. Fig. 4.5(c) shows an eye diagram after the one-bit delay and the balance receiver for a 20-ps time delay between the control and probe pulses. The asymmetric XPM phase shift can be observed, compared with the eye diagram shown in Fig. 4.4.

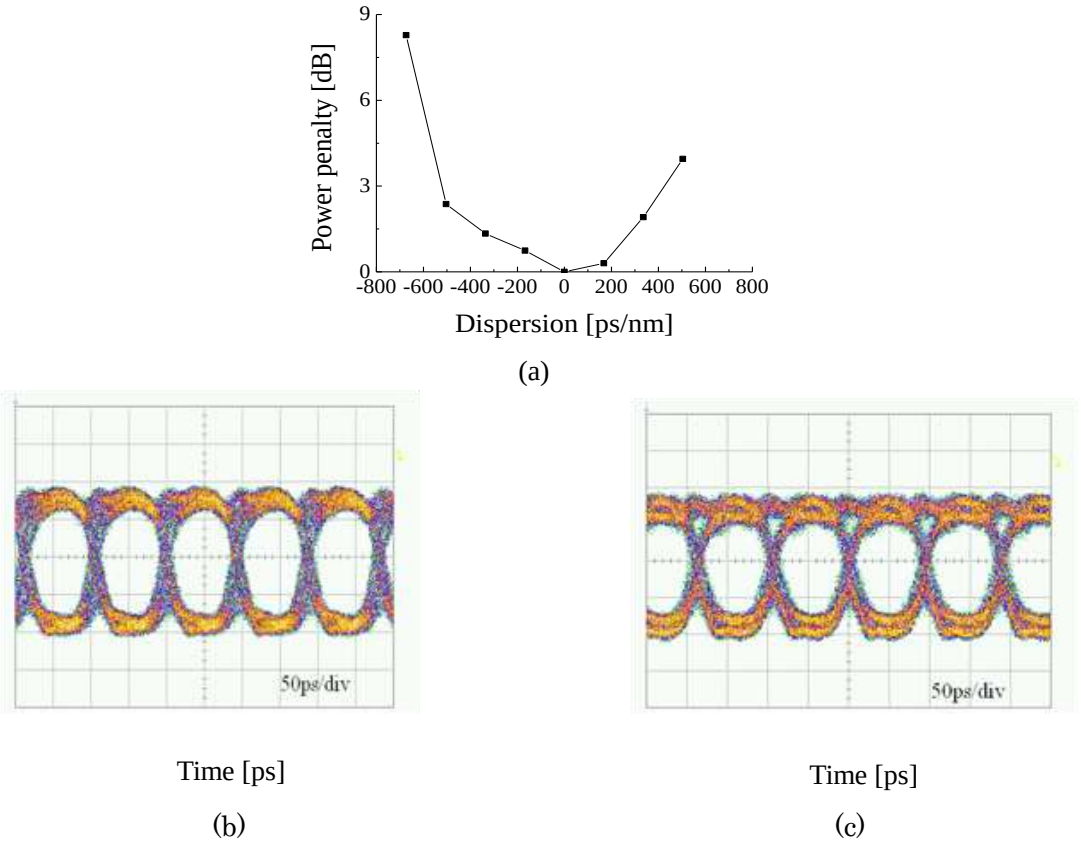

Fig. 4.6. Results of dispersion-tolerance measurement. (a) Power penalty as a function of the imposed dispersion. Eye diagrams of the received signal using DCF/SMF with dispersion. (b) -500.19ps/nm. (c) 503.85ps/nm.

The transmission capability of the converted BPSK signal was inspected by examining the dispersion tolerance. We measured the eye diagrams and the power penalty at BER=10^{-9} as a function of the imposed dispersion. Fig. 4.6(a) shows the results of the power penalty. A reasonable dispersion tolerance of ±300 ps/nm suitable for long-haul transmissions was observed. Figs. 4.6(b) and 4.6(c) show the eye diagrams of the received signal after transmitted through dispersion compensated fiber (DCF) with a dispersion of -500.19 ps/nm and SSMF with a dispersion of 503.85

ps/nm. The waveform shown in Fig. 4.6(c) is degraded from that shown in Fig. 4.6(b). This degradation was probably caused by the imbalance frequency chirp induced by the LN-IM and XPM. It implies that the results of dispersion tolerance can be improved further.

4.3 Principle of OOK to 16QAM format conversion based on NOLM

Fig. 4.7(a) shows the configuration of the proposed OOK to 16QAM modulation format converter whose main part is a NOLM including two HNLFs in it. We denote the four ports of the 3dB couplers as ports 1, 2, 3, and 4 as shown in Fig. 4.7(a). The 3dB coupler has a 1:1 power-split ratio and the phases of the coupled output signal and the through output signal are 90° shifted. Port 3 is the input port of this converter. The probe pulse E_{in} incident on the NOLM from the 3 dB coupler travels through the loop in both directions. We call these two probe pulses as clockwise and counter-clockwise probe pulses, respectively. The electrical fields of the two probe pulses are denoted as E_{c} and E_{cc} and come out from port 1 and port 2 of the 3dB coupler, respectively. The relation between the input electrical field and the output from port 1 and port 2 is expressed as

$$E_{\text{c}} = -jE_{\text{cc}} = \frac{1}{\sqrt{2}} E_{\text{in}}. \tag{4.1}$$

HNLF1 is employed for phase modulation as shown in Fig. 4.7(b). It works as an OOK to QPSK modulation format converter. The probe pulse and two OOK signals, as control pulses, are synchronously launched into HNLF1. The probe pulse is modulated in its phase due to XPM induced by the co-propagating control pulses. From Eq. (2.9), the phase changes of the probe pulses due to XPM are given by

$$\begin{aligned} \Phi_{\text{c}} &= 2\gamma L_{\text{eff}} \left(P_1 + P_2\right), \\ \Phi_{\text{cc}} &= 2\gamma L_{\text{eff}} \left(P_3 + P_4\right), \end{aligned} \tag{4.2}$$

where P_j (j=1, 2, 3, 4) are the peak powers of OOK-j. γ and L_{eff} are the nonlinear coefficient and the effective interaction length of HNLF1, respectively. L_{eff} depends on the fiber loss that is defined as

$$L_{\text{eff}} = \frac{1 - \exp(-\alpha L)}{\alpha}, \tag{4.3}$$

where α and L are the attenuation constant and the length of HNLF1, respectively. Eq. (4.2) shows that the phase change of the clockwise probe pulse Φ_c and the counter-clockwise probe pulse Φ_{cc}

are proportional to the sum of the peak powers of the two OOK signals acting as the control pulses. Thus, by properly adjusting the peak powers of the control pulses, Φ_c and Φ_{cc} can be set to 0, π/2, π, or 3π/2. Namely, an OOK to QPSK modulation format conversion is bilaterally realized in HNLF1.

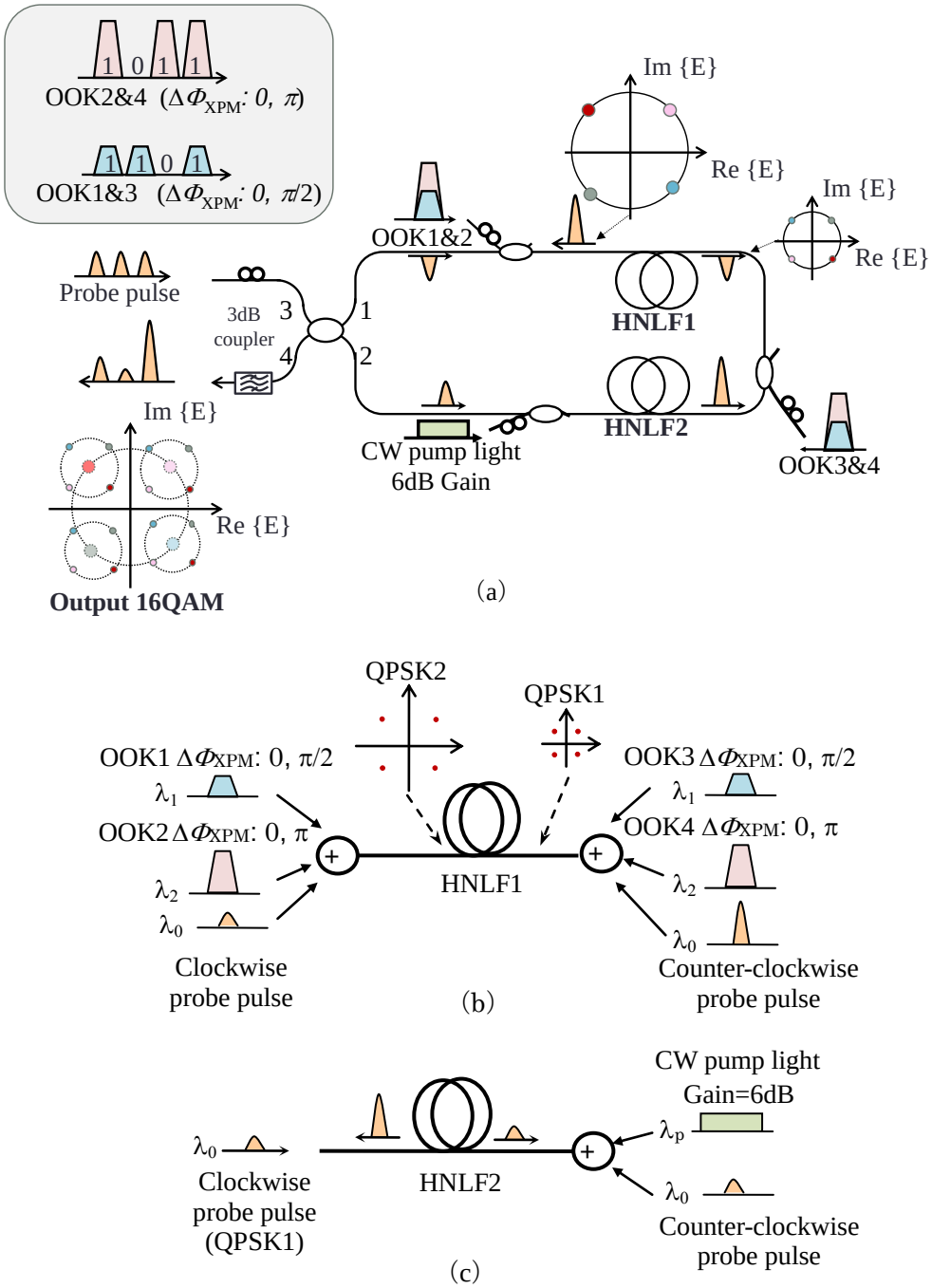

Fig. 4.7. Schematic diagram of the proposed modulation format converter. (a) The configuration of the converter. (b) Schematic diagram of phase modulation in HNLF1. (c) Schematic diagram of amplitude modulation in HNLF2.

Based on this consideration, we expect the control pulses of OOK 1 and OOK 2 signals to induce π/2 and π phase changes onto the clockwise probe pulse, respectively. The other two control pulses, OOK 3 and OOK4, induce the same amount phase changes to the counter-clockwise probe pulse. From Eq. (4.2), the desired peak powers of the four OOK signals P_j are given by

$$2P_1 = P_2 = 2P_3 = P_4 = \frac{\pi}{2\gamma L_{\text{eff}}}. \tag{4.4}$$

The clockwise and counter-clockwise probe pulses also receive a phase shift from the counter-propagating OOK signals due to XPM. The phase shift Φ_{cp} is given by the average powers of the control pulses as

$$\begin{aligned} \Phi_{\text{c\_cp}} &= 2\gamma L_{\text{eff}} \left(\bar{P}_3 + \bar{P}_4\right), \\ \Phi_{\text{cc\_cp}} &= 2\gamma L_{\text{eff}} \left(\bar{P}_1 + \bar{P}_2\right), \end{aligned} \tag{4.5}$$

where $\bar{P}_j$ (j=1, 2, 3, 4) are the average powers of the OOK signals. $\Phi_{\text{c\_cp}}$ and $\Phi_{\text{cc\_cp}}$ are the phase changes of the clockwise and counter-clockwise probe pulses, respectively, induced by counter-propagating OOK signals. From Eq. (4.4), for long trains of random input signals, the relation between the average powers of the four OOK signals are given by

$$2\bar{P}_1 = \bar{P}_2 = 2\bar{P}_3 = \bar{P}_4 . \tag{4.6}$$

The clockwise and the counter-clockwise probe pulses obtain the same phase shift from the counter-propagating OOK signals via XPM as

$$\Phi_{\text{cp}} = \Phi_{\text{c\_cp}} = \Phi_{\text{cc\_cp}}. \tag{4.7}$$

The probe pulse itself also experiences SPM, which is expressed as

$$\begin{aligned} \Phi_{\text{c\_SPM}} &= \gamma L_{\text{eff}} P_{\text{c}}, \\ \Phi_{\text{cc\_SPM}} &= \gamma L_{\text{eff}} P_{\text{cc}}, \end{aligned} \tag{4.8}$$

where $\Phi_{\text{c\_SPM}}$ and $\Phi_{\text{cc\_SPM}}$ are the phase changes of the clockwise and counter-clockwise probe pulses induced by SPM. The OPA was employed to induce 6-dB gain to the counter-clockwise probe pulse, then the peak powers of the clockwise P_{c} and counter-clockwise P_{cc} probes pulses should satisfy the following relation,

$$P_{\text{cc}} = 4P_{\text{c}}. \tag{4.9}$$

In a general situation, we can set $P_{cc} \le 0$dBm, thus neither Φ_{c_SPM} or Φ_{cc_SPM} is small enough to be ignored.

QPSK1 and QPSK2 are generated after the clockwise and counter-clockwise probe pulses experience a 4-level phase change in HNLF1. The electric fields of the clockwise probe pulse and counter-clockwise probe pulses after passing through HNLF1 are expressed as

$$E_c = \frac{1}{\sqrt{2}} E_{in} \exp\left[j\left(\Phi_c + \Phi_{cp}\right)\right], \qquad E_{cc} = \frac{j}{\sqrt{2}} E_{in} \exp\left[j\left(\Phi_{cc} + \Phi_{cp}\right)\right]. \tag{4.10}$$

In order to generate 16QAM signal from the above two QPSK signals, the amplitude of QPSK2 should be doubled relative to that of QPSK1. A 2:1 amplitude ratio is accomplished in HNLF2 via OPA as shown in Fig. 4.7(c). CW pump light and the probe pulses are transmitted together in HNLF2, and OPA occurs effectively by properly allocating the wavelengths of the probe and CW lights. The launched power of the CW light is adjusted to induce a 6-dB OPA onto the counter-clockwise probe pulse. The CW light induce the same phase shift Φ_{cw} by XPM to both the clockwise and counter-clockwise probe pulses, while inducing OPA only to the counter-clockwise probe pulse in HNLF 2, since that phase matching cannot be achieved between anti-directionally propagating pulses.

OBPFs are used to remove the OOK signals and the CW pump light at the output of the NOLM. The one- round transmitted electric fields of the probe pulses at port 1 and port 2 of the 3dB coupler are expressed as

$$E_1 = 2E_{cc} \exp\left(j\Phi_{cw}\right) = j\sqrt{2} E_{in} \exp\left[j\left(\Phi_{cc} + \Phi_{cp} + \Phi_{cw}\right)\right], \qquad E_2 = E_c \exp\left(j\Phi_{cw}\right) = \frac{1}{\sqrt{2}} E_{in} \exp\left[j\left(\Phi_{cc} + \Phi_{cp} + \Phi_{cw}\right)\right]. \tag{4.11}$$

At the output of the converter, i.e., port 4, the electrical field of the probe pulse is then given by

$$E_{out} = \frac{1}{\sqrt{2}}\left(jE_1 + E_2\right) = \frac{1}{2} E_{in} \exp\left[j\left(\Phi_{cp} + \Phi_{cw}\right)\right]\left[\exp\left(j\Phi_c\right) - 2\exp\left(j\Phi_{cc}\right)\right]. \tag{4.12}$$

Eq. (4.12) shows that the output signal of this converter is a superposition of the two QPSK signals. The amplitude of one QPSK signal is two times the other. In Eq. (4.12), E_{in}, Φ_{cp} and Φ_{cw} are constant, thus

$$E_{\text{out}} \propto \exp\left(j\frac{\pi}{4}\right)\left[\exp\left(j\Phi_{\text{c}}\right)-2\exp\left(j\Phi_{\text{cc}}\right)\right]$$
$$\propto\left[\sin\left(\Phi_{\text{c}}+\frac{\pi}{4}\right)-2\sin\left(\Phi_{\text{cc}}+\frac{\pi}{4}\right)\right]+j\left[\cos\left(\Phi_{\text{c}}+\frac{\pi}{4}\right)-2\cos\left(\Phi_{\text{cc}}+\frac{\pi}{4}\right)\right] \tag{4.13}$$

In Eq. (4.13), we assumed that the phase difference relative to the reference is π/4, both Φ_c and Φ_{cc} at the HNLF output take one of the four values, 0, π/2, π, and 3π/2, depending on the "0" or "1" data of the four OOK channels. Each symbol of E_{out} carries 4 data bits, and the I-Q constellation map by sampling each symbol peak have 16 levels as shown in Fig. 1.2. Therefore, OOK to 16QAM format conversion can be realized by the proposed scheme.

4.4 Simulation

In the previous section, we neglected FWM and the walk-off between the control and probe pulses. They can induce a power fluctuation and imperfect phase modulation to the probe pulse. Therefore, the parameters of HNLF and the wavelengths and peak powers of control and probe pulses should be carefully designed. We calculate the waveform and the I-Q diagram of the converted 16QAM signal at the output of NOLM at a symbol rate of 10 GS/s by using the split-step Fourier method including the 3rd-order dispersion of HNLF. The simulation model is shown in Fig. 4.8. To simplify the simulation, we separated the clockwise and counter-clockwise paths by assuming a MZI model. Φ_{cw} is the calculated constant phase shift of the clockwise probe pulses due to XPM induced by the counter propagating CW light.

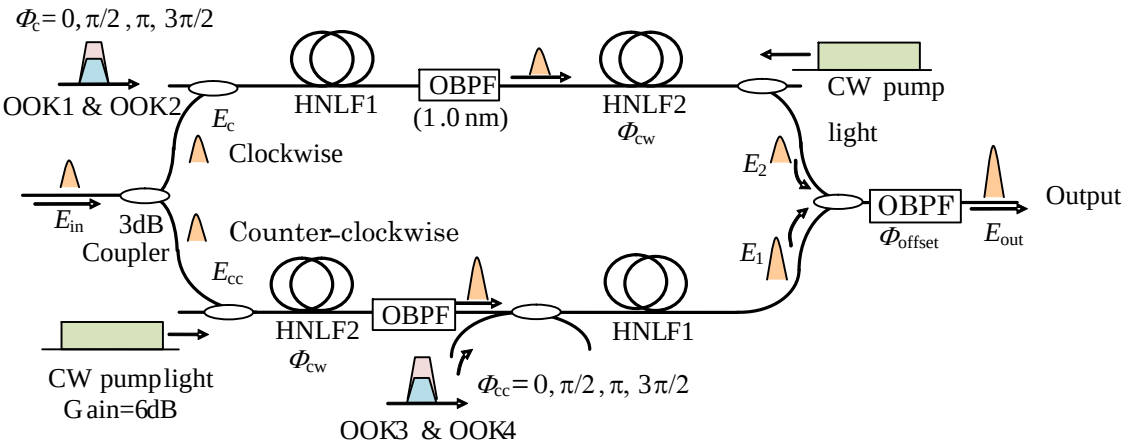

Fig. 4.8. Simulation model of the proposed modulation format converter.

The phase is given by

$$\Phi_{\mathrm{cw}} = 2\gamma_2 L_{\mathrm{eff},2} P_{\mathrm{cw}}, \tag{4.14}$$

where γ_2 and $L_{\mathrm{eff},2}$ are the nonlinear coefficient and the effective interaction length of HNLF 2, respectively. P_{cw} is the power of the CW light. The parameters of HNLF1 and HNLF 2 are shown in Table 4.1. Here, we have added a phase offset $\Phi_{\mathrm{offset}} = \pi/4 - (\Phi_{\mathrm{cp}} + \Phi_{\mathrm{cw}})$ to the output signal of this converter. The output electrical field E_{out} can be written as

$$E_{\mathrm{out}} = \frac{1}{2} E_{\mathrm{in}} \exp\left(j\frac{\pi}{4}\right)\left[\exp(j\Phi_{\mathrm{c}}) - 2\exp(j\Phi_{\mathrm{cc}})\right]. \tag{4.15}$$

The pulse shapes of the control and the probe pulses were assumed to be a super-Gaussian and a Gaussian, respectively. Their waveforms can be expressed as

$$E(t) = \sqrt{P}\exp\left(\frac{t}{T_0}\right)^{2m}, \qquad T_{\mathrm{FWHM}} = 1.665T_0, \tag{4.16}$$

where parameter *m* determines the degree of the edge sharpness. T_{FWHM} is the full width at half maximum (FWHM) of the pulses.

Table 4.1. Parameters of HNLF1 and HNLF2 at a wavelength of 1570nm.

	HNLF1	HNLF2
Dispersion [ps/nm/km]	0.08343	0.04646
Dispersion slope [ps/nm^2 /km]	0.02035	0.02047
Loss [dB/km]	0.426	0.411
Nonlinearity [1/W/km]	12.0	12.0
Length [km]	0.406	0.403

Table 4.2. Wavelengths and peak powers of control, probe pulses, and CW light.

	λ [nm]	*P* [dBm]	*m*	T_{FWHM} [ps]
OOK1,OOK3	1551.2	22.6	3	60
OOK2,OOK4	1536.5	25.4		
Probe pulse	1545.0	0.0	1	30
CW pump light	1569.5	24.5		

The wavelengths, the peak powers, the pulse width and parameter *m* of the control pulses of OOK1-4, which are used to induce π/2 or π phase shift to probe pulses by XPM, and those of the probe pulses and the CW pump light used to induce 6-dB parametric gain to the counter-clockwise probe pulses are summarized in Table 4.2. These parameters were designed for our simulation. There is an almost a 3dB power difference between the peak powers of OOK1 (OOK3) and OOK2

(OOK4), even though they are a bit larger than the theoretical value given by Eq. (4.4), since waveform deformation due to dispersion is not included in the theoretical estimation. Here, we ignore the losses of the OBPFs and couplers for coupling the OOK signals, the CW pump light, and the probe pulses.

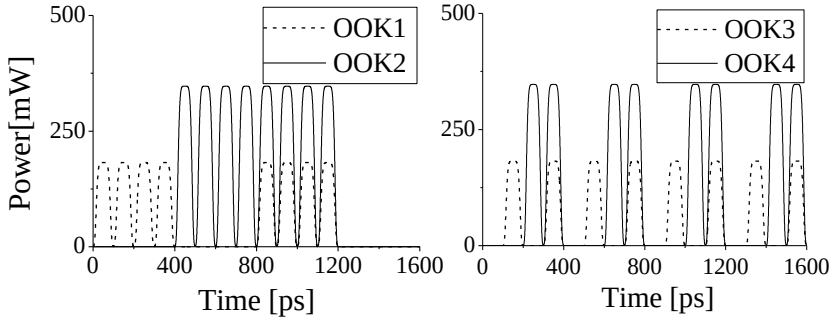

(a)

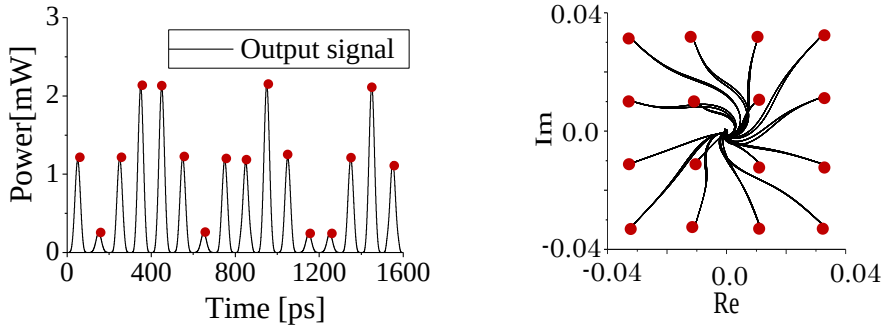

(b)

Fig. 4.9. Waveforms. (a) Waveforms of four input OOK signals. (b) Intensity waveform and I-Q diagram at the output of the converter at 10 GS/s.

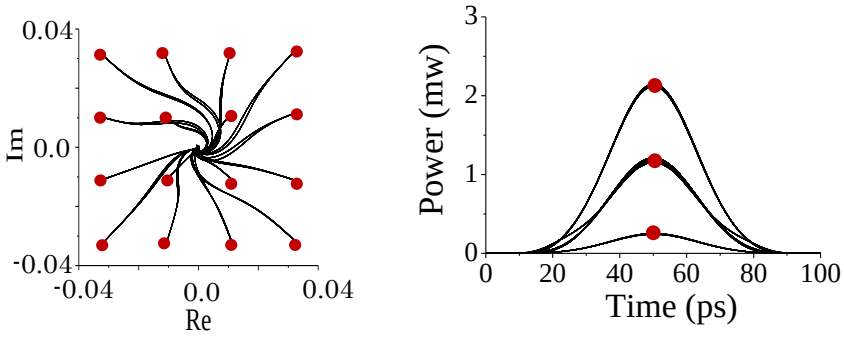

Fig. 4.10. I-Q diagram and intensity eye diagram of the output 16QAM signal when the four input OOK signals are 10 Gb/s PRBSs of length 2^7-1.

The simulation results are shown in Fig. 4.9. Fig. 4.9(a) shows the waveforms of four OOK signals, where all possible patterns of 2^4=16 symbols are taken into account. Fig. 4.8(b) shows intensity waveform and the I-Q diagram at the output of the converter. In the I-Q diagram, the red circles indicate the sampling point of each pulses's peak, and the lines connecting the center point and red circles indicate each pulses' sidelobe between the bottom and peak. A clear three-level pulse train can be observed. Due to FWM between OOK signals and the probe pulse, small fluctuations are observed at the output pulse's peaks.

Fig. 4.10 depicts the I-Q diagram and the intensity eye diagram of the output 16QAM signals when the four OOK signals are modulated at a 10-Gb/s pseudo-random binary sequence (PRBS) with a length of 2^7-1. We can observe a clear eye opening. Even when the pattern length of the input signal is long, the I-Q diagram hardly changes from Fig. 4.9(b). These simulation results confirm that OOK to 16QAM modulation format conversion at a symbol rate of 10 GS/s is feasible by the proposed scheme.

4.5 Performance of the OOK to 16QAM format converter

4.5.1 Influence of OOK signals' pulse shape

Since the phase shift is proportional to the power of the control pulses as indicated in Eq. (4.2), the shape of the phase shift of the probe pulse follows the control signals' pulses shape. Thus, the pulse shape is also an important factor when employing XPM effect. The influence of the OOK control signals' pulse shape will be examined in this section.

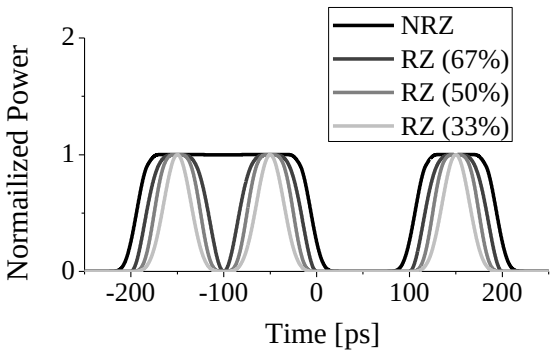

Fig. 4.11. Intensity waveforms of 33%, 50%, 67% RZ and NRZ-OOK signals.

The intensity waveforms of different OOK signals are summarized in Fig. 4.11. The RZ signal waveforms with duty ratios of 33%, 50%, and 67% can be written as

$$E_{\mathrm{RZ\_33}}(t)=\begin{cases}\sqrt{P_{\mathrm{RZ\_33}}}\sin\left(\dfrac{\pi}{2}\left[1+\sin\left(\dfrac{\pi t}{T_s}\right)\right]\right), & |t|\le\dfrac{T_s}{2}\\ 0, & \text{otherwise}\end{cases} \tag{4.17}$$

$$E_{\mathrm{RZ\_50}}(t)=\begin{cases}\sqrt{P_{\mathrm{RZ\_50}}}\sin\left(\dfrac{\pi}{4}\left[1+\cos\left(\dfrac{2\pi t}{T_s}\right)\right]\right), & |t|\le\dfrac{T_s}{2}\\ 0, & \text{otherwise}\end{cases} \tag{4.18}$$

$$E_{\mathrm{RZ\_67}}(t)=\begin{cases}\sqrt{P_{\mathrm{RZ\_67}}}\sin\left(\dfrac{\pi}{2}\cos\left(\dfrac{\pi t}{T_s}\right)\right), & |t|\le\dfrac{T_s}{2}\\ 0, & \text{otherwise}\end{cases} \tag{4.19}$$

For OOK signals with a bit rate of 10 Gb/s, the symbol interval $T_s = 100$ ps. $E_{\mathrm{RZ\_x}}(t)$ and $P_{\mathrm{RZ\_x}}$ are the electric fields and the peak powers of the RZ-OOK signals with different duty cycles of 33%, 50%, and 67%, respectively. On the other hand, the electric field of the NRZ-OOK signal $E_{\mathrm{NRZ}}(t)$ is bit-pattern depended function represented by

$$E_{\mathrm{NRZ}}(t)=\begin{cases}\sqrt{P_{\mathrm{NRZ}}}, & |t|\le\dfrac{(1-a)T'_s}{2}\\ \dfrac{\sqrt{P_{\mathrm{NRZ}}}}{2}\left[1-\sin\left(\dfrac{\pi(|t|-T'_s/2)}{aT'_s}\right)\right], & \dfrac{(1-a)T'_s}{2}\le|t|\le\dfrac{(1+a)T'_s}{2}\\ 0, & \text{otherwise}\end{cases} \tag{4.20}$$

where T'_s is the time interval for continuous "1" signals, namely $T'_s = NT_s$, where N is the length of each signal train segment with continuous "1" signals, a is a parameter taking from 0 to 1 which determines the pulse width. In our simulation, a was assumed as 0.45. $E_{\mathrm{NRZ}}(t)$ and P_{NRZ} are the electrical field and the peak power of the NRZ-OOK signals, respectively.

The simulation results of the I-Q diagram in terms of optical power and eye diagram of the output 16QAM signal are shown as Fig. 4.12 for different OOK signals' pulse shapes of RZ-OOK signals with duty cycles of 33%, 50%, 67% and NRZ-OOK signal. The results show that the 16QAM signal converted from the OOK signals with a larger pulse width has a better signal quality. This may be

RZ (33%):

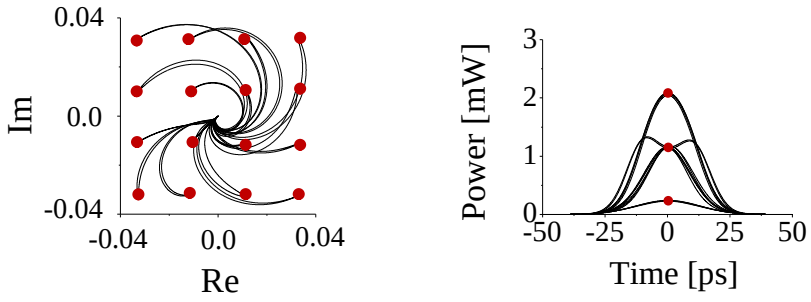

RZ (50%):

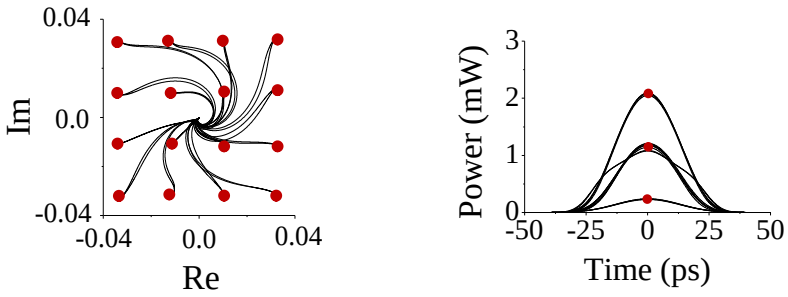

RZ (67%):

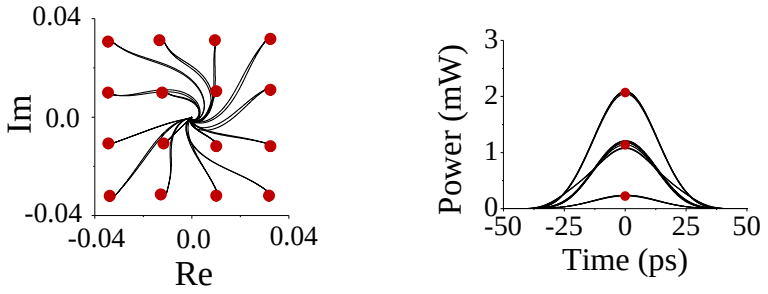

NRZ (*a*=0.45):

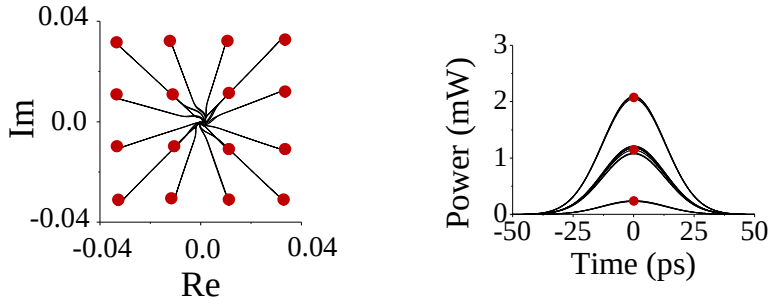

Fig. 4.12 The I-Q diagram and intensity eye diagram of the output 16QAM signal observed at the output of the converter for various pulse widths of OOK signal. The bit rate is 10 Gb/s.

because the full signal power effectively contributes to the phase shift when the OOK pulse width is large. Besides, if full power OOK signals are employed as control pulses, the converter is robust against the walk-off between the control and probe pulses.

4.5.2 Power tolerance of the control pulses

The results shown in Section 4.4 are obtained from ideal parameter values listed in Table 4.2. Unfortunately, however, non-ideal peak powers of the OOK signals result in imperfect phase modulation onto the two QPSK signals, and non-ideal power of the CW pump light results in imperfect amplitude ratio between two QPSK signals. In this section, the power tolerance of the converter will be analytically evaluated.

We calculate the error vector magnitude (EVM) to evaluate the tolerance of power deviation in the conversion. The EVM is defined as the mean square root of the difference between the 16QAM signal converted with ideal power and that with actual power of the control light or the CW pump light, normalized by the mean square of the 16QAM signals which are converted under the ideal power operation, that is

$$\mathrm{EVM} = \sqrt{\frac{\sum_{\mathrm{k}} \left|\mathrm{e}(k)\right|^2}{\sum_{\mathrm{k}} \left|E_{\mathrm{out\_ideal}}(k)\right|^2}}. \tag{4.21}$$

Here, $E_{\mathrm{out\_ideal}}(k) = E_{\mathrm{out}}(k\Delta t)$ is a sample of the ideal output signal and $\mathrm{e}(k) = \mathrm{e}(k\Delta t)$ is a sampled error signal defined as

$$\mathrm{e}(k) = E_{\mathrm{out}}(k) - E_{\mathrm{out\_ideal}}(k), \tag{4.22}$$

where $E_{\mathrm{out}}(k) = E_{\mathrm{out}}(k\Delta t)$ is the sampled actual output signal. Δt represents the sampling period. The sampling point of the *k*-th converted 16QAM signal pulse is the central time point of the *k*-th symbol period.

The electric field observed at the output of this converter is expressed as Eq. (4.12), which can be modified for non-ideal case as

$$E_{\mathrm{out}} = \frac{1}{2} E_{\mathrm{in}} \exp\left[j\left(\Phi_{\mathrm{cp}} + \Phi_{\mathrm{cw}}\right)\right]\left[\exp\left(j\Phi_{\mathrm{c}}\right) - (2+\alpha)\exp\left(j\Phi_{\mathrm{cc}}\right)\right]. \tag{4.23}$$

Here, Φ_{c} and Φ_{cc} are the phase changes of the clockwise and counter-clockwise probe pulses induced by non-ideal OOK signals, and are given by Eq. (4.2). α is the amplitude difference relative

to ideal 1:2 ratio and is related to the parametric gain induced by the non-ideal CW pump light as

$$G = \frac{P_{\mathrm{QPSK1}}}{P_{\mathrm{QPSK2}}} = \frac{\left|E_{\mathrm{QPSK1}}\right|^2}{\left|E_{\mathrm{QPSK2}}\right|^2} = (2+\alpha)^2. \tag{4.24}$$

We define the peak power difference ΔP_j $(j = 1, 2, 3, 4)$ as

$$P_j = P_j - P_{j\_\mathrm{ideal}}\,, \tag{4.25}$$

where P_j is the actual peak power of OOK-j and P_{j_ideal} is the ideal peak power given by Eq. (4.4). Using Eq. (4.25), the phase differences, $\Delta\Phi_{\mathrm{c}}$ and $\Delta\Phi_{\mathrm{cc}}$, can be expressed as

$$\begin{aligned} \Delta\Phi_{\mathrm{c}} &= \Phi_{\mathrm{c}} - \Phi_{\mathrm{c\_ideal}} = 2\gamma L_{\mathrm{eff}}\left(\Delta P_1 + \Delta P_2\right), \\ \Delta\Phi_{\mathrm{cc}} &= \Phi_{\mathrm{cc}} - \Phi_{\mathrm{cc\_ideal}} = 2\gamma L_{\mathrm{eff}}\left(\Delta P_3 + \Delta P_4\right), \end{aligned} \tag{4.26}$$

where $\Phi_{\mathrm{c\_ideal}}$ and $\Phi_{\mathrm{cc\_ideal}}$ are the ideal phase changes induced by P_{j_ideal}. Substituting Eqs. (4.23) and (4.26) into Eq. (4.22), the sampled error signal can be expressed as

$$\begin{aligned} \mathrm{e}(k) = \frac{1}{2}E_{\mathrm{in}}\exp\left(j\Phi_{\mathrm{cp}} + \Phi_{\mathrm{cw}}\right)\{&\exp\left(j\Phi_{\mathrm{c\_ideal}}\right)\left[\exp\left(j\Delta\Phi_{\mathrm{c}}\right) - 1\right] \\ &- \exp\left(j\Phi_{\mathrm{cc\_ideal}}\right)\left[(2+\alpha)\exp\left(j\Delta\Phi_{\mathrm{cc}}\right) - 2\right]\}. \end{aligned} \tag{4.27}$$

Substituting Eqs. (4.12) and (4.27) into Eq. (4.21), we obtain

$$\mathrm{EVM} = \sqrt{\frac{\sum_k a(k)}{\sum_k 5 - 4\cos[\Phi_{\mathrm{c\_ideal}}(k) - \Phi_{\mathrm{cc\_ideal}}(k)]}}, \tag{4.28}$$

where

$$\begin{aligned} a(k) = (\alpha+2)^2 + 6 - 2\cos\left[\Delta\Phi_{\mathrm{c}}(k)\right] - 4(2+\alpha)\cos\left[\Delta\Phi_{\mathrm{cc}}(k)\right] \\ -2[(2+\alpha)\left\{\cos\left[\Phi_{\mathrm{c}}(k) - \Phi_{\mathrm{cc}}(k)\right] - \cos\left[\Phi_{\mathrm{c\_ideal}}(k) - \Phi_{\mathrm{cc}}(k)\right]\right\} \\ -2\left\{\cos\left[\Phi_{\mathrm{c}}(k) - \Phi_{\mathrm{cc\_ideal}}(k)\right] - \cos\left[\Phi_{\mathrm{c\_ideal}}(k) - \Phi_{\mathrm{cc\_ideal}}(k)\right]\right\}]. \end{aligned} \tag{4.29}$$

Assuming a deterministic deviation of the control and CW lights and the equal appearing probability

of 16 kinds of 16QAM signal, we have

$$\sum_{k=1}^{16}\cos[\Phi_{\mathrm{c\_ideal}}(k)-\Phi_{\mathrm{cc\_ideal}}(k)]=0. \tag{4.30}$$

Substituting Eq. (4.30) into Eq. (4.28), we obtain

$$\mathrm{EVM}=\sqrt{\frac{(\alpha+2)^2+6}{5}-\frac{1}{40}\sum_{k=1}^{16}b(k)}, \tag{4.31}$$

where

$$\begin{aligned} b(k)=&\cos\left[\Delta\Phi_{\mathrm{c}}(k)\right]+2(2+\alpha)\cos\left[\Delta\Phi_{\mathrm{cc}}(k)\right]+(2+\alpha)\left\{\cos\left[\Phi_{\mathrm{c}}(k)-\Phi_{\mathrm{cc}}(k)\right]\right.\\ &\left.-\cos\left[\Phi_{\mathrm{c\_ideal}}(k)-\Phi_{\mathrm{cc}}(k)\right]\right\}-2\cos\left[\Phi_{\mathrm{c}}(k)-\Phi_{\mathrm{cc\_ideal}}(k)\right]. \end{aligned} \tag{4.32}$$

Firstly, we derive the EVM induced by the deviation of OOK1 or OOK2. In this case, $\Delta\Phi_{\mathrm{cc}}=\alpha=0$ and 8 kinds of 16QAM signal deviate from the ideal signal points as shown in Fig. 4.14(a). Then, the EVM is expressed as

$$\begin{aligned} \mathrm{EVM}&=\sqrt{\frac{2}{5}-\frac{1}{40}\left\{8+\sum_{k=1}^{8}\cos[2\gamma L_{\mathrm{eff}}\Delta P_j(k)]\right\}}\\ &=\sqrt{\frac{1}{5}\left\{1-\cos\left[\pi\frac{\Delta P_j}{P_{2\_\mathrm{ideal}}}\right]\right\}}\\ &\cong\frac{\pi\left|\Delta P_j\right|}{\sqrt{10}P_{2\_\mathrm{ideal}}} \qquad \text{for } j=1,2. \end{aligned} \tag{4.33}$$

Here, we used Eq. (4.4) to derive the second line in the right-hand side. Next, we consider the EVM induced by the deviation of OOK3 or OOK4. In this case, $\Delta\Phi_{\mathrm{c}}=\alpha=0$ and 8 kinds of 16QAM signal deviate from the ideal signal points as shown in Fig. 4.14(b). Then, the EVM can be expressed as

$$\begin{aligned} \mathrm{EVM}&=2\sqrt{\frac{2}{5}-\frac{1}{40}\left\{8+\sum_{k=1}^{8}\cos[2\gamma L_{\mathrm{eff}}\Delta P_j(k)]\right\}}\\ &=2\sqrt{\frac{1}{5}\left\{1-\cos\left[\pi\frac{\Delta P_j}{P_{4\_\mathrm{ideal}}}\right]\right\}}\\ &\cong\frac{2\pi\left|\Delta P_j\right|}{\sqrt{10}P_{4\_\mathrm{ideal}}} \qquad \text{for } j=3,4. \end{aligned} \tag{4.34}$$

Here, we used Eq. (4.4) to derive the second line of the right-hand side. Based on Eqs. (4.33) and (4.34), we calculate the EVM induced by the deviation of each OOK signals.

The analytical and numerical results are shown in Fig. 4.13 by lines and symbols, respectively. In the numerical simulation, the parameters of the two HNLFs and the wavelengths of the probe and the control lights are the same as those shown in Tables 4.1 and 4.2, except that the peak power of the probe pulse is 3 dBm.

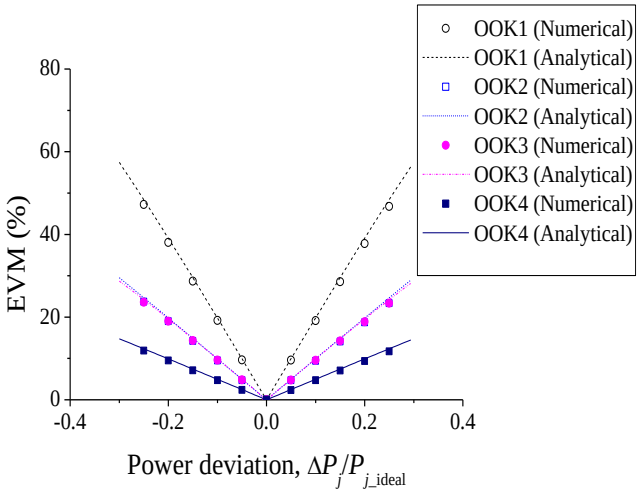

Fig. 4.13. The tolerance against peak power deviations of four OOK signals.

As shown in Fig. 4.13, the analytical results have a good agreement with the numerical results. The EVM almost linearly increases along with the absolute value of ΔP_j in all the results. According to Eqs. (4.33) and (4.34), the EVM for the deviation of OOK 3 and 4 is two times larger than OOK 1 and 2 because of the two times amplitude difference between QPSK1 and QPSK2 signals. Besides, the EVM for the deviation of OOK2 and 4 used for inducing π phase shift is two times larger than OOK1 and 3 which are used for inducing π/2 phase shift to the probe pulse.

The converted 16QAM signal constellations for some $\Delta P_1/P_{1\_ideal}$ are shown in Fig. 4.14(a) by the filled squares and triangles, where the QPSK 2 signals are also represented by the open circles. In order to understand the dynamics of signal points, dotted lines are used to connect the four-point signal sets of QPSK 1 and QPSK2. In these results, we can observe that the non-ideal peak power of OOK1 signal results in a phase drift proportional to the power difference between the non-ideal and the ideal QPSK 1 signals, in addition to the four-point signal set of the QPSK2 remains on its ideal position. The converted 16QAM signal constellations for some $\Delta P_3/P_{3\_ideal}$ are presented in Fig. 4.14(b) by the filled squares and triangles. From these, four points signal set of the QPSK 1 remains their ideal position, but the phase drifts proportional to the power difference between the actual and the ideal QPSK2 signals. This is shown by the open squares and triangles.

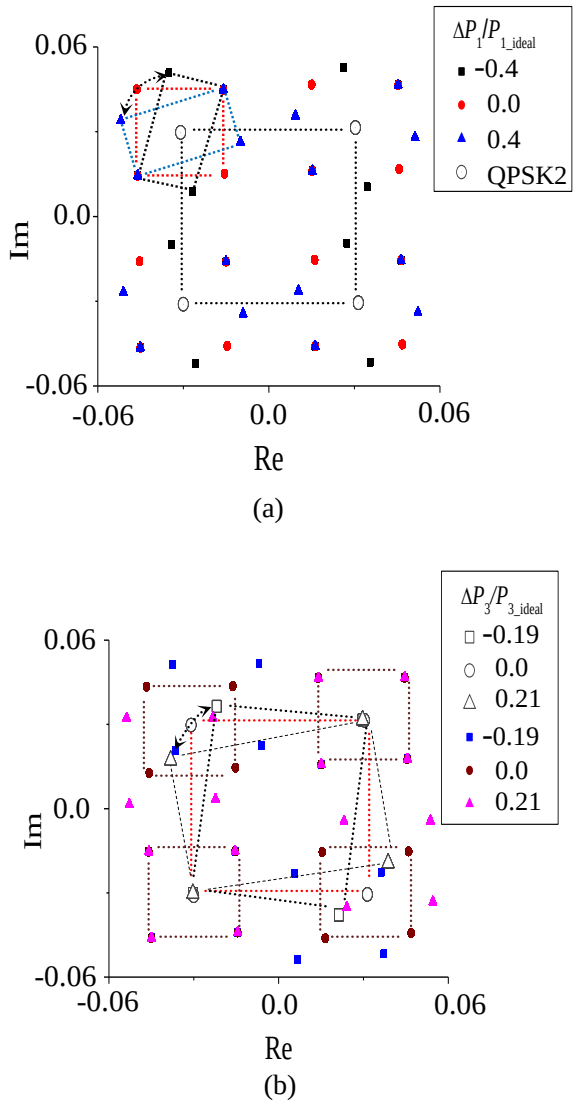

Fig. 4.14. I-Q diagram of the converted 16QAM signal from four OOK signals with a length of 2^{13}-1 PRBS. (a) for $\Delta P_1/P_{1\_ideal}$. (b) for $\Delta P_3/P_{3\_ideal}$.

The output power of the control OOK signals is quite high. Whereas the peak power of the OOK signal pulses of data of 0 is assumed to zero in the previous sections, the residual off level of the OOK signals can affect the converter performance. Thus issue is disscussed in the following. The extinction ratio of four OOK signals is defined as

$$R=10\times\log\left(\frac{P_{j\_0}}{P_{j\_1}}\right), \tag{4.35}$$

where P_{j_0} and P_{j_1} are the powers of the zero and one pulses, respectively. The nonzero power of

the off state induces undesired phase shift onto the probe pulses. However, the effect of extinction ratio can be compensated by readjusting the ideal power of OOK signal as

$$P_{j\_1} = P_{j\_\text{ideal}} + P_{j\_0}, \tag{4.36}$$

with

$$\Phi_0 = 2\gamma L_{\text{eff}} \left(P_{1\_0} + P_{2\_0} \right) \cong 2\gamma L_{\text{eff}} \left(P_{3\_0} + P_{4\_0} \right). \tag{4.37}$$

From Eq. (4.12), the output signal can be expressed as

$$E_{\text{out}} = \frac{1}{2} E_{\text{in}} \exp\left[j\left(\Phi_{\text{cp}} + \Phi_0 + \Phi_{\text{cw}} \right) \right] \left[\exp\left(j\Phi_{\text{c\_ideal}} \right) - 2\exp\left(j\Phi_{\text{cc\_ideal}} \right) \right]. \tag{4.38}$$

Finally, we consider the EVM induced by the deviation of the CW pump light. In this case, $\Delta\Phi_c = \Delta\Phi_{cc} = 0$, and then the EVM can be expressed as

$$\text{EVM} = \frac{|\alpha|}{\sqrt{5}}. \tag{4.39}$$

The EVMs due to the deviation of CW pump light calculated by the numerical simulation and that by Eq. (4.39) are shown in Fig. 4.15. The agreement between those results is very well for small α, where for large α, the numerical results are larger than the analytical ones. This is because the term $\Delta\Phi_{\text{cw}} = 2\gamma L_{\text{eff}} \Delta P_{\text{cw}}$ is ignored in Eq. (4.23).

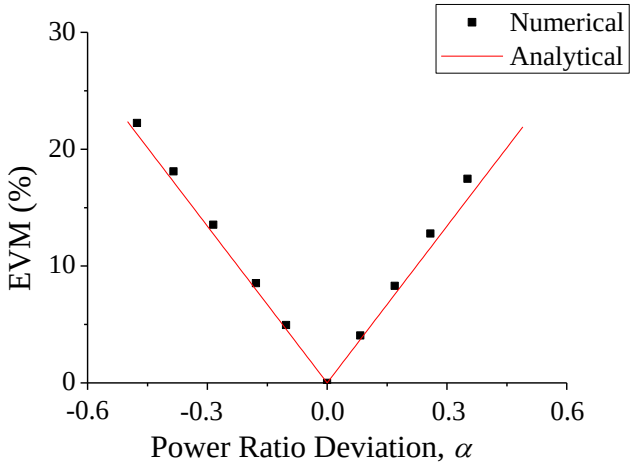

Fig. 4.15. Power tolerance for CW pump light.

4.6 Conclusion

An all-optical RZ-OOK to RZ-BPSK format conversion scheme has been introduced in this chapter in order to well understand the XPM employed in amplitude-to-phase modulation format conversion. We experimentally demonstrated an error-free operation of this format conversion at a bit rate of 10.7 Gb/s. In addition, we investigated the CD and timing tolerance of the converter.

As a main research work of thesis, an all-optical OOK to 16QAM modulation format conversion scheme using NOLM has been proposed and numerically demonstrated, and the tolerance against the power deviation has been analytically evaluated. A 16QAM signal is generated as a result of super-position of two QPSK signals with different amplitudes. In the converter, the nonlinear effects of XPM and OPA are employed in the converter for OOK to QPSK format conversion and achieving 2:1 amplitude ratio between two QPSK signals, respectively. It is noteworthy that this technique enables to realize a transparent gateway node for 100 Gb/s and beyond because XPM and OPA in optical fibers are ultrafast phenomena with a response time less than sub-picoseconds. The influence of the pulse shape of the control pulses has been discussed because it is an important factor when employing XPM effect. The peak powers of all the control lights are the key parameter in these nonlinear phenomena. The power tolerance for the 4-channel OOK signals and the CW pump light of the converter has been also analytically evaluated and simple relations between the EVM and the power deviations have been derived.

Chapter 5

OOK to 16QAM format conversion employing NOLM with 1:2 coupler

In order to experimentally demonstrate all-optical OOK to 16QAM format conversion, a simplified configuration of the converter with a 1:2 coupler employed in the NOLM will be described in this chapter. The first experimental demonstration of an all-optical modulation format conversion from NRZ–OOK to RZ–16QAM in NOLM with a 1:2 coupler configuration will be presented at 10 GS/s. Regarding a problem observed in the experimental results, the effect of the ASE noise accompanied with the amplified OOK signals from an EDFA will be numerically studied.

5.1. Introduction

Due to the rapidly worldwide growing data and internet traffic in telecommunication networks, the next-generation optical networks will require significant improvements in transmission capacity. The 16QAM modulation format is an attractive multi-level modulation format which possesses outstanding performance of transmission capacity, implying its potentiality for the next generation transmission system of higher than 100G. However, its large constellation size significantly reduces the tolerance against noise and nonlinear impairments and limits the feasible transmission reach. One conclusion maybe that the 16QAM format is employed in MAN. Researches will unremittingly explore the practicability of 16, 32, or 64QAM format employed in a WDM channel at a bit rate of 400 Gb/s for long-haul WANs in a cost-effective manner. On the other hand, the conventional OOK formats may keep their main role in MANs and access networks or rarely incorporate with the multi-level modulation format in the WANs. The function of OOK to 16QAM format conversion will be an important interface technology for a gateway between optimally designed WAN and MAN

(or MAN and access networks), which separately employ different modulation formats.

An all–optical OOK to 16QAM format converter based on XPM and OPA in a NOLM was numerically demonstrated in Chapter 4. The influence of the OOK signal's pulse shape was theoretically discussed for that it is an important factor when employing the XPM effect. According to these simulation results, the NRZ–OOK format provides the best performance because of its relative full phase modulation to the probe light. Traditionally, a 1:1 coupler is employed in a NOLM. In such a NOLM, a CW pump light was required to induce 6-dB amplitude ratio via OPA in HNLF between the clockwise and counter-clockwise probe pulses. The scheme proposed in the previous chapter needs a complicated parameter design, which implies a difficulty in experimental implementation. In this chapter, an experimental demonstration of the all-optical NRZ–OOK to RZ–16QAM format conversion with a simplified configuration will be presented. The complexity of the scheme proposed in the previous chapter can be reduced by replacing the 1:1 coupler with a 1:2 coupler in the NOLM. In this way, one HNLF and the CW pump light for OPA can be removed to construct a simple and cost effective setup. The all-optical modulation format conversion from NRZ–OOK to RZ–16QAM in NOLM with the 1:2 coupler configuration will be experimentally demonstrated at 10 GS/s. The simulation and experimental results confirm the feasibility of this proposed converter. However, the phases of the generated 16QAM signals are affected by the amplitude-to-phase-noise conversion due to the amplitude-dependent property of XPM. In our scheme, the OOK signals should be amplified to high power before launched into the HNLF for intensity-to-phase conversion [76], where the ASE noise from the amplifiers degrades the quality of the converted phase. The effect of ASE noise will be theoretically discussed to improve the performance of the converter.

5.2 Simplified configuration with 1:2 coupler employed in a NOLM

Fig. 5.1 shows the configuration of the simplified modulation format converter which is basically a NOLM with a 1:2 coupler. The 1:2 coupler is used in place of the 1:1 coupler in the previous chapter. In this configuration, the HNLF and the CW pump light for amplifying the transmitted probe pulse in one branch are not required. This simplified configuration is expected to provide a better cost efficiency and stable operation. The operation principle can be easily understood by Fig. 5.1. In Fig. 5.1, we define four ports of the 1:2 couplers as ports 1, 2, 3, and 4. The 1:2 coupler has the 1:2 power-splitting ratio and the phases of the coupled output signal and the through output signal are 90° shifted. Port 3 is the input port of this converter. When the probe pulse is incident to the NOLM from the coupler, it is split into two pulses at ports 1 and 2. Denoting the electrical field

of the input probe pulse as E_{in}, the relation between the input and the output electrical fields at ports 1 and 2 can be expressed as

$$E_1 = \frac{1}{\sqrt{3}} E_{in},$$
$$E_2 = j\sqrt{\frac{2}{3}} E_{in}. \tag{5.1}$$

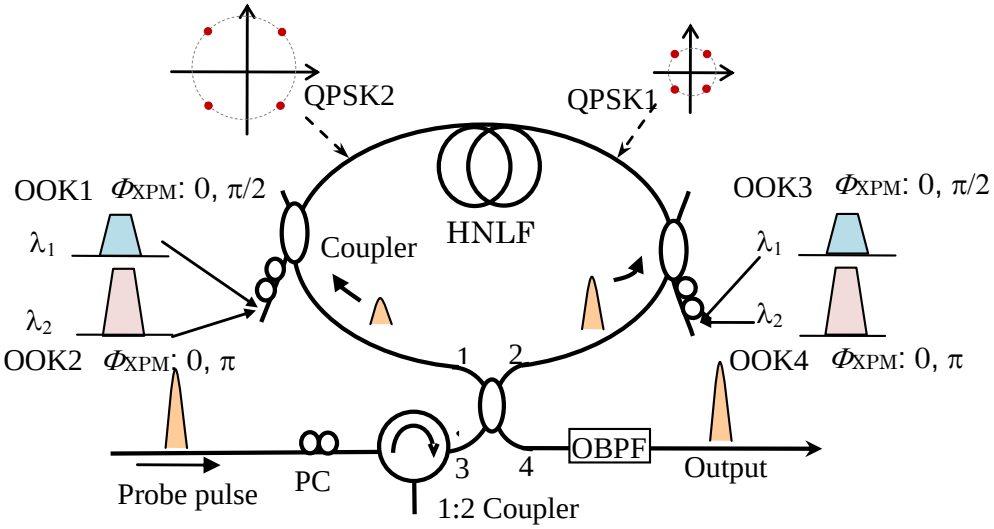

Fig. 5.1. Schematic diagram of the proposed modulation format converter.

The probe pulses, that are split into ports 1 and 2, travel through the loop in the clockwise and counter-clockwise directions, respectively. The clockwise OOK signals 1 and 2 are used to modulate the clockwise probe pulse to be QPSK1 by XPM in the HNLF as shown in Fig. 5.1. On the other hand, the counter-clockwise OOK signals 3 and 4 are used for creating QPSK2. For simplicity, we presume here the use of a polarization-maintaining (PM)-HNLF, or an equivalent, so that only one polarization state of the optical field needs to be considered [77]. According to Eq. (2.9), the nonlinear phase changes of the clockwise and counter-clockwise probe pulses which are induced by the co-propagating OOK signals via XPM can be given by

$$\Phi_c = 2\gamma L_{eff}\left(P_{OOK1} + P_{OOK2}\right),$$
$$\Phi_{cc} = 2\gamma L_{eff}\left(P_{OOK3} + P_{OOK4}\right), \tag{5.2}$$

where γ and L_{eff} are the nonlinear coefficient and the effective interaction length of the fiber, respectively. $P_{\text{OOK}i}$ are the peak powers of the OOK*i* signals. After one-round transmission, the electrical fields of the probe pulses at ports 1 and 2 can be expressed as

$$\begin{aligned} E_1^{\text{T}} &= \exp\left(j\Phi_{\text{cc}}\right)E_2 = j\sqrt{\frac{2}{3}}\exp\left(j\Phi_{\text{cc}}\right)E_{\text{in}}, \\ E_2^{\text{T}} &= \exp\left(j\Phi_{\text{c}}\right)E_1 = \frac{1}{\sqrt{3}}\exp\left(j\Phi_{\text{c}}\right)E_{\text{in}}. \end{aligned} \tag{5.3}$$

An OBPF is used to remove the OOK signals at the NOLM output. Then, at the output of the converter, the electrical field of the probe pulse E_{out} is obtained as

$$E_{\text{out}} = j\sqrt{\frac{2}{3}}E_1^{\text{T}} + \frac{1}{\sqrt{3}}E_2^{\text{T}} = -\frac{1}{3}\left\{2\exp\left(j\Phi_{\text{cc}}\right) - \exp\left(j\Phi_{\text{c}}\right)\right\}E_{\text{in}}. \tag{5.4}$$

This equation indicates that the output signal is a superposition of two QPSK signals with an amplitude ratio of 1:2. Therefore, a 16QAM signal can be generated at the output of the converter. However, non-ideal peak powers of the OOK signals will result in imperfect phase modulation of the two QPSK signals as discussed in the previous chapter. From Eq. (5.2), the non-ideal phase difference depends on the peak-power difference as

$$\begin{aligned} \Delta\Phi_{\text{c}} &= 2\gamma L_{\text{eff}}\left(\Delta P_{\text{OOK1}} + \Delta P_{\text{OOK2}}\right), \\ \Delta\Phi_{\text{cc}} &= 2\gamma L_{\text{eff}}\left(\Delta P_{\text{OOK3}} + \Delta P_{\text{OOK4}}\right). \end{aligned} \tag{5.5}$$

Here, $\Delta P_{\text{OOK}i}$ is the power difference between the noisy and the ideal OOK*i* signals. If the ASE noise in the amplified OOK signals is assumed to be additive white Gaussian noise (AWGN), the probability density function of $\Delta P_{\text{OOK}i}$ is a Gaussian distribution as

$$\text{f}(\Delta P_{\text{OOK}i}) = \frac{1}{\sqrt{2\pi}\sigma_{\text{OOK}i}}\exp\left[-\frac{\left(\Delta P_{\text{OOK}i}\right)^2}{2\sigma_{\text{OOK}i}^2}\right], \tag{5.6}$$

where $\sigma_{\text{OOK}i}$ is the standard deviation of the probability distribution of OOK*i* signal's peak power. Squaring and averaging Eq. (5.5) gives a standard deviation of the phase fluctuations as

$$\begin{aligned} \sigma_{\text{c}} &= 2\gamma L_{\text{eff}}\sqrt{\sigma^2{}_{\text{OOK1}} + \sigma^2{}_{\text{OOK2}}}, \\ \sigma_{\text{cc}} &= 2\gamma L_{\text{eff}}\sqrt{\sigma^2{}_{\text{OOK3}} + \sigma^2{}_{\text{OOK4}}}. \end{aligned} \tag{5.7}$$

where σ_c and σ_{cc} represent the standard deviations of the phase fluctuations in the clockwise and counter-clockwise QPSK signals which is proportional to the power fluctuations of the OOK signals. Eq. (5.7) indicates that even moderate power fluctuations in the OOK signals can be converted into considerable phase noise in the probe pulse because of the large nonlinear coefficient and a long interaction length of the HNLF.

5.3 Experimental demonstration

The experimental setup of the converter is shown in Fig. 5.2. The generation unit of NRZ-OOK signals is shown in the top left dotted box. CW lights from tunable laser sources 1 (TLS 1) and 2 (TLS 2) with wavelengths of 1546.2 nm and 1550.3 nm, respectively, were modulated together to be NRZ-OOK signals with a 10 Gb/s PRBS of length 2^{15}-1 by an intensity modulator (IM). A phase modulator was also used after the IM in order to suppress the SBS [75] which may emerge when high power OOK signals enter the PM-HNLF. Then, a 3-dB OC followed by OBPFs with a pass-width of 0.4 nm was used to separate the generated NRZ-OOK signals so that the different wavelengths went into two branches, respectively. We denote the separated OOK signals with different wavelengths as OOK 1, 3 and OOK 2, 4. They were amplified by two EDFAs to two specified peak powers, separately, for inducing $\pi/2$ and π phase shift onto the probe pulses. Two OBPF with a pass-width of 1nm followed the EDFAs in order to filter out the ASE noise generated from the EDFA. This is because ASE would induce fluctuations in the peak powers of the OOK signals, which turn to be phase fluctuations in the generated QPSK signal via XPM in the PM-HNLF. A PM-3dB coupler was used to combine and re-separate the NRZ-OOK signals generated in the upper and lower branches with different wavelengths and peak powers into two groups OOK 1, 2 and OOK 3, 4 for the phase modulations to the clockwise probe pulse and the counter-clockwise probe pulse. A PCs were used to maximize the output powers of the PM-3dB coupler that induced a function of eliminating one linear polarization mode. The VODL were also used to skew the time delay between the OOK signals and the probe pulses. The PM-NOLM for NRZ-OOK to RZ-16QAM modulation format converter is shown in the top right dotted box in Fig. 5.2. In the PM-NOLM, a VOA was used to balance the peak powers of clockwise OOK1, 2 and counter-clockwise OOK3, 4. Two PM-WDM couplers were used to combine the clockwise and the counter-clockwise OOK signals with the probe pulses into both sides of the PM-HNLF. Optical isolators (ISOs) were used before the PM-WDM coupler to remove the OOK signals from the opposite directions. The probe pulse was generated from TLS 3 with a wavelength of 1565nm. PC was used to maximize the input power of the probe pulses. Then, a 16QAM signal is generated at the output of the PM-NOLM. A sampling oscilloscope and an optical coherent receiver followed by a

real-time oscilloscope with a sampling rate of 10 GS/s were used to observe the waveform and the constellation map of the output signal, respectively. The fast polarization mode of the PM-HNLF was used. The zero-dispersion wavelength, the dispersion slope, the loss coefficient, the nonlinear coefficient, and the length of the HNLF were λ_0 = 1590 nm, D_λ =0.024 ps/ nm^2/km, α = 2.7 dB/km, γ = 18.0 W^{-1}km^{-1}, and L = 0.5 km, respectively. The wavelengths of the two OOK signals were set to be 1550.3 nm and 1546.2 nm, respectively.

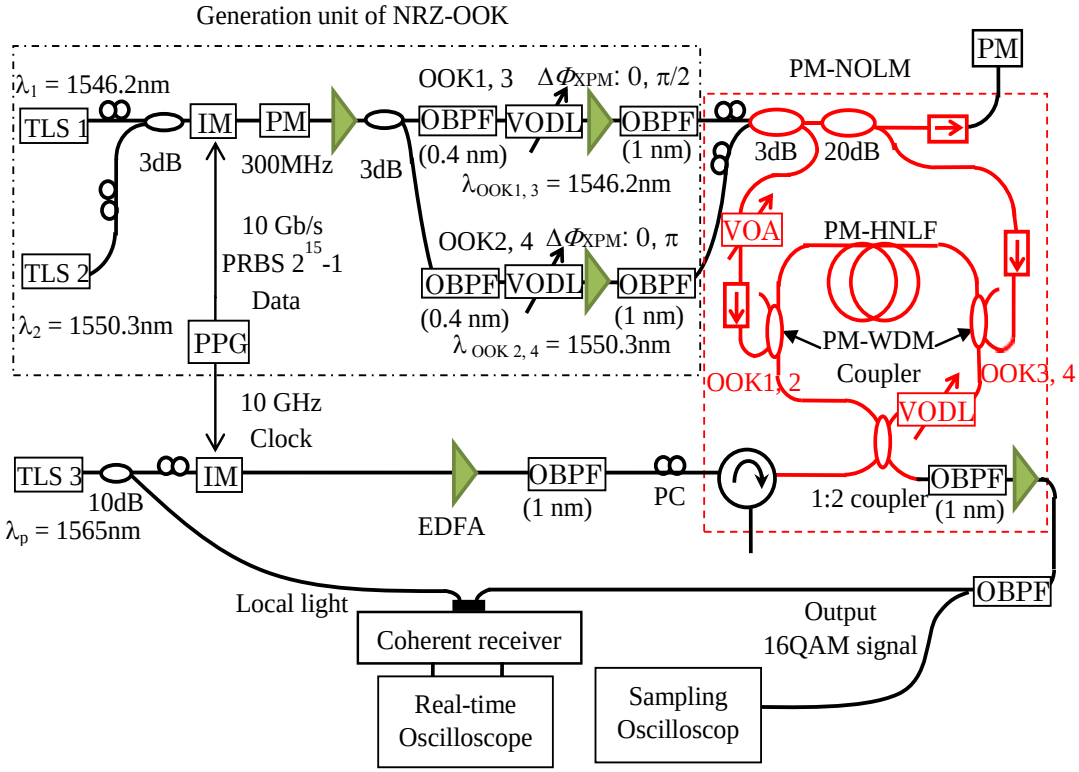

Fig. 5.2 Experimental setup.

The experimental results without using of digital signal processing are shown in Fig. 5.3. Fig. 5.3(b) shows the eye diagram of the power of the output 16QAM signal. The waveform of the output power is shown in Fig. 5.3(a). The 16QAM signals had three power levels with a power ratio of 1:5:9 which were measured as 1.5 mW, 7 mW, and 13 mW. The constellation map of the 16QAM signal is shown in Fig. 5.3(c). The ideal position is also shown by black circles. The open and closed circles respectively indicate constellation points of the clockwise and counter-clockwise probe pulses at the output of the PM-HNLF. We can observe that the output signals suffered from phase noise due to the amplitude-to-phase-noise conversion. The ASE noise generated from the EDFAs, in addition to a bit OPA and Raman gain, may induce random and pattern dependent intensity fluctuation to the OOK signals. The effect of the ASE noise will be theoretically discussed in the next section. In Fig. 5.3(c), the upper half of the constellation map looks so noisy that it is hard to identify each signal

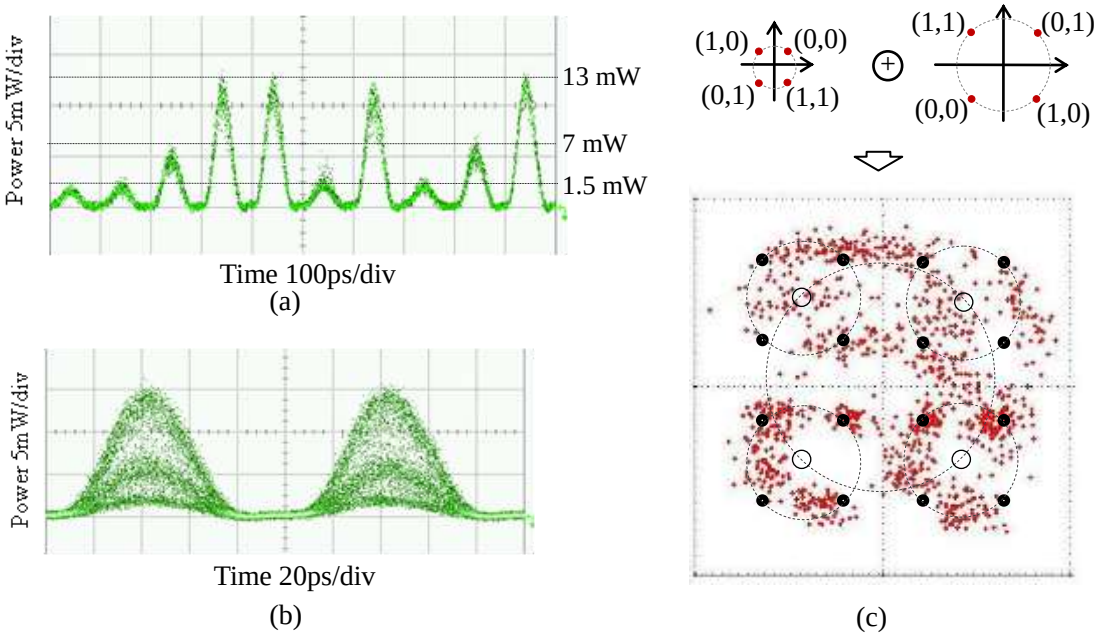

Fig. 5.3. Experimental results of the output signal when the input OOK signals are 10Gb/s PRBS with length of 2^{15}-1. (a) waveform, (b) eye diagram, (c) I-Q constellation map.

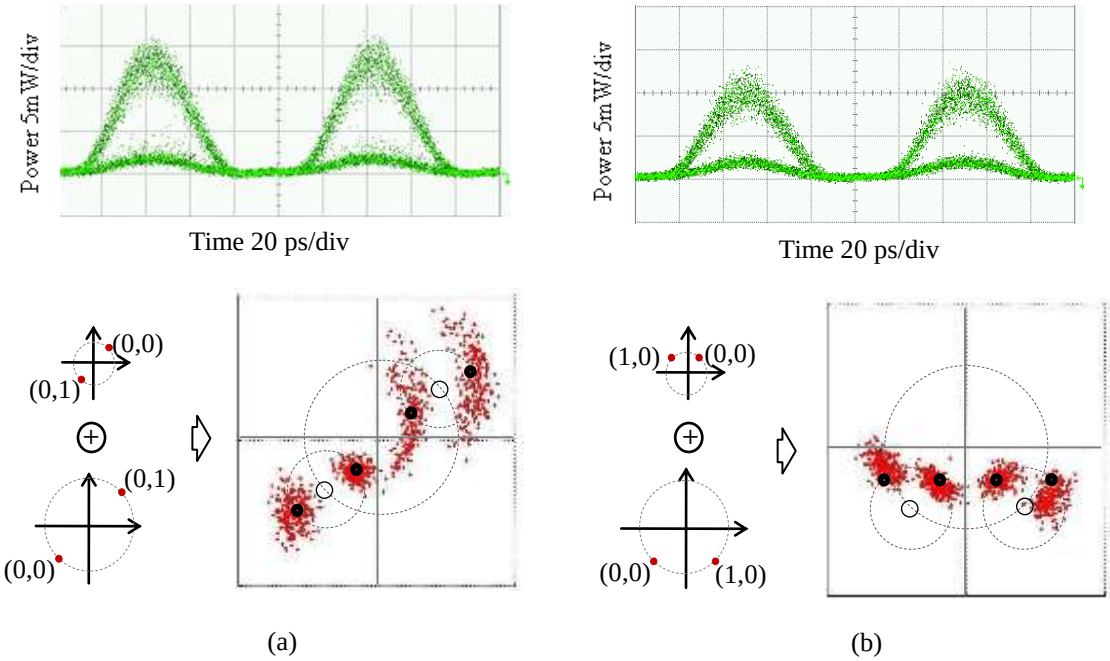

Fig. 5.4. Experimental results of the eye diagram and the I-Q constellation maps of APSK1 and APSK2 when the input OOK signals are 10Gb/s PRBS with a length of 2^{15}-1. (a)APSK1, (b) APSK2.

point. In order to examine the constellation in more detail, APSK1 and APSK2 as part of the 16QAM signal's constellation map were also measured.

When all the OOK 1, 3 signals are fixed as 0, the probe pulse experiences only a phase shift at 0 or π from the control pulses and the amplitude of the output signal only take two levels. This signal is called as the APSK1 signal, and is shown in Fig. 5.4(a). When all the OOK 2, 4 signals are fixed at 0, on the other hand, the probe pulse only get π/2 phase shift from the control pulses. The eye diagram and the constellation map of APSK2 are shown in Fig. 5.4(b). The ideal location of the superposition of two BPSK signals modulated in the clockwise and counter-clockwise branches of the NOLM is also indicated in Fig. 5.4. The above conditions were experimentally achieved by turning off one of the amplifiers in the upper and lower branches. The ideal constellation maps of the clockwise and counter-clockwise probe pulses are shown in the left-hand side of the experimental results. From the constellation maps of APSK1 and APSK2, we can see that the right half of APSK1 suffered from some phase noises since the EDFA used to amplify the OOK signals for π phase modulation was not stable enough. Therefore, the upper half of the 16QAM signals became so noisy that it is hard to identify each point in Fig. 5.3(c).

5.4 Effect of ASE noise from EDFA

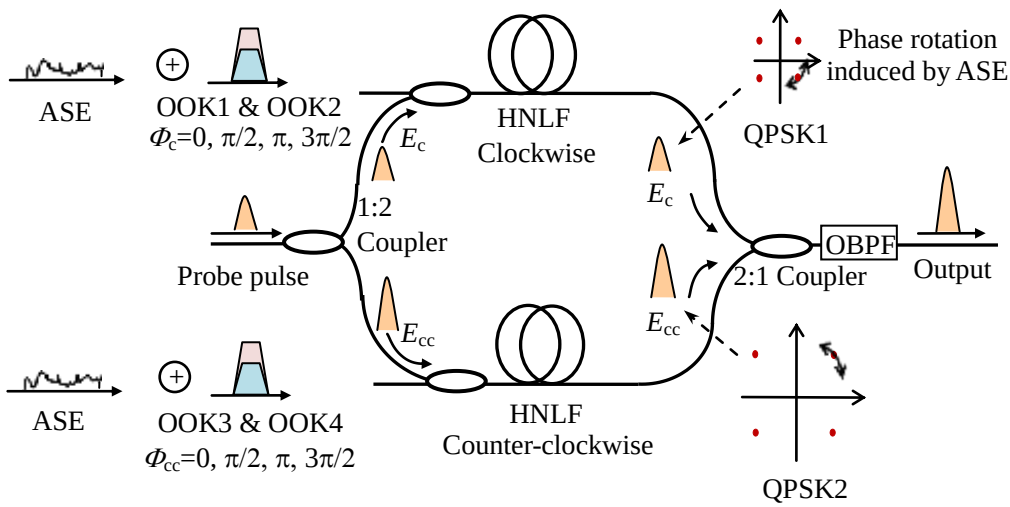

Fig. 5.5 Simulation model.

In this section, the Split-Step Fourier method will be used to evaluate the effect of the ASE noise generated from the EDFAs in the OOK to QPSK/16QAM modulation format converter. The

simulation system model is shown in Fig. 5.5. In Fig. 5.5, probe pulses going to the upper and lower branches of a MZI simulate the clockwise and counter-clockwise probe pulses in the NOLM. In this simulation, the phase change of the clockwise probe pulse induced by counter-propagated OOK signals was not taken into account since the phase difference is small enough to be ignored for long pulse trains of the input OOK signals, as mentioned in Chapter 4. The parameters of the HNLF and the wavelengths of the control and probe pulses were the same as those in the experiment. Fig. 5.6 shows the simulation results of the intensity eye diagram and the constellation map of the output 16QAM signal when the input OOK signals are 10 Gb/s PRBS with a length of 2^7-1 without ASE noise accompanied. The red circles in the constellation map indicate the sampling points of each pulse. The clear eye opening and undistorted constellation points could be obtained under this ideal condition. The ideal peak powers of the OOK signals for inducing π/2 and π phase shift are 20 dBm and 23 dBm, respectively.

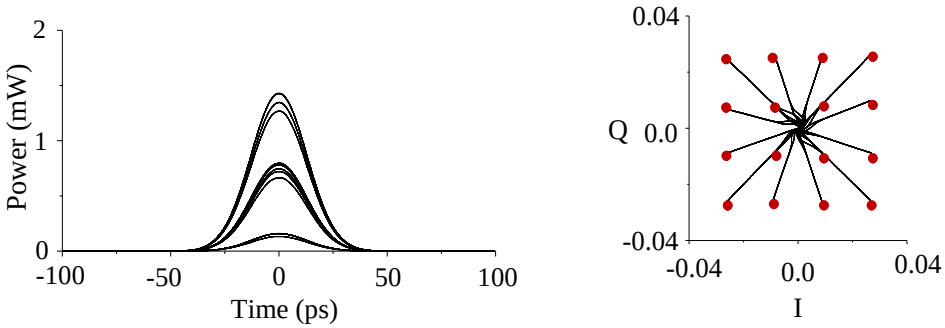

Fig. 5.6. Simulation results of the eye diagram and constellation maps of the output 16QAM signal when the input OOK signals are 10 Gb/s PRBS with a length of 2^7-1 without ASE noise accompanied.

Then, an AWGN was added to the OOK signals as a model of ASE noise. The Gaussian-shape OBPF with a pass-width of 1nm followed the EDFA to cut a wide power spectrum of ASE into a narrow range. The OSNRs of the OOK signals, which were used to induce π/2 (OOK1, 3) and π (OOK2, 4) phase shift onto the probe pulse, were $OSNR_{OOK\_\pi/2}$ = 34.2dB and $OSNR_{OOK\_\pi}$ = 22dB, respectively. The numerically obtained probability density function $f(\Delta P_{OOKi})$ of the peak power fluctuation of the OOK PRBS with a length of 2^{16}-1 is shown with red lines in Fig. 5.7(a). Then, the variance of the numerically obtained power fluctuation of the OOK signals could be calculated by the discrete probability density function $f(\Delta P_{OOKi})$ from

$$\sigma^2_{OOKi} = \sum_{k=1}^{n} \left(\Delta P_{OOKi\_k}\right)^2 f(\Delta P_{OOKi\_k}), \tag{5.8}$$

where *n* is the sum of the discrete points of function $f(\Delta P_{OOKi})$. Substituting Eq. (5.8) into Eq. (5.6), a fitting Gaussian distribution was obtained, which is shown by the black line in Fig. 5.7(a). The peak power to fluctuation ratio (P_{OOKi}/σ_{OOKi}) of the ASE noise added OOK signals is also shown in Fig. 5.7(a). The simulation results of the constellation maps of QPSK1 and QPSK2 signals generated in the upper and lower branches of the Mach-Zehnder interferometer are shown in Figs. 5.7(b) and 5.7(c). Even when the $OSNR_{OOK\_\pi}$ was as low as 18 dB, the phase fluctuation didn't exceed the range of $\pm\pi/4$. The phase fluctuation of the constellation point of QPSK2 was the same as the QPSK1 except the π phase offset. The numerically obtained phase probability distribution functions of each constellation point of the QPSK1 signal were shown in Fig. 5.7(b). The numerically obtained variances of the peak power and phase fluctuation, shown in Figs. 5.7(a) and 5.7(b), come in great agreement with the analytical relation described in Eq. (5.7).

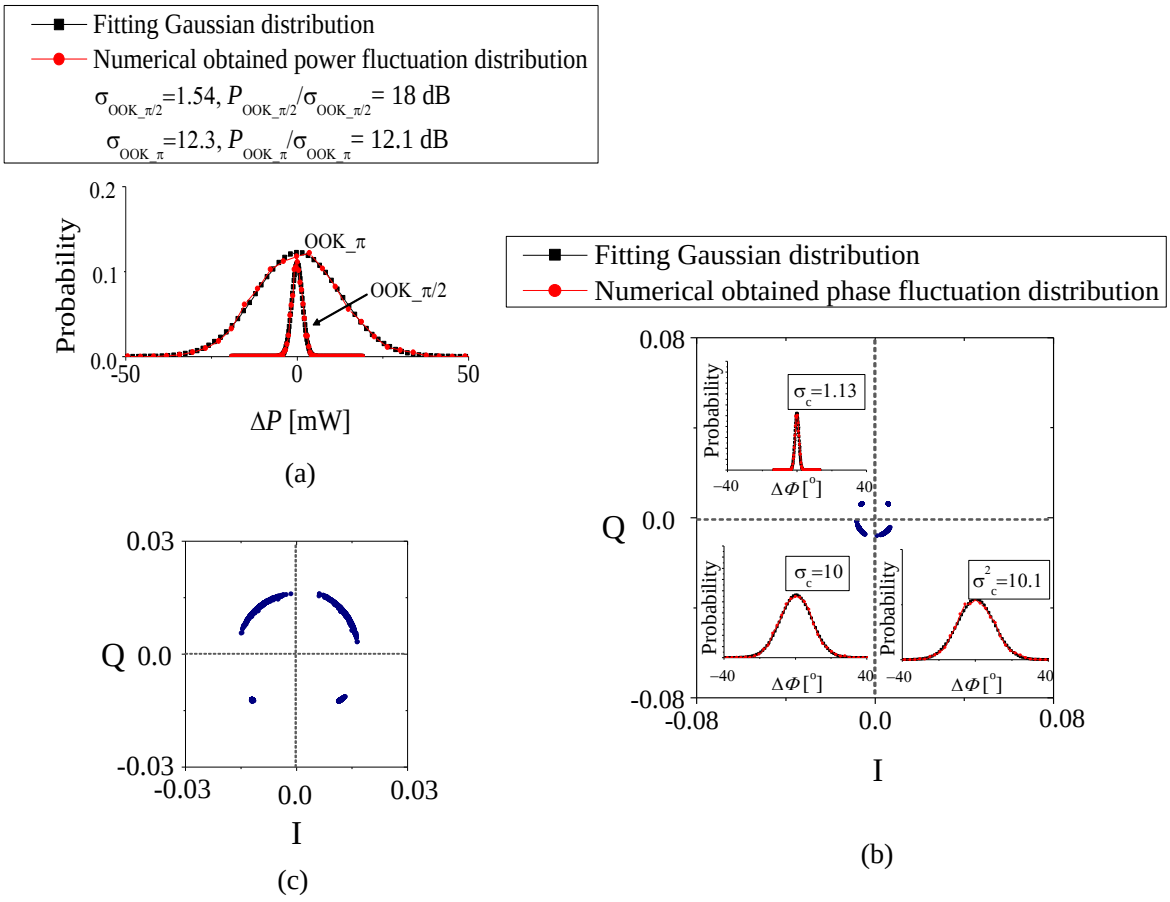

Fig. 5.7. Simulation results of the power distribution and phase distribution. (a) Peak power fluctuation of the OOK signals with ASE noise accompanied. $\Delta P = P_{actual} - P_{ideal}$. (b), (c) I-Q diagram and the phase fluctuation of two phase noisy QPSK1 and QPSK2 signals with π phase offset and 1:2 amplitude ratio which are modulated by the amplitude noisy OOK signals.

Fig. 5.8 shows the simulation results of the constellation map and the intensity eye diagram observed at the output of the converter as a superposition of the two noisy QPSK signals. Each cell was marked by red letters which was divided by the boundry lines of each constellation point. In Fig. 5.8(a), we can find that the 16 constellation points suffer from a rotation with different angles, and errors obviously arise in the upper half of the constellation map for low OSNR of OOK_π signals. Comparing Figs. 5.8(b) and 5.8(c) with the experimental results shown in Figs. 5.3 and 5.4, we can find that the experimental results have an agreement with the simulated results. However, the constellation map of the experimental results seems even worse, maybe because of the non-ideal optical coherent receiver and time mismatching of the real-time oscilloscope. It implies that the constellation map of 16QAM and APSK1 can be improved obviously, if the OOK_π signals were amplified with less ASE noise.

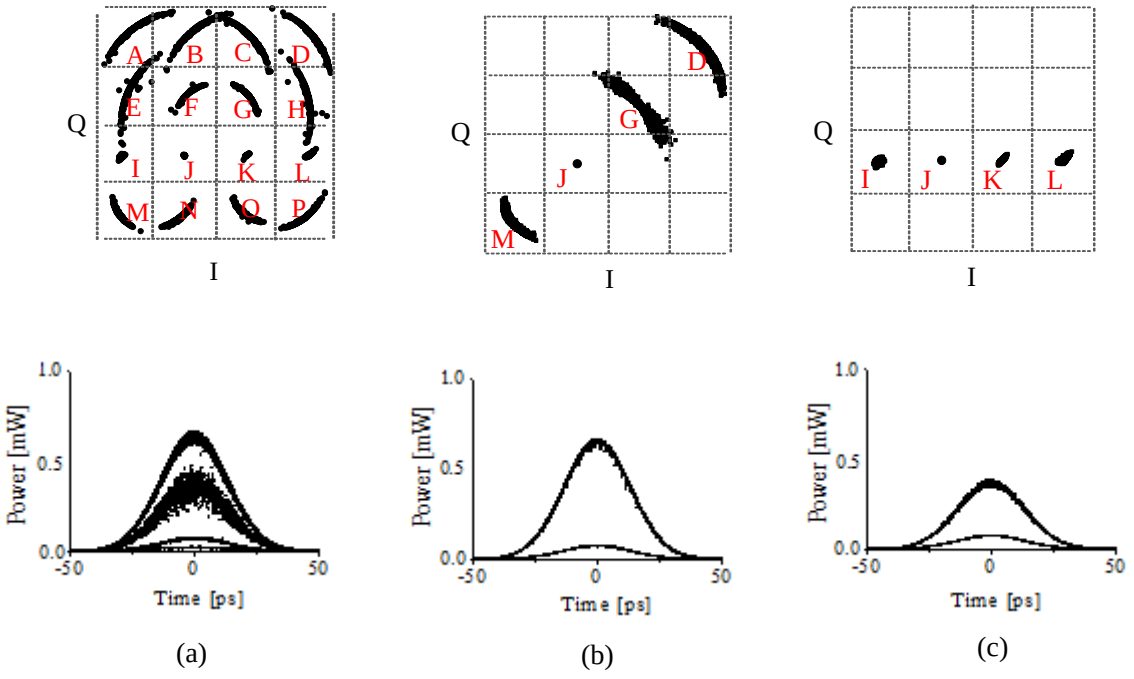

Fig. 5.8. Simulation results of the constelation map and the eye diagram observed at the output of the converter as the superposition of two noisy QPSK signals. (a) 16QAM. (b) APSK1. (c) APSK2. $SNR_{OOK1,\ 3}$=30.2dB, $SNR_{OOK2,\ 4}$= 18dB.

Different from conversion to QPSK signal, the amplitude-to-phase-noise conversion is a crucial problem in the 16QAM signal converter because of the ASE noise accumulated in the two OOK signals is and the compact signal points alignment of the 16QAM signal. Moreover, the noisy constellation points of the converted 16QAM signal are curving in different angles and different

directions. In order to evaluate the BER of the output 16QAM signal, the method of least squares was used to find the fitting circle of each curved constenllation points. In Fig. 5.8(a), the constellation of the output 16QAM signal with the data of (1001) is marked as "C". For instance, a fitting circle of the constellation point "C" is shown in Fig. 5.9(a), where the phase boundry points points on the circle, labeled as Φ_L and $\Delta\Phi_S$, are indicated. The numerically obtained probability distribution function of the phase on the above fitting circle is shown in Fig. 5.9(b). The BER of the converted 16QAM signal could be written as

$$BER = \frac{1}{16}\sum_{i=1}^{16}\left[1-\int_{\Delta\Phi_S}^{\Delta\Phi_L} \mathrm{f}\left(\Delta\Phi_i\right) d\Delta\Phi_i\right], \tag{5.9}$$

where $\mathrm{f}\left(\Delta\Phi_i\right)$ is the fitting phase Gaussian distribution function of each constellation points of the output 16QAM signal with respect to the fitting circle center, $\Delta\Phi_L$ and $\Delta\Phi_S$ represent the phase boundry angles.

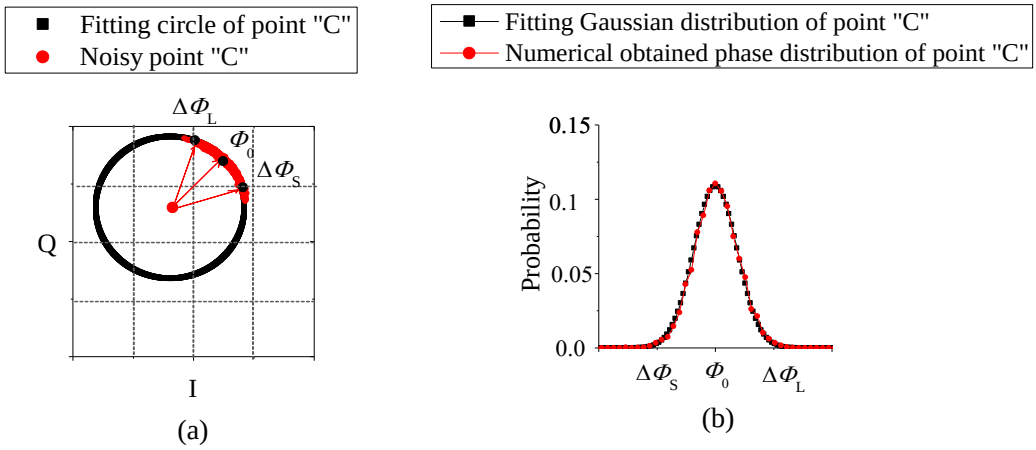

Fig. 5.9(a) The fitting circle for point "C". (b) The phase probability density function of point "C" relative to the fitting circle center.

The simulated BER results of the 16QAM signal versus the peak power fluctuation caused by the ASE noise in the OOK_π and OOK_π/2 signals, separately, are shown in Fig. 5.10. The BER becomes better as the $P_{OOK\_\pi}/\sigma_{OOK\_\pi}$ and $P_{OOK\_\pi/2}/\sigma_{OOK\_\pi/2}$ increases from 12.2 dB to 18 dB, represented by the black and red lines in Fig. 5.10, respectively. The constellation maps of the 16QAM signal is shown in the upper right side of Fig. 5.10 when OSNR of all of the OOK signals is 30.2 dB, P/σ = 18 dB. Compared with Fig. 5.8(a), the signal points on the upper half of the constellation map are obviously condensed for small peak power fluctuation of OOK_π signals. In

addition, the constellation maps of the 16QAM signal, when the OSNR of OOK_π/2 signal is 18 dB, is shown in the lower left side of Fig. 5.10. We can observe that it is different from the constellation maps in Fig. 5.8(a), and that the APSK2 signal has noisy phase if the OSNR of OOK_π/2 signals is low. According to Fig. 5.10, the peak power to fluctuation ratio of all the OOK signals should be larger than 18 dB. Although the simulated result does not precisely tell us how the phase noise will limit the transmission capability of the converted 16QAM modulation format, the errors induced by the amplitude-to-phase-noise conversion could be surmised by the simulation result.

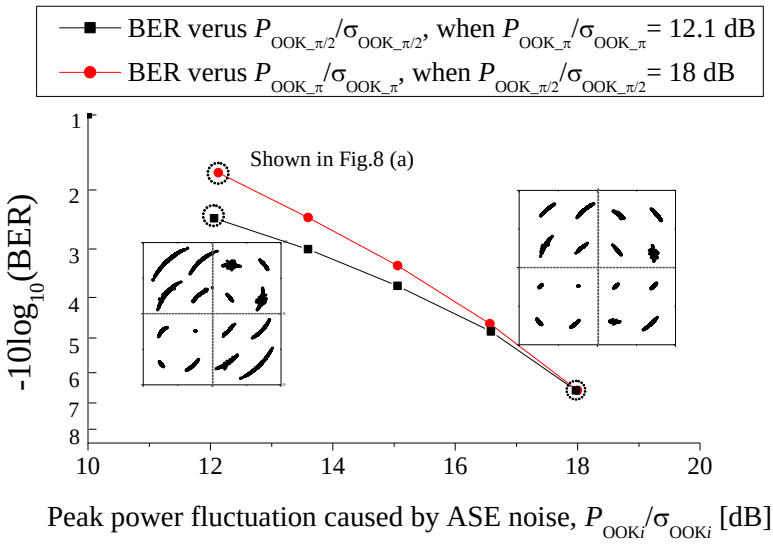

Fig. 5.10 Bit error rate of the converted 16QAM signal verus peak power fluctuation caused by ASE noise added to the OOK_π and OOK_π/2 signals, separately.

5.5 Conclusion

In this chapter, an all-optical OOK to 16QAM modulation format conversion scheme using a NOLM with 1:2 coupler has been proposed and experimentally demonstrated for the first time. However, the output signals were phase noisy due to the amplitude-to-phase-noise conversion. The ASE noise from EDFAs, in addition of a bit OPA and Raman gain, may induce random and pattern dependent power fluctuation in the OOK signals. The influence of ASE noise from the EDFAs used to amplify the control pulses for phase modulation onto the probe pulses has also been theoretically

discussed. The simulation results imply that the experimental results of the constellation map of 16QAM and APSK1 could be improved obviously, if the OOK_π signals were also amplified with limited ASE noise accompanied. The BER of the 16QAM signal versus the peak power to fluctuation ratio of the OOK signals has been numerically calculated. The errors induced by the amplitude-to-phase-noise conversion as the XPM employed all-optical OOK to 16QAM modulation format conversion system could be surmised by the simulation result.

Chapter 6

Conclusions

The nonlinearities in SOAs and optical fibers had been widely employed to realize all-optical modulation format conversion. The pattern effect in a SOA can seriously impair the performance of high-speed signal processing systems, and thus its operation speed is limited by its low recovery time. This thesis focuses on the fiber nonlinearity and its applicability for high-speed signal processing systems. The objective of this thesis is to develop technologies contributing to enlarge the network capacity by enhancing the throughput in gateway nodes and the network flexibility on choosing an optimal modulation format. Aiming at realization of a transparent gateway node for 100 Gb/s and beyond, the nonlinear effects in optical fibers are exploited, which are ultrafast phenomena with a response time of less than sub-picoseconds. A novel all-optical OOK to 16QAM format conversion based on fiber nonlinearity has been proposed in this thesis.

The NLS equation and the nonlinear effects of XPM and FWM, which are employed in the all-optical OOK to 16QAM format converter, have been introduced. Our system of a OOK to 16QAM format converter consists of a NOLM which is a valuable tool in optical signal processing applications. Compared with an all-fiber based Mach-zehnder interferometer, the phase drift between the clockwise and counter-clockwise lights can be ignored in the NOLM.

Measurement of the optical fiber nonlinear coefficient γ is now important for applications of fiber nonlinear devices in optical networks. We have proposed a novel fiber nonlinearity measurement method utilizing PM-FWM. With a simple setup, we have confirmed that the nonlinear coefficient γ can be determined for 0.1- to 1-km long HNLDSFs and a 1km-long low-nonlinearity SSMF in a straightforward way. The measured results had a good agreement with ones by the CW-SPM method. The CD and dispersion slope can be simultaneously measured with a high precision, and therefore, their influence on the nonlinear coefficient γ measurement could be removed.

An RZ-OOK to RZ-BPSK format conversion scheme has been described as part of the research work of this thesis. The Kerr effect of XPM was employed to achieve the amplitude to phase

modulation conversion. The main research work of this thesis was the all-optical OOK to 16QAM format conversion. We have proposed and numerically demonstrated an all-optical OOK to 16QAM modulation format conversion scheme using NOLM, and analytically evaluated the tolerance against the power deviation. It is noteworthy that this technique will enable to realize a transparent gateway node for 100Gb/s and beyond because XPM and OPA in optical fibers used are ultrafast phenomena with a response time of less than sub-picoseconds. The influence of the pulse shape of the control pulses were discussed because it is an important factor when employing the XPM effect. The peak powers of the control lights are key parameters in these nonlinear phenomena. In this regards, the power tolerance for four OOK signals and CW pump light used in the converter have also been analytically evaluated, and simple relations between the EVM and power deviations were derived.

In order to experimentally demonstrate the all-optical OOK to 16QAM format conversion, a simplified configuration of the converter with a 1:2 coupler employed in the NOLM has been proposed. This all-optical OOK to 16QAM modulation format conversion scheme has been experimentally demonstrated at 10GS/s for the first time in this thesis. However, the output signals were phase noisy due to the amplitude-phase-noise conversion. The ASE noise from EDFAs, in addition of a bit OPA and Raman gain, may induce power fluctuation to the OOK signals. The influence of ASE noise from the EDFAs used to amplify the control pulses for phase modulation onto the probe pulses has also been theoretically discussed. The simulation results imply that the experimental results of the constellation map of 16QAM and APSK1 could be improved obviously, if the OOK_π signals were also amplified with limited ASE noise accompanied. The BER of the 16QAM signal versus the peak power to fluctuation ratio of the OOK signals has been numerically calculated. The errors induced by the amplitude-to-phase-noise conversion as the XPM employed all-optical OOK to 16QAM modulation format conversion system could be surmised by the simulation result.

Bibliography

[1] F. -J. Westphal, A. Gladisch, and M. Gunkel, "Hierarchy and dynamics of optical networks," *Proc. ECOC 2009*, Vienna, Austria, Symposia 4.

[2] N. J. Frigo, P. P. Iannone, and K. C. Reichmann, "A view of fiber to the home economics," *IEEE Commun. Mag.*, Vol. 42, No. 8, pp. S16–S23, 2004.

[3] P. J. Winzer and R.-J. Essiambre, "Advanced optical modulation formats," *Proc. IEEE*, Vol. 94, No. 5, pp. 952–985, 2006.

[4] D. van den Borne, *Robust optical transmission systems*, Technische Universiteit Eindhoven, 2008.

[5] A. A. M. Saleh and J. M. Simmons, "Evolution toward the next-generation core optical network," *IEEE/OSA J. Lightw. Technol.*, Vol. 24, No. 9, pp. 3303-3321, 2006.

[6] T. J. Xia, S. Gringeri, and M. Tomizawa, "High-capacity optical transport networks," *IEEE Commun. Mag.*, Vol. 50, No. 11, pp. 170-178, 2012.

[7] G. Charlet, "Progress in optical modulation formats for high-bit rate WDM transmission," *IEEE J. Selected Topics in Quantum Electron.*, Vol. 12, No. 4, pp. 469-483, 2006.

[8] T. Ono, Y. Yano, K. Fukuchi, T. Ito, H. Yamakazi, M. Yamaguchi, and K. Emura, "Characteristics of optical duobinary signals in Terabit/s capacity, high−spectral efficiency WDM systems," *IEEE/OSA J. Lightw. Technol.*, Vol. 16, No. 5, pp. 788-797, 1998.

[9] K. Yonenaga and S. Kuwano, "Dispersion−tolerant optical transmission system using duobinary transmitter and binary receiver," *IEEE/OSA J. Lightw. Technol.*, Vol. 15, No. 8, pp. 1530-1537, 1997.

[10] T. Wuth, M. W. Chbat, and V. F. Kamalov, "Multi-rate (100G/40G/10G) transport over deployed optical networks," *Proc. OFC/NFOEC 2008*, San Diego, USA, Paper NTuB3.

[11] K. Schuh, E. Lach, B. Junginger, G. Veith, J. Renaudier, G. Charlet, and P. Tran, "8 Tbit/s (80x107 Gbit/s) DWDM ASK-NRZ VSB transmission over 510 km NZDSF with 1bit/s/Hz spectral efficiency," *Proc. ECOC 2007*, Berlin, Germany, Paper PD1.8.

[12] P. Bower and I. Dedic, "High speed converters and DSP for 100G and beyond," *Opt. Fiber Technol.*, Vol. 17, No. 5, pp. 464-471, 2011.

[13] G. W Lu and T. Miyazaki, "Experimental demonstration of RZ-8-APSK generation through optical amplitude and phase multiplexing," *IEEE Photon. Technol. Lett.*, Vol. 20, No. 23, pp. 1995-1997, 2008.

[14] S. L. Jansen, D. van den Borne, and M. Kuschnerov, "Advances in modulation formats for fiber-optic transmission systems," *Proc. OSA/CLEO'2011*, Baltimore, USA, Tutorial Paper CWJ1.

[15] D. van den Borne, M. Alfiad, S. L. Jansen, and T. Wuth, "40G/100G long-haul optical transmission system design using digital coherent receivers," *Proc. OECC'2009*, Hong Kong, China, Paper FN1.

[16] E. Lach and W. Idler, "Modulation formats for 100G and beyond," *Opt. Fiber Technol.*, Vol.17, No. 5, pp. 377-386, 2011.

[17] Y. Miyamoto and S. Suzuki, "Advanced optical modulation and multiplexing technologies for high-capacity OTN based on 100Gb/s channel and beyond," *IEEE Commun. Mag.*, Vol. 48, No. 3, pp. S65-S72, 2010.

[18] M. S. Alfiad, M. Kuschnerov, T. Wuth, T. J. Xia, G. Wellbrock, E. -D. Schmidt, D. van den Borne, B. Spinnler, C. J. Weiske, E. de Man, A. Napoli, M. Finkenzeller, S. Spaelter, M. Rehman, J. Behel, M. Chbat, J. Stachowiak, D. Peterson, W. Lee, M. Pollock, B. Basch, D. Chen, M. Freiberger, B. Lankl, and H. de Waardt, "111-Gb/s transmission over 1040-km field-deployed fiber with 10G/40G neighbors," *IEEE Photon. Technol. Lett.*, Vol. 21, No. 10, pp. 615-617, 2009.

[19] J. Winzer and R.−J. Essiambre, "Advanced modulation formats for high-capacity optical transport networks," *IEEE/OSA J. Lightw. Technol.*, Vol. 24, No.12, pp. 4711-4728, 2006.

[20] T. Matsuda, A. Naka, and S. Saito, "Comparison between NRZ and RZ signal formats for in-line amplifier transmission in the zero-dispersion regime," *IEEE/OSA J. Lightw Technol.*, Vol. 16, No. 3, pp. 340–348, 1998.

[21] M. I. Hayee and A. E. Willner, "NRZ versus RZ in 10–40-Gb/s dispersion managed WDM transmission systems," *IEEE Photon. Technol. Lett.*, Vol. 11, No. 8, pp. 991–993, 1999.

[22] M. Pfennigbauer, M. M. Strasser, M. Pauer, and P. J. Winzer, "Dependence of optically preamplified receiver sensitivity on optical and electrical filter bandwidths: Measurement and simulation," *IEEE Photon. Technol. Lett.*, Vol. 14, No. 6, pp. 831-833, 2002.

[23] W. Atia and R. S. Bondurant, "Demonstration of return-to-zero signaling in both OOK and DPSK formats to improve receiver sensitivity in an optically preamplified receiver," *Proc. LEOS 1999*, San Francisco, USA, pp. 226–227.

[24] S. Norimatsu and K. Ito, "Performance comparison of optical modulation formats for 40 Gbit/s systems from the viewpoint of frequency utilization efficiency and tolerance for fiber

nonlinearities," *Electronics and Communications in Japan* (*Part I: Communications*), Vol. 89, No. 8, pp. 50-64, 2006.

[25] T. Mizuochi, K. Ishida, T. Kobayashi, J. Abe, K. Kinjo, K. Motoshima, and K. Kasahara, "A comparative study of DPSK and OOK WDM transmission over transoceanic distances and their performance degradations due to nonlinear phase noise," *IEEE/OSA J. Lightw. Technol.*, Vol. 21, No. 9, pp. 1933-1943, 2003.

[26] Y. Ben-Ezra, U. Mahlab, M. Haridim, and B. I. Lembrikov, "Applications of all-optical signal processing in modern optical communications," *Proc. ICTON 2007*, Roma, Italy, pp. 328-331

[27] P. P. Baveja, D. N. Maywar, and G. P. Agrawal, "Optimization of all-optical 2R regenerators operating at 40 Gb/s: Role of dispersion, " *IEEE/OSA J. Lightw. Technol.*, Vol. 27, No.17, pp. 3831-3836, 2009.

[28] D. Norte and A. E. Willner, "All-optical data format conversions and reconversions between the wavelength and time domains for dynamically reconfigurable WDM networks," *IEEE/OSA J. Lightw. Technol.*, Vol. 14, No. 6, pp. 1170-1182, 1996.

[29] W. Li, M. Chen, Y. Dong, and S. Xie, "All-optical format conversion from NRZ to CSRZ and between RZ and CSRZ using SOA-based fiber loop mirror," *IEEE Photon. Technol. Lett.*, Vol. 16, No. 1, pp. 203-205, 2004.

[30] T. Silveira, A. Ferreira, A. Teixeira, and P. Monteiro, "40−Gb/s multichannel NRZ to CSRZ format conversion using an SOA," *IEEE/OSA J. Lightw. Technol.*, Vol. 16, No. 1, pp. 203−205, 2004.

[31] Y. Yu, X. Zhang, J. B. Rosas-Fernández, D. Huang, R. V. Penty, and I. H. White, "Single SOA based 16 DWDM channels all-optical NRZ-to-RZ format conversions with different duty cycles," *Opt. Express*, Vol. 16, No. 20, pp. 16166-16171, 2008.

[32] J. Dong, X. Zhang, F. Wang, Y. Yu, and D. Huang, "Single-to-dual channel NRZ-to-RZ format conversion by four-wave mixing in single semiconductor optical amplifier," *Electron. Lett.*, Vol. 44, No. 12, pp. 763-764, 2008.

[33] G. P. Agrawal, *Fiber−Optic Communications Systems*, 4th Edition, Wiley Series in microwave and optical engineering, 2010.

[34] C. Xu, X. Liu, and X. Wei, "Differential phase−shift keying for high spectral efficiency optical transmissions," *IEEE J. Selected Topics in Quantium Electron.*, Vol. 10, No. 2, pp. 281-293, 2004.

[35] A. H. Gnauck and P. J. Winzer, "Optical phase−shift−keyed transmission," *IEEE/OSA J. Lightw. Technol.*, Vol. 23, No.1, pp. 115-130, 2005.

[36] D. van den Borne, V. A. J. M. Sleiffer, M. S. Alfiad, S. L. Jansen, and T. Wuth, "POLMUX-QPSK modulation and coherent detection: The challenge of long-haul 100G transmission," *Proc. ECOC'2009*, Vienna, Austria, Paper, 3.4.1.

[37] C. Fludger, T. Duthel, D. van der Borne, C. Schulien, E.-D. Schmidt, T. Wuth, J. Geyer, E. de Man, G.-D. Khoe, and H. de Waardt, " Coherent equalization and POLMUX-RZ-DQPSK for robust 100– GE transmission," *IEEE/OSA J. Lightw. Technol.*, Vol. 26, No. 1, pp. 64-72, 2008.

[38] V. A. J. M. Sleiffer, V. Veljanovski, D. van den Borne, J. Capasso, H. Kuluslu, J. Seixas, V. Schramm, A. Tschersich, R. Nogueira, N. B. Pavlovic, K. Ivarson, S. Spaelter, and H.de Waardt, "45.8 and 125 Gb/s CP-QPSK/CP-BPSK field trial over installed submarine cable," *IEEE/OSA J. Lightw. Technol.*, Vol. 30, No. 4, pp. 624-633, 2012.

[39] K. Mishina, S. Kitagawa, and A. Maruta, "All-optical modulation format conversion from on-off-keying to multiple-level phase-shift keying based on nonlinearity in optical fiber," *Opt. Express*, Vol. 15, No. 13, pp. 8444-8453, 2007.

[40] S. Kitagawa, S. M. Nissanka, and A. Maruta, "All−optical modulation format conversion from NRZ−OOK to RZ−M−ary PSK based on fiber nonlinearity," *Proc. OFC'2008*, San Diego, USA, Paper OTuD6.

[41] C. Yan, Y. Su, L. Yi, L. Leng, X. Tian, X. Xu, and Y. Tian, "All-optical format conversion from NRZ to BPSK using a single saturated SOA," *IEEE Photon. Technol. Lett.*, Vol. 18, No. 22, pp. 2368-2370, 2006.

[42] H. Jiang, H. Wen, L. Han, Y. Guo, and H. Zhang, "All-optical NRZ-OOK to BPSK format conversion in an SOA-based nonlinear polarization switch," *IEEE Photon. Technol. Lett.*, Vol. 19, No. 24, pp. 1985-1987, 2007.

[43] A. Maruta and N. Hashimoto, "Experimental demonstration of all-optical modulation format conversion from NRZ-OOK to RZ-8APSK based on fiber nonlinearity," *Proc. OFC'2012*, LA, USA, Paper OM3B.

[44] K. Mishina, S. Kitagawa, M. Nissanka, A. Maruta, S. Mitani, K. Ishida, K. Shimizu, T. Hatta, and K. Kitayama, "All−optical modulation format conversion from NRZ−OOK to RZ−QPSK using parallel SOA−MZI OOK/BPSK converters," *Opt. Express*, Vol. 15, No. 12, pp. 7774-7785, 2007.

[45] J. Wang, J. Yang, I. M. Fazal1, N. Ahmed, Y. Yan, B. Shamee, A. E. Willner, K. Birnbaum, J. Choi, B. Erkmen, S. Dolinar, and M. Tur, "Demonstration of 12.8-bit/s/Hz spectral efficiency using 16QAM signal over multiple orbital-angular-momentum modes," *Proc. ECOC'2011*, Geneva, Switzerland, Paper We.10.P1.76.

[46] S. Yamanaka, T. Kobayashi, A. Sano, H. Masuda, E. Yoshida, Y. Miyamoto, T. Nakagawa, M. Nagatani, and H. Nosaka, "11 x 171 Gb/s PDM 16QAM transmission over 1440 km with a spectral efficiency of 6.4 b/s/Hz using high-speed DAC," *Proc. ECOC'2010*, Turin, Italy, Paper We.8.C.1.

[47] A. Sano, H. Masuda, T. Kobayashi, M. Fujiwara, K. Horikoshi, E. Yoshida, Y. Miyamoto, M. Matsui, M. Mizoguchi, H. Yamazaki, Y. Sakamaki, and H. Ishii, "Ultra-high capacity WDM

Transmission using spectrally-efficient PDM 16QAM modulation and C- and extended L-band wideband optical amplification," *IEEE/OSA J. Lightw. Technol.*, Vol. 29, No. 4, pp. 578-586, 2011.

[48] M. S. Alfiad, M. Kuschenerov, S. L. Jansen, T. Wuth, D. Borne, and H. Waardt, "11x224-Gb/s polmux-RZ-16QAM transmission over 670 km of SSMF with 50-GHz channel spacing," *IEEE Photon. Technol. Lett*., Vol. 22, No. 15, pp. 1150-1152, 2010.

[49] P. J. Winzer, A. H. Gnauck, S. Chandrasekhar, S. Draving, J. Evangelista, and B. Zhu, "Generation and 1,200-km transmission of 448-Gb/s ETDM 56-Gbaud PDM 16-QAM using a single I/Q modulator," *Proc. ECOC'2010*, Turin, Italy, Paper PD2.2.

[50] T. Richter, E. Palushani, C. Schmidt-Langhorst, M. Nölle, R. Ludwig, and C. Schubert, "Single wavelength channel 10.2 Tb/s TDM-data capacity using 16QAM and coherent detection," *Proc. OFC'2011*, LA, USA, Paper PDPA9.

[51] S. Aleksic and V. Krajinovic, "Methods for compensation of the pattern effect in semiconductor optical amplifiers," *NOC'2003*, Vienna, Austria, pp. 159-166.

[52] G. P. Agrawal, *Nonlinear fiber optics*, 4th Edition, Academic Press, 2007.

[53] K. Kawano and T. Kitoh, *Introduction to optical waveguide analysis: solving Maxwells equation and the Schrödinger equation*, a Wiley-Interscience Publication, 2001.

[54] M. I. Hayee and A. E. Willner, "NRZ versus RZ in 10–40-Gb/s dispersion-managed WDM transmission systems," *IEEE Photon. Technol. Let.*, Vol. 11, No. 8, pp. 991-993, 1999.

[55] J. Hansryd, Peter A. Andrekson, M. Westlund, J. Li, and P.-O. Hedekvist, "Fiber-based optical parametric amplifiers and their applications," *IEEE J. Selected Topics in Quantum Electron.*, Vol. 8, No. 3, pp. 506-520, 2002.

[56] Q. Lin, F. Yaman, and G. P. Agrawal, "Photon-pair generation by four-wave mixing inside optical fibers," *Opt. Lett.*, Vol. 31, No. 9, pp. 1286-1288, 2006.

[57] F. Yaman, Q. Lin, and G. P. Agrawal, "A novel design for polarization-independent single-pump fiber-optic parametric amplifiers," *IEEE Photon. Technol. Lett.*, Vol. 18, No. 22, pp. 2335-2337, 2006

[58] Y. Miyoshi, S. Takagi, S. Namiki, and K. Kitayama, "Multi-period PM-NOLM with dynamic counter-propagating effects compensation for 5-bit all-optical analog-to-digital conversion and its performance evaluations," *IEEE/OSA J. Lightw. Technol.*, Vol. 28, No. 4, pp. 415- 422, 2010.

[59] M. Saruwatari, K. Tsuji, N. Onodera, and T. Yamaguchi, "Wavelength-flexible optical signal conversion using a NOLM-based XPM circuit followed by a Brillouin-assisted notch-filtering technique," *Proc. PS'2006*, Heraklion, Crete, pp. 1-3.

[60] C. H. Kwok, S. H. Lee, K. K. Chow, C. Shu, L. Chinlon, and A. Bjarklev, ”Widely tunable wavelength conversion with extinction ratio enhancement using PCF-based NOLM,” *IEEE Photon. Technol. Lett.*, Vol. 17, No. 12, pp. 2655 – 2657, 2005.

[61] M. Zhang, P. Ye, F. Zhang, Y. Zhao, and J Wang, “NOLM-based wavelength conversion with FBG band-pass filter for optical packet switching,” *C. Opt. Lett.*, Vol. 1, No. 1, pp. 3-5, 2003.

[62] P. Honzatko and M. Karásek, “10 and 20 Gb/s all-optical RZ to NRZ modulation format and wavelength converter based on nonlinear optical loop mirror,” *Opt. Commun.*, Vol. 283, No. 10, pp. 2061-2065, 2010.

[63] A. G. Striegler, M. Meissner, K. Cvecek, K. Sponsel, G. Leuchs, and B. Schmauss, “NOLM-based RZ-DPSK signal regeneration,” *IEEE Photon. Technol. Lett.*, Vol. 17, No. 3, pp. 639-641, 2005.

[64] K. Cvecek, G. Onishchukov, K. Sponsel, A. G. Striegler, B. Schmauss, and G. Leuchs, “Experimental investigation of a modified NOLM for phase-encoded signal regeneration,” *IEEE Photon. Technol. Lett.*, Vol. 18, No. 17, pp. 1801-1803, 2006.

[65] M. Hirano, T. Nakanishi, T. Okuno, and M. Onishi, “Silica-based highly nonlinear fibers and their application,” *IEEE J. Selected Topics in Quantum Electron.*, Vol. 15, No. 1, pp. 103-113, 2009.

[66] M. Hirano and T. Sasaki, “Straightforward chromatic dispersion measurement based on phase mismatching FWM,” *Proc. ECOC'2009*, Vienna, Austria, Paper 4.1.6.

[67] R. H. Stolen and L. Chinlon, “Self-phase-modulation in silica optical fibers,” *Phys. Rev. A*, Vol. 17, No. 4, pp. 1448-1453, 1978.

[68] M. Monerie and Y. Durteste, “Direct interferometric measurement of nonlinear refractive index of optical fiber by cross-phase modulation,” *Electron. Lett.*, Vol. 23, No. 18, pp. 961-963, 1987.

[69] C. Vinegoni, M. Wegmuller, B. Huttner, and N. Gisin, “Measurement of nonlinear polarization rotation in a highly birefringent optical fibre using a Faraday mirror,” *J. Opt. A: Pure Appl. Opt.* Vol. 2, No. 4, pp. 314–318, 2000.

[70] F. Wittl, “Interferometric determination of the nonlinear refractive index n2 of optical fibers,” Proc. Symposium on Optical Fiber Measurements, pp. 71-74, 1996.

[71] C. Vinegoni, M. Wegmuller, and N. Gisin, “Measurement of the nonlinear coefficient of standard SMF, DSF, and DCF fiber using a self-aligned interferometer and a Faraday Mirror,” *IEEE Photon. Technol. Lett.*, Vol. 13, No. 12, pp. 1337-1339, 2001.

[72] A. Boskovic, S. V. Chernikov, J. R. Taylor, L. Gruner-Nielsen, and O. A. Levring, “Direct continuous-wave measurement of n2 in various types of telecommunication fiber at 1.55 μm,” *Opt. Lett.*, Vol. 21, No. 24, pp. 1966-1968, 1966.

[73] L. Prigent and J. -P. Hamaide, “Measurement of fiber nonlinear Kerr coefficient by four-wave mixing,” *IEEE Photon. Technol. Lett.*, Vol. 5, No. 9, pp. 1062-1065, 1993.

[74] T. Dennis and P. A. Williams, "Achieving high absolute accuracy for group-delay measurements using the modulation phase-shift technique," *IEEE/OSA J. Lightw. Technol.*, Vol. 23, No. 11, pp. 3748-3754, 2005.

[75] M. C. Ho, M. E. Marhic, K. Y. K. Wong, and L. G. Kazovsky, "Narrow-linewidth idler generation in fiber four-wave mixing and parametric amplification by dithering two pumps in opposition of phase," *IEEE/OSA J. Lightw. Technol.*, Vol. 20, No. 3, pp. 469-476, 2002.

[76] J. P. Gordon and L. F. Mollenauer, "Phase noise in photonic communications systems using linear amplifiers," *Opt. Lett.*, Vol. 15, No. 23, pp. 1351-1353, 1990.

[77] S. Kumar, A. Selvarajan, and G. Anand, "Nonlinear propagation of two optical pulses of two different frequencies in birefringent nonlinear fibers," *J. Opt. Soc. Am. B*, Vol. 11, No. 5, pp. 810-817, 1994.

Acronyms

ADC	analog to digital converter
APSK	amplitude phase shift keying
ASE	amplified spontaneous emission
ASK	amplitude shift keying
AWGN	additive white Gaussian noise
BASK	binary amplitude shift keying
BER	bit error rate
BPSK	binary phase shift keying
CD	chromatic dispersion
CMOS	complementary metal-oxide-semiconductor
CP	coherent-detected polarization-multiplexed
CW	continuous wave
DAC	digital to analog converter
DCF	dispersion compensated fiber
DSF	dispersion shifted fiber
DSP	digital signal processing
DWDM	dense wavelength division multiplexing
EDFA	erbium doped fiber amplifier
E/O	electrical-to-optical
EVM	error vector magnitude
FWM	four-wave mixing
FWHM	full width at half maximum
HNLDSF	highly nonlinear dispersion-shifted fiber
HNLF	highly nonlinear optical fiber
ISI	inter-symbol interference
ISO	optical isolator
LN-IM	lithium niobate-intensity modulator
MAN	metro area network

MPS	modulation phase shift
MZI	Mach-Zehnder interferometer
NOLM	nonlinear optical loop mirror
NLS	nonlinear Schrödinger
NRZ	non-return-to-zero
OBPF	optical bandpass filter
OC	optical coupler
O/E	optical-to-electrical
OOK	on-off-keying
OPA	optical parametric amplification
OSA	optical spectrum analyzer
OSNR	optical signal-to-noise ratio
OTDM	optical time division multiplexing
PA	polarization analyzer
PC	polarization controller
PM	power meter
PM	polarization-maintaining
PMD	polarization-mode dispersion
PM-FWM	phase-mismatching-FWM
PRBS	pseudo-random binary sequence
PSK	phase shift keying
PMD	polarization mode dispersion
QPSK	quadrature phase shift keying
RZ	return-to-zero
SBS	stimulated Brillouin scattering
SE	spectral efficiency
SOA	optical semiconductor amplifier
SPM	self-phase modulation
SSMF	standard single mode fiber
TLS	tunable laser source
VOA	optical variable attenuator
VODL	variable optical delay line
WAN	wide area network
WDM	wavelength division multiplexing
XPM	cross phase modulation

List of Publications

A. Journals

[1]. G. Huang, Y. Miyoshi, A. Maruta, Y. Yoshida, and K. Kitayama, ”All-optical OOK to 16QAM Modulation Format Conversion Employing Nonlinear Optical Fiber Loop Mirror,” *IEEE/OSA J. Lightw. Technol.*, Vol. 30, No. 9, pp. 1342-1350, 2012. [In Chapter 4]

[2]. G. Huang, Y. Miyoshi, A. Maruta, and K. Kitayama, ”All-optical technique for modulation format conversion from NRZ-OOK to RZ-16QAM employing nonlinear optical loop mirror with 1:2 coupler,” *Opt. Express*, Vol. 20, No. 24, pp. 27311-27321, 2012. [In Chapter 5]

[3]. G. Huang, Y. Yamamoto, M. Hirano, A. Maruta, T. Sasaki, and K. Kitayama, “Straightforward method for measuring optical fiber’s nonlinear coefficient based on phase- mismatching FWM,” *Opt. Express*, Vol. 21, No. 17, pp. 20463-20469, 2013. [In Chapter 3]

B. International conferences

[1]. G. Huang, Y. Miyoshi, N. Hashimoto, Y. Yoshida, A. Maruta, and K. Kitayama, “All-optical RZ-OOK to RZ-BPSK modulation format conversion based on fiber nonlinearity,” *Asia Communications and Photonics Conferance and Exhibition* (*ACP*), Shanghai, China, Paper ThB4, Dec. 2010. [In Chapter 4]

[2]. G. Huang, Y. Miyoshi, Y. Yoshida, A. Maruta, and K. Kitayama, ”All-optical OOK to 16QAM Modulation Format Conversion Employing Nonlinear Optical Fiber Loop Mirror,” *Optical Fiber Communication Conf. Expo.* (*OFC*), LA, USA, Paper OThN6, Mar. 2011. [In Chapter 4]

[3]. G. Huang, Y. Miyoshi, Y. Yoshida, A. Maruta, and K. Kitayama, ”All-optical OOK to 16QAM modulation conversion based on nonlinear optical loop mirror with 1:2 coupler,” *Optical Fiber Communication Conf. Expo.* (*OFC*), LA, USA, Paper OTh4H, Mar. 2012. [In Chapter 5]

[4]. G. Huang, Y. Miyoshi, A. Maruta, and K. Kitayama, ”The effect of ASE on XPM employed all optical OOK to Multi-level modulation format conversion,” *Asia Communications and Photonics Conferance and Exhibition* (*ACP*), Guangzhou, China, Paper AF4A, Nov. 2012. [In Chapter 5]

[5]. G. Huang, Y. Yamamoto, M. Hirano, A. Maruta, T. Sasaki, and K. Kitayama, ”Fiber nonlinear coefficient measurement based on phase mismatching FWM”, *CLEO-PR&OECC/PS*, Kyoto, Japan, Paper WS4-2, Jun. 2013. [In Chapter 3]

C. Domestic conferences

[1]. G. Huang, Y. Miyoshi, Y. Yoshida, A. Maruta, and K. Kitayama, “All-optical OOK to 16QAM Modulation Format Conversion Employing Nonlinear Optical Fiber Loop Mirror,” *Technical Report on Optical Communication Systems (OCS)*, Vol. 111, No. 122, pp. 71-76 (OCS2011-39). [In Chapter 4]

[2]. G. Huang, Y. Miyoshi, A. Maruta, Y. Yoshida, and K. Kitayama, “Experimental demonstration of all-optical OOK to 16QAM modulation conversion based on Nonlinear Optical Loop mirror with 1:2 coupler,” *Technical Report on Optical Communication Systems (OCS)*, Vol. 112, No. 152, pp. 35-40 (OCS2012-27). [In Chapter 5]

[3]. G. Huang, Y. Miyoshi, N. Hashimoto, Y. Yoshida, A. Maruta, and K. Kitayama, “All-optical RZ-OOK to RZ-BPSK modulation format conversion based on fiber nonlinearity,” *The 2010 IEICE Society Conference*, Osaka Prefecture University, B-10-72, Sep. 2010. [In Chapter 4]

[4]. G. Huang, Y. Yamamoto, M. Hirano, A. Maruta, T. Sasaki, and K. Kitayama, “Phase-mismatching FWM method for the measurement of SSMF’s chromatic dispersion and nonlinear coefficients,” *The 2013 IEICE Society Conference*, Fukuoka Institute of Technology, B-13-39, Sep. 2013. [In Chapter 3]